Università degli Studi di Ferrara
Facoltà di Scienze Matematiche, Fisiche e Naturali
Corso di Dottorato di Ricerca in Fisica, XV Ciclo

Precision Polarization Measurement of the HERMES H/D Gas Target

Relatore:

Prof. Dr. PAOLA FERRETTI DALPIAZ

Dottorando:

DAVIDE REGGIANI

Relatore Aggiunto:

Dr. PAOLO LENISA

Anni 2000-2002

Contents

Introduction

Since 1995 the HERMES experiment has been running in the HERA storage ring, at DESY, mainly devoted to the study of the spin structure of the nucleon. At HERMES deep inelastic scattering events are produced by exploiting the 27.5 GeV electron/positron beam in combination with an internal polarized gas target. Thanks to the Sokolov-Ternov mechanism [Sok64], the HERA beam is characterized by a self polarization, transverse to its momentum, which is turned to longitudinal at the HERMES interaction point by the employment of two spin rotators. Beside the identification of the inclusive events, the HERMES spectrometer, furnished with a dual radiator RICH detector, is capable of distinguish between pions, kaons and protons, thus allowing the semi-inclusive analysis.
Since 1996 HERMES has been employing a polarized hydrogen/deuterium gas target, whose spin orientation, defined by the application of an external magnetic field, was kept longitudinal to the beam momentum till the end of 2000 and switched to transverse in 2001. The polarized gas is produced by an atomic beam source (ABS) and diagnosed by a target gas analyzer (TGA), measuring the atomic and molecular relative contents, and by a Breit-Rabi polarimeter (BRP) which determines the polarization of atoms.
Gas targets offer significant advantages over solid state targets for spin experiment as they provide high degree of polarization ($P > 0.8$), they are free of dilution ($f = 1$) and they can invert the spin of the atoms in milliseconds, substantially reducing the systematic errors of spin experiments. The HERMES target makes use of a storage cell in order to confine the polarized atoms to a small volume around the path of the high energy beam. The cell consists in an open ended aluminum tube, through which the HERA beam passes, provided with two side tubes for injection and sampling of the polarized gas. This technique, firstly developed in the early '80s [Hae80], results in a typical areal density increase of about two orders of magnitude compared to a free jet target. Beside HERMES, various experiment have already used storage cells as internal gas target [Gil93, Dez95, Zap96, Buu00] and more are planned [Ala00, Bar01].
Some potential disadvantages are connected to the application of a storage cell. Spin relaxation and/or recombination into molecules can be generated by the numerous collisions of the atoms with the cell wall, reducing therefore the target polarization. Furthermore, as the occurrence of these processes is not uniform along the cell, specific corrections have

to be developed in order to relate the properties of the sample gas to the average target values. These complications make the calculation of the target polarization a rather involved effort.
The goal of this thesis is to present an accurate measurement of the HERMES target performance. The whole procedure that has been developed in order to perform a highly accurate measurement of the target nuclear polarization is described in details. The calibration techniques allowing to distinguish the unpolarized molecules coming from background sources from the potentially polarized recombined molecules is presented, as well as the possible measurements that can be accomplished to disentangle the effects due to different spin relaxation processes. Some particular measurements are shown, whose results give indication of the cell surface properties, allowing in this way a limitation of the target polarization systematic error. So far, in case of relatively high recombination rate, one of the strongest contribution to the uncertainty of the target polarization value has been given by the lack of knowledge about the value of the remnant nuclear polarization of recombined molecules. In this thesis, the first measurement of this quantity obtained at HERMES is presented. Eventually, all the results coming from the single analyses are brought together and exploited to the determination of the target average polarization achieved during data taking for the running periods of 1997, with hydrogen, and 2000, with deuterium.
Through the one year long HERA luminosity upgrade shutdown in 2000/2001, a significant effort has been made in order to set up a transverse polarized target at HERMES. The studies that were carried out to design a holding magnet compatible with the environmental constraints and, at the same time, with the experimental request in terms of target performance are discussed together with the first results.

The thesis is structured in the following way.

- In the first chapter, the hyperfine structure of hydrogen and deuterium is presented as a way to understand the working principle of th HERMES target. Particular emphasis is addressed to the explanation of the main drawback related to the newly developed transverse polarized target, namely the possible depolarization via HERA beam induced hyperfine transitions.

- The second chapter is devoted to the experimental setup. Beside detailed descriptions of the two detectors involved in the polarization measurement, TGA and BRP, specific account assumes here the section dedicated to the design of the transverse target magnet.

- In the third chapter, the general approach that has to be applied for the calculation of the target polarization is presented. Explanations on how to treat all the possible sources of target depolarization and recombination are given along with the related measurements.

- The fourth chapter is dedicated to the analysis of the longitudinal hydrogen running period in 1997. During this year the instability of the target performance has been compensated by the possibility of understanding the changing cell surface conditions. Of great importance is the section devoted to the measurement of the molecular polarization.

- In the last chapter the calculation of the target polarization for the deuterium run in 2000 is shown. The outstanding target performance of these period allowed to collect one of the best polarized deuterium dataset currently available in the world.

Chapter 1

Hyperfine Structure and Beam Induced Target Depolarization

The knowledge of hydrogen and deuterium hyperfine structure is essential for the understanding of the HERMES polarized target. First of all, the target polarization is achieved and measured by selecting particular hyperfine states through the Stern-Gerlach separation and by exchanging their populations via hyperfine transitions. Furthermore, potential processes of spin relaxation can be explained in terms of the same transition's mechanism. This is particularly true for the case of the resonant depolarization induced by the HERA electron bunched beam.
After a survey over the basics of the static hyperfine structure of hydrogen and deuterium, the central part of the chapter is devoted to the theory of hyperfine transitions. Particular emphasis will be addressed to the study of the beam induced spin relaxation which has played a central role during the design and setup of the transversely polarized target through the one year long HERA shutdown in 2001/2002.

1.1 The solution of the static Hamiltonian

The hyperfine structure of the hydrogen/deuterium atom in the ground state $1S_{1/2}$ can be derived from a Hamilton operator describing the coupling between the spin of the electron $\mathbf{S}$ and spin on the nucleus $\mathbf{I}$ and the additional interactions of the magnetic moments with an external magnetic field $\mathbf{B}$:

$$\mathcal{H} = A_{H,D}\mathbf{S}\cdot\mathbf{I} + \frac{g_S\mu_B}{\hbar}\mathbf{S}\cdot\mathbf{B} - \frac{g_I\mu_N}{\hbar}\mathbf{I}\cdot\mathbf{B} \tag{1.1}$$

The constant $A_{H,D}$ contains information about the coupling strength between $\mathbf{S}$ and $\mathbf{I}$ for hydrogen and deuterium respectively. The quantity $\mu_B = \frac{e\hbar}{2m_ec}$ ($\mu_N = \frac{e\hbar}{2m_pc}$) is the Bohr (nuclear) magnet on relating the spin $\mathbf{S}$ ($\mathbf{I}$) to the magnetic moment $\boldsymbol{\mu}_\mathbf{e}$ ($\boldsymbol{\mu}_\mathbf{I}^{p,d}$ for proton and deuteron respectively) through $\frac{\boldsymbol{\mu}_\mathbf{e}}{\mu_B} = g_S\mathbf{S}$ ($\frac{\boldsymbol{\mu}_\mathbf{I}^{p,d}}{\mu_N} = g_I\mathbf{I}$), where $g_S = 2.0023$

($g_I^p = 5.5857$, $g_I^d = 0.8574$) is the electron (proton, deuteron) gyro-magnetic factor.
In case of hydrogen the coupling $\mathbf{F} = \mathbf{S} \cdot \mathbf{I}$, where $S = I = \frac{1}{2}$, originates a singlet state with total spin $F = 0$ and a triplet with $F = 1$ ($m_F = \pm 1, 0$). In case of deuterium $I = 1$, so that a doublet $F = \frac{1}{2}$ ($m_F = \pm\frac{1}{2}$) and a quadruplet $F = \frac{3}{2}$ ($m_F = \pm\frac{3}{2}, \pm\frac{1}{2}$) are produced by the spin-spin coupling. The energy difference between the two levels is known as *hyperfine splitting* $E_{HFS}^{H,D}$ for hydrogen and deuterium respectively.
The presence of an external magnetic field $\mathbf{B}$ introduces the additional couplings $\mathbf{S} \cdot \mathbf{B}$ and $\mathbf{I} \cdot \mathbf{B}$. This leads to the splitting of the non-singlet states and the consequent generation of four defined energy levels for hydrogen and six for deuterium.

1.1.1 Hydrogen

The Hamiltonian (1.1) can be written as follows:

$$\mathcal{H} = A_H \hbar^2 \left[\frac{\mathbf{S} \cdot \mathbf{I}}{\hbar^2} + \frac{\mathbf{B}}{B_C^H} \cdot \left(\frac{\mathbf{S}}{\hbar} - \varepsilon_H \frac{\mathbf{I}}{\hbar} \right) \right] \tag{1.2}$$

where $B_C^H = \frac{A_H \hbar^2}{g_S \mu_B} = 50.7\,\mathrm{mT}$ is the so-called *critical field*, whereas $\varepsilon_H = \frac{g_I \mu_N}{g_S \mu_B} = 1.5 \cdot 10^{-3} \ll 1$.
In the representation $|\, \mathbf{S}^2, \mathbf{I}^2; m_S, m_I \,\rangle$ (where m_S and m_I refer to the operators S_z e I_z), a basis for the Hamilton operator is given by:

$$|\uparrow +\rangle \quad , \quad |\uparrow -\rangle \quad , \quad |\downarrow -\rangle \quad , \quad |\downarrow +\rangle \tag{1.3}$$

where the arrow refers to the electron and the sign to the nuclear spin. The spin-spin coupling term in 1.2 can be written as

$$\mathbf{S} \cdot \mathbf{I} = I_z S_z + \frac{1}{2}(I_+ S_- + I_- S_+) \tag{1.4}$$

where $I_\pm = I_x \pm i I_y$ and $S_\pm = S_x \pm i S_y$. Taking into account that $S_z = I_z = \pm\frac{\hbar}{2}$, one can write 1.4 in the following matrix representation:

$$\mathbf{S} \cdot \mathbf{I} = \frac{\hbar^2}{4} \begin{pmatrix} 1 & 0 & 0 & 1 \\ 0 & -1 & 0 & 2 \\ 0 & 0 & 1 & 0 \\ 0 & 2 & 0 & -1 \end{pmatrix} \tag{1.5}$$

For the terms of 1.2 representing the interactions with the external magnetic field, one has:

$$\mathbf{S} \cdot \mathbf{B} = S_z B_z + \frac{1}{2} S_+ (B_x - i B_y) + \frac{1}{2} S_- (B_x + i B_y) \tag{1.6}$$

and correspondingly

$$\mathbf{I} \cdot \mathbf{B} = I_z B_z + \frac{1}{2} I_+ (B_x - i B_y) + \frac{1}{2} I_- (B_x + i B_y) \tag{1.7}$$

In case of a static magnetic field along the z direction, $\mathbf{B} = (0, 0, B)$ and defining the variable $x = \frac{B}{B_C^H}$, the matrix representations of (1.6) and (1.7) are:

$$\frac{\mathbf{B}}{B_C^H} \cdot \mathbf{S} = \frac{\hbar}{2} \begin{pmatrix} x & 0 & 0 & 0 \\ 0 & x & 0 & 0 \\ 0 & 0 & -x & 0 \\ 0 & 0 & 0 & -x \end{pmatrix} \tag{1.8}$$

and

$$\frac{\mathbf{B}}{B_C^H} \cdot \mathbf{I} = \frac{\hbar}{2} \begin{pmatrix} x & 0 & 0 & 0 \\ 0 & -x & 0 & 0 \\ 0 & 0 & -x & 0 \\ 0 & 0 & 0 & x \end{pmatrix} \tag{1.9}$$

The static Hamiltonian $\mathcal{H}_0^{st}$ can now be completely represented by the following matrix form:

$$\mathcal{H}_0^{st} = \frac{A_H \hbar^2}{4} \begin{pmatrix} 1 + 2x(1-\varepsilon_H) & 0 & 0 & 0 \\ 0 & -1 + 2x(1+\varepsilon_H) & 0 & 2 \\ 0 & 0 & 1 - 2x(1-\varepsilon_H) & 0 \\ 0 & 2 & 0 & -1 - 2x(1+\varepsilon_H) \end{pmatrix} \tag{1.10}$$

Since the matrix (1.10) is not diagonal, the basis (1.3) does not represent a set of eigenstates of (1.2). The diagonalization of (1.10) can be performed by means of an orthogonal transformation:

$$\mathcal{H}_1^{st} = U_0^T \mathcal{H}_0^{st} U_0 \tag{1.11}$$

where the orthonormal matrix U_0 is given by

$$U_0 = \begin{pmatrix} 1 & 0 & 0 & 0 \\ 0 & \cos\theta & 0 & -\sin\theta \\ 0 & 0 & 1 & 0 \\ 0 & \sin\theta & 0 & \cos\theta \end{pmatrix} \tag{1.12}$$

The so-called *mixing angle* θ depends on $x = \frac{B}{B_C}$ and can be derived from the following relations:

$$\begin{aligned} \cos\theta &= \sqrt{\tfrac{1}{2}(1+\cos 2\theta)} & \sin\theta &= \sqrt{\tfrac{1}{2}(1-\cos 2\theta)} \\ \cos 2\theta &= \frac{x(1+\varepsilon_H)}{\sqrt{x^2(1+\varepsilon_H)^2+1}} & \sin 2\theta &= \frac{1}{\sqrt{x^2(1+\varepsilon_H)^2+1}} \end{aligned} \tag{1.13}$$

The eigenenergies of $\mathcal{H}_1^{st}$ are:

$$\begin{aligned} E_1 &= \frac{E_{HFS}^H}{4}\left(1 + 2x(1-\varepsilon_H)\right) & E_3 &= \frac{E_{HFS}^H}{4}\left(1 - 2x(1-\varepsilon_H)\right) \\ E_2 &= \frac{E_{HFS}^H}{4}\left(-1 + 2\sqrt{x^2(1+\varepsilon_H)^2+1}\right) & E_4 &= \frac{E_{HFS}^H}{4}\left(-1 - 2\sqrt{x^2(1+\varepsilon_H)^2+1}\right) \end{aligned} \tag{1.14}$$

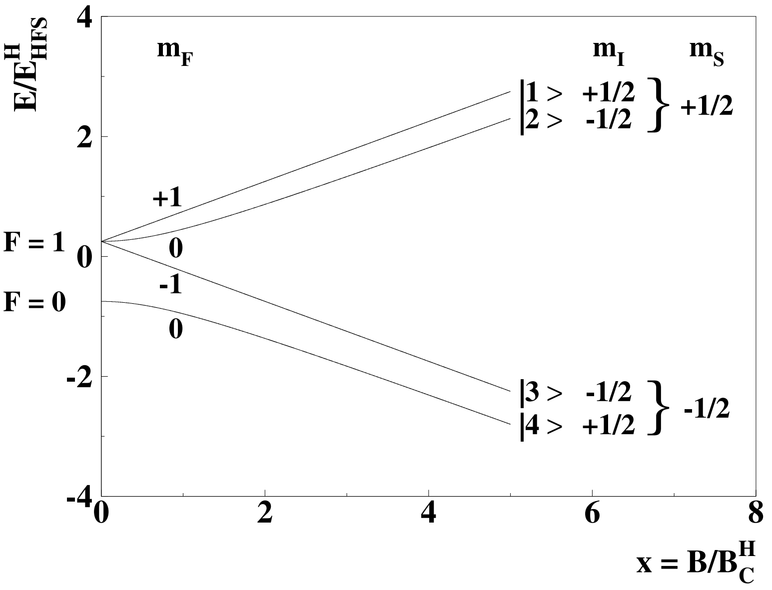

Figure 1.1: Hyperfine energy levels of hydrogen plotted as functions of the magnetic holding field (Breit-Rabi diagram). The energies are scaled to the hyperfine energy E^H_{HFS} and the field values to the critical field B^H_C.

where $E^H_{HFS} = A_H\hbar^2 = 5.87 \cdot 10^{-5}\,\mathrm{eV}$ represents the energy difference between the state with total spin $F = 1$ and the one with $F = 0$, if no external magnetic field is present ($x = 0$). The hydrogen hyperfine splitting is usually known in terms of the frequency $\nu^H_{HFS} = \frac{E^H_{HFS}}{2\pi\hbar} = 1420.4\,\mathrm{MHz}$. In figure 1.1 the hydrogen hyperfine eigenenergies are plotted as functions of the variable x.
The new basis is composed by eigenstates of the operators $\mathbf{F}^2$ and $F_z = S_z + I_z$:

$$\begin{aligned} |\,1\,\rangle &= |\uparrow +\rangle & \qquad |\,3\,\rangle &= |\downarrow -\rangle \\ |\,2\,\rangle &= \cos\theta\,|\uparrow -\rangle + \sin\theta\,|\downarrow +\rangle & \qquad |\,4\,\rangle &= \sin\theta\,|\uparrow -\rangle - \cos\theta\,|\downarrow +\rangle \end{aligned} \tag{1.15}$$

Polarization definitions

The electron and nuclear polarizations (P_e and P_z) of the state $|\,i\,\rangle$ are given by the expectation values of the operators $\frac{2}{\hbar}S_z$ and $\frac{2}{\hbar}I_z$ respectively. For a sample of atoms one has:

$$P_e = \sum_{i=1}^{4} n_i \langle\, i\,|\frac{2}{\hbar}S_z|\,i\,\rangle = n_1 - n_3 + (n_2 - n_4)\cos 2\theta \tag{1.16}$$

$$P_z = \sum_{i=1}^{4} n_i \langle\, i\,|\frac{2}{\hbar}I_z|\,i\,\rangle = n_1 - n_3 - (n_2 - n_4)\cos 2\theta \tag{1.17}$$

where n_i is the relative population of state $|\,i\,\rangle$, undergoing the following normalization condition:

$$\sum_i n_i = 1 \tag{1.18}$$

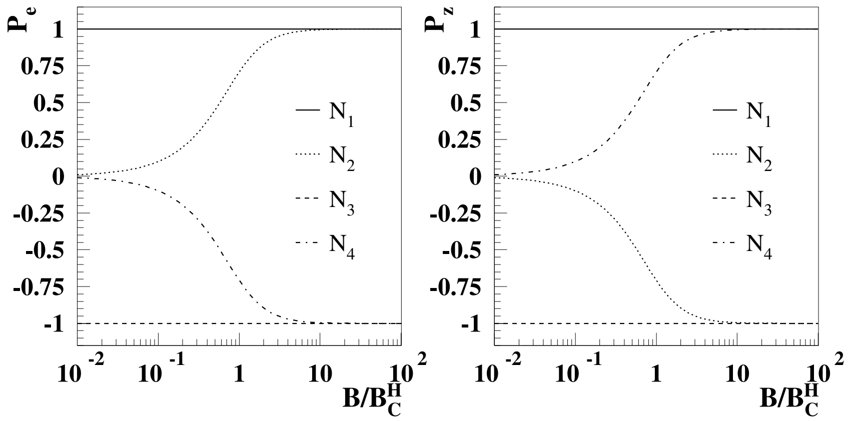

Figure 1.2:
The electron (left) and nuclear polarizations of the four hydrogen hyperfine states plotted as functions of the external magnetic field. The field values are normalized to the critical field B_C^H.

P_e and P_z for the different hydrogen hyperfine states are plotted in figure 1.2 as function of the applied magnetic field.
The critical field B_C^H marks the boundary between two field regions:

- $B \ll B_C^H \Longleftrightarrow \theta \to \frac{\pi}{4}$, Zeeman limit.
  The interaction with the external field can be treated perturbatively. A basis is given by the eigenstates of $|\,F, m_F\,\rangle$. The pure states $|\,1\,\rangle$ and $|\,3\,\rangle$ are polarized ($P_e = P_z = \pm 1$), whereas $|\,2\,\rangle$ e $|\,4\,\rangle$ are unpolarized ($P_e = P_z \simeq 0$):

$$
\begin{aligned}
|\,1\,\rangle &\simeq |\,F=1, m_F=+1\,\rangle &=& \;|\uparrow +\rangle \\
|\,2\,\rangle &\simeq |\,F=1, m_F=0\,\rangle &=& \;\frac{1}{\sqrt{2}}(|\uparrow -\rangle + |\downarrow +\rangle) \\
|\,3\,\rangle &\simeq |\,F=1, m_F=-1\,\rangle &=& \;|\downarrow -\rangle \\
|\,4\,\rangle &\simeq |\,F=0, m_F=0\,\rangle &=& \;\frac{1}{\sqrt{2}}(|\uparrow -\rangle - |\downarrow +\rangle)
\end{aligned} \tag{1.19}
$$

- $B_z >> B_C^H \Longleftrightarrow \theta \to 0$, Paschen-Back limit.
  The spin-spin interaction can be treated perturbatively. Now the eigenstates can be represented by the basis (1.3) where all the states are polarized.

1.1.2 Deuterium

In case of deuterium the Hamiltonian (1.1) can be written as follows:

$$
\mathcal{H} = A_D \hbar^2 \left[\frac{\mathbf{S}\cdot\mathbf{I}}{\hbar^2} + \frac{3}{2}\frac{\mathbf{B}}{B_C^D}\left(\frac{\mathbf{S}}{\hbar} - \varepsilon_D \frac{\mathbf{I}}{\hbar}\right) \right] \tag{1.20}
$$

where $B_C^D = \frac{3}{2}\frac{A_D \hbar^2}{g_S \mu_B} = 11.7\,\mathrm{mT}$ is the critical field, while $\varepsilon_D = \frac{g_I \mu_K}{g_S \mu_B} = 2.3 \cdot 10^{-4} \ll 1$.
In the representation $|\,\mathbf{S}^2, \mathbf{I}^2; m_S, m_I\,\rangle$ (where m_S and m_I refer again to S_z e I_z), a basis can be written as

$$
|\uparrow 1\rangle \quad , \quad |\uparrow 0\rangle \quad , \quad |\uparrow -1\rangle \quad , \quad |\downarrow 1\rangle \quad , \quad |\downarrow 0\rangle \quad , \quad |\downarrow -1\rangle \tag{1.21}
$$

where the arrow refers to the electron spin.
Following the same scheme applied for hydrogen, the spin-spin interaction term results:

$$\mathbf{S}\cdot\mathbf{I} = \frac{\hbar^2}{2}\begin{pmatrix} 1 & 0 & 0 & 0 & 0 & 0 \\ 0 & 0 & 0 & 0 & 0 & \sqrt{2} \\ 0 & 0 & -1 & 0 & \sqrt{2} & 0 \\ 0 & 0 & 0 & 1 & 0 & 0 \\ 0 & 0 & \sqrt{2} & 0 & 0 & 0 \\ 0 & \sqrt{2} & 0 & 0 & 0 & -1 \end{pmatrix} \tag{1.22}$$

while the external magnetic field interaction terms can be expressed by

$$\frac{3}{2}\frac{\mathbf{B}}{B_C^D}\cdot\mathbf{S} = \frac{3}{2}\frac{\hbar}{2}\begin{pmatrix} x & 0 & 0 & 0 & 0 & 0 \\ 0 & x & 0 & 0 & 0 & 0 \\ 0 & 0 & x & 0 & 0 & 0 \\ 0 & 0 & 0 & -x & 0 & 0 \\ 0 & 0 & 0 & 0 & -x & 0 \\ 0 & 0 & 0 & 0 & 0 & -x \end{pmatrix} \tag{1.23}$$

and

$$\frac{3}{2}\frac{\mathbf{B}}{B_C^D}\cdot\mathbf{I} = \frac{3}{2}\hbar\begin{pmatrix} x & 0 & 0 & 0 & 0 & 0 \\ 0 & 0 & 0 & 0 & 0 & 0 \\ 0 & 0 & -x & 0 & 0 & 0 \\ 0 & 0 & 0 & -x & 0 & 0 \\ 0 & 0 & 0 & 0 & 0 & 0 \\ 0 & 0 & 0 & 0 & 0 & x \end{pmatrix} \tag{1.24}$$

Finally, the matrix form of the Hamiltonian (1.20) is given by

$$\mathcal{H}_0^{st} = \frac{A_D\hbar^2}{2}\begin{pmatrix} 1+\frac{3}{2}x(1-2\varepsilon_D) & 0 & 0 & 0 & 0 & 0 \\ 0 & \frac{3}{2}x & 0 & 0 & 0 & \sqrt{2} \\ 0 & 0 & -1+\frac{3}{2}x(1+2\varepsilon_D) & 0 & \sqrt{2} & 0 \\ 0 & 0 & 0 & 1-\frac{3}{2}x(1-2\varepsilon_D) & 0 & 0 \\ 0 & 0 & \sqrt{2} & 0 & -\frac{3}{2}x & 0 \\ 0 & \sqrt{2} & 0 & 0 & 0 & -1-\frac{3}{2}x(1+2\varepsilon_D) \end{pmatrix} \tag{1.25}$$

The matrix (1.25) can be diagonalized by applying the orthogonal transformation (1.11), with U_0 now given by

$$U_0 = \begin{pmatrix} 1 & 0 & 0 & 0 & 0 & 0 \\ 0 & \cos\theta_+ & 0 & 0 & 0 & 0 \\ 0 & 0 & \cos\theta_- & 0 & -\sin\theta_+ & 0 \\ 0 & 0 & 0 & 1 & 0 & 0 \\ 0 & 0 & \sin\theta_- & 0 & \cos\theta_- & 0 \\ 0 & \sin\theta_+ & 0 & 0 & 0 & \cos\theta_+ \end{pmatrix} \tag{1.26}$$

where

$$\begin{aligned} \cos\theta_\pm &= \sqrt{\tfrac{1}{2}(1+\cos 2\theta_\pm)} & \sin\theta_\pm &= \sqrt{\tfrac{1}{2}(1-\cos 2\theta_\pm)} \\ \cos 2\theta_\pm &= \frac{3x(1+2\varepsilon_D)\pm 1}{\sqrt{(3x(1+2\varepsilon_D)\pm 1)^2+8}} & \sin 2\theta_\pm &= \frac{\sqrt{8}}{\sqrt{(3x(1+2\varepsilon_D)\pm 1)^2+8}} \end{aligned} \tag{1.27}$$

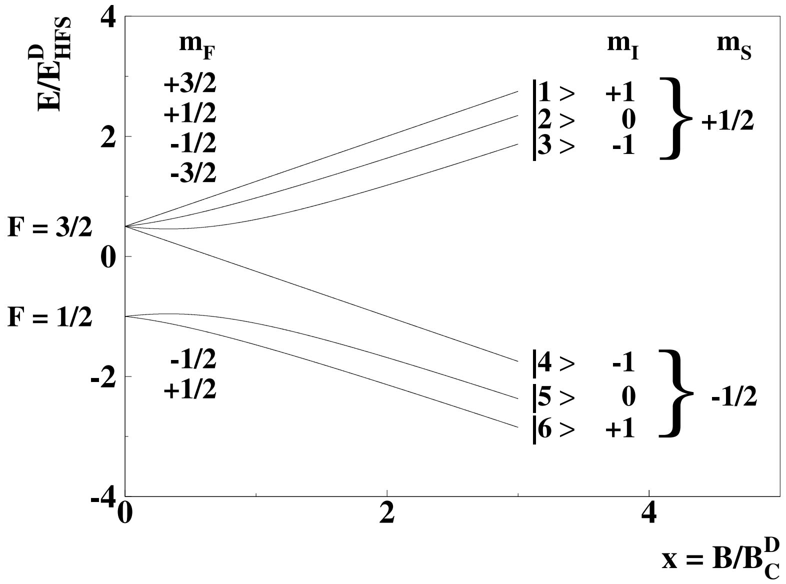

Figure 1.3:
Breit-Rabi diagram of deuterium. The energy and the magnetic field values are expressed as adimensional variables like in figure 1.1.

are the relations from which one can derive the mixing angles θ_- e θ_+.
The eigenenergies of the static Hamiltonian are:

$$\begin{aligned}
E_1 &= \frac{E^D_{HFS}}{3}\left(1 + \frac{3}{2}x(1 - 2\varepsilon_D)\right) \\
E_2 &= \frac{E^D_{HFS}}{6}\left(-1 + \sqrt{9x^2(1 + 2\varepsilon_D)^2 + 6x(1 + 2\varepsilon_D) + 9}\right) \\
E_3 &= \frac{E^D_{HFS}}{6}\left(-1 + \sqrt{9x^2(1 + 2\varepsilon_D)^2 - 6x(1 + 2\varepsilon_D) + 9}\right) \\
E_4 &= \frac{E^D_{HFS}}{3}\left(1 - \frac{3}{2}x(1 - 2\varepsilon_D)\right) \\
E_5 &= \frac{E^D_{HFS}}{6}\left(-1 - \sqrt{9x^2(1 + 2\varepsilon_D)^2 - 6x(1 + 2\varepsilon_D) + 9}\right) \\
E_6 &= \frac{E^D_{HFS}}{6}\left(-1 - \sqrt{9x^2(1 + 2\varepsilon_D)^2 + 6x(1 + 2\varepsilon_D) + 9}\right)
\end{aligned} \tag{1.28}$$

with $E^D_{HFS} = \frac{3}{2}A_D\hbar^2 = 1.35 \cdot 10^{-6}\,\text{eV}$, whereas the correspondent frequency is given by $\nu^D_{HFS} = 327.4\,\text{MHz}$.
The deuterium energy levels are plotted in figure 1.3 as functions of the external magnetic field. The interpretation of the critical field given for the hydrogen case is still valid.
The basis of eigenstates correspondent to the eigenvalues (1.28) is:

$$\begin{aligned}
|\,1\,\rangle &= |\uparrow +1\,\rangle & |\,4\,\rangle &= |\downarrow -1\,\rangle \\
|\,2\,\rangle &= \cos\theta_+\,|\uparrow 0\,\rangle + \sin\theta_+\,|\downarrow +1\,\rangle & |\,5\,\rangle &= \sin\theta_-\,|\uparrow -1\,\rangle - \cos\theta_-\,|\downarrow 0\,\rangle \\
|\,3\,\rangle &= \cos\theta_-\,|\uparrow -1\,\rangle + \sin\theta_-\,|\downarrow 0\,\rangle & |\,6\,\rangle &= \sin\theta_+\,|\uparrow 0\,\rangle - \cos\theta_+\,|\downarrow +1\,\rangle
\end{aligned} \tag{1.29}$$

Only the first and the fourth are pure states (i.e. polarized). The polarization of the remaining states depends on the values of the mixing angles θ_+ e θ_-.

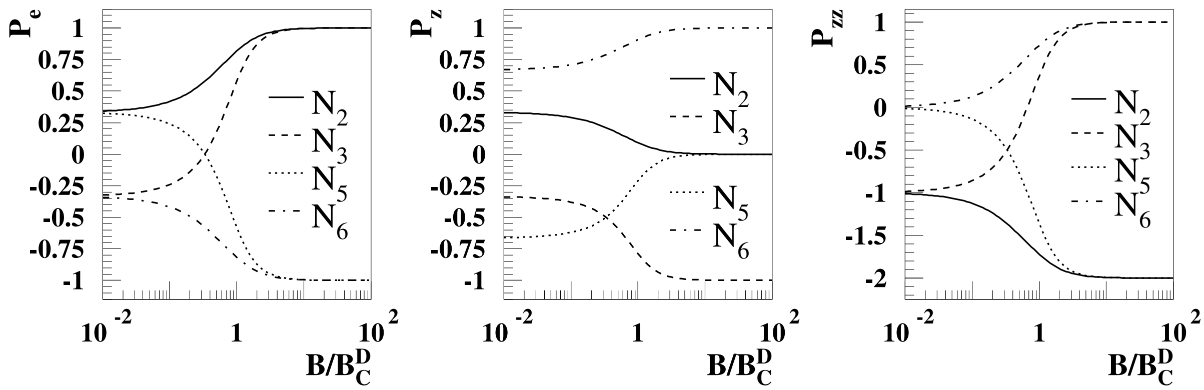

Figure 1.4: The electron (left), nuclear (center) and tensor polarizations of the four non-pure deuterium hyperfine states as functions of the external magnetic field. The polarizations of the pure states $|\,1\,\rangle$ and $|\,4\,\rangle$ do not depend on the strength of B.

Polarization definitions

The polarization of electrons P_e and nuclei P_z are given by

$$\begin{aligned} P_e &= \sum_{i=1}^{6} n_i \,\langle\, i \,|\, \frac{2}{\hbar} S_z \,|\, i\,\rangle = n_1 - n_4 + (n_2 - n_6)\cos 2\theta_+ + (n_3 - n_5)\cos 2\theta_- \qquad (1.30) \\ P_z &= \sum_{i=1}^{6} n_i \,\langle\, i \,|\, \frac{1}{\hbar} I_z \,|\, i\,\rangle = n_1 + n_6 - n_3 - n_4 + (n_2 - n_6)\sin^2\theta_+ + (n_3 - n_5)\sin^2\theta_- \end{aligned}$$

As the deuteron has spin $I = 1$, $m_I = 0, \pm 1$, the *vector polarization* P_z alone does not entirely describe its spin state. In order to complete the nuclear spin representation of deuterium one usually employs the *tensor polarization* P_{zz}, defined as the z-z component of the tensor operator $I_{ij} = \frac{3}{2}(I_i I_j + I_j I_i) - 2\delta_{ij}$ [Fic71]. The tensor polarization of the deuteron is then given by:

$$P_{zz} = \langle\, I_{zz} \,\rangle = \left\langle\, 3I_z^2 - 2 \,\right\rangle \qquad (1.31)$$

and hence:

$$P_{zz} = n_1 + n_4 - \frac{1}{2}(n_2 + n_3 + n_5 + n_6) - \frac{3}{2}(n_2 - n_6)\cos 2\theta_+ + \frac{3}{2}(n_3 - n_5)\cos 2\theta_- \qquad (1.32)$$

The polarizations for the different deuterium hyperfine states are plotted in figure 1.4 as functions of the applied magnetic field.

1.2 Hyperfine transitions

Let us consider once more the Hamilton operator (1.1) applying the Schrödinger equation to one of its eigenstates Ψ:

$$i\hbar \frac{\partial}{\partial t}\Psi = \mathcal{H}\Psi \qquad (1.33)$$

If one multiplies from the left the orthonormal operator U_0 (see eq. 1.12 or 1.26), one has:

$$i\hbar\left(\frac{\partial}{\partial t}U_0^T\Psi + U_0^T\frac{\partial}{\partial t}\Psi\right) = \left(U_0^T\mathcal{H} + i\hbar\frac{\partial}{\partial t}U_0^T\right)\Psi \tag{1.34}$$

Applying $U_0^T U_0 = \mathbf{1}$ in the second member of (1.34), one obtains:

$$i\hbar\left(\frac{\partial}{\partial t}U_0^T\Psi + U_0^T\frac{\partial}{\partial t}\Psi\right) = \left(U_0^T\mathcal{H}U_0 + i\hbar\frac{\partial}{\partial t}U_0^T U_0\right)U_0^T\Psi \tag{1.35}$$

Finally, changing basis by means of the transformation $\Phi = U^T\Psi$, one has:

$$i\hbar\frac{\partial}{\partial t}\Phi = \left(\mathcal{H}_1^{st} + i\hbar\frac{\partial}{\partial t}U_0^T U_0\right)\Phi \tag{1.36}$$

where $\mathcal{H}_1^{st}$ represents the diagonal static Hamiltonian, already encountered in the previous section.

The term $i\hbar\frac{\partial}{\partial t}U_0^T U_0$ is non-zero if the external magnetic field is time dependent. In such a case, the resulting distortion of the eigenstates may originate transitions between pairs of hyperfine states.

Each transition is characterized by a defined frequency ν_{ab} related to the energy difference between the two hyperfine states:

$$\nu_{ab} = \frac{|E_a - E_b|}{2\pi\hbar} \tag{1.37}$$

The holding field dependence of the energy levels (see eq. (1.14) and (1.28)) is of course transferred to the transition frequencies.

Hyperfine transitions can be classified depending on the relative orientations of the static holding field $\mathbf{B}^{st}$ and the time dependent one $\mathbf{B}(t)$. Transitions caused by the component of $\mathbf{B}(t)$ parallel to the static one are called σ, whereas transitions generated by the perpendicular component of $\mathbf{B}(t)$ are called π.

A further possible classification of hyperfine transitions will be discussed in section 1.2.4.

1.2.1 Hydrogen

Let us consider an external magnetic field having the following form:

$$\mathbf{B} = (0, 0, B^{st} + b(t)) \tag{1.38}$$

so that the static component of the field B^{st} and the time dependent one $b(t)$ are parallel. Choosing $b(t) = b_{\|}\cos\nu t$, the time dependent part of the hydrogen Hamiltonian contained in (1.36) becomes

$$\mathcal{H}_1^{\sigma} = i\hbar\begin{pmatrix} 0 & 0 & 0 & 0 \\ 0 & s\dot{s}+c\dot{c} & 0 & -s\dot{c}+c\dot{s} \\ 0 & 0 & 0 & 0 \\ 0 & s\dot{c}-c\dot{s} & 0 & s\dot{s}+c\dot{c} \end{pmatrix} = \frac{i\hbar\nu}{2}y_\sigma \sin\nu t\begin{pmatrix} 0 & 0 & 0 & 0 \\ 0 & 0 & 0 & \sin^2\theta \\ 0 & 0 & 0 & 0 \\ 0 & -\sin^2\theta & 0 & 0 \end{pmatrix} \tag{1.39}$$

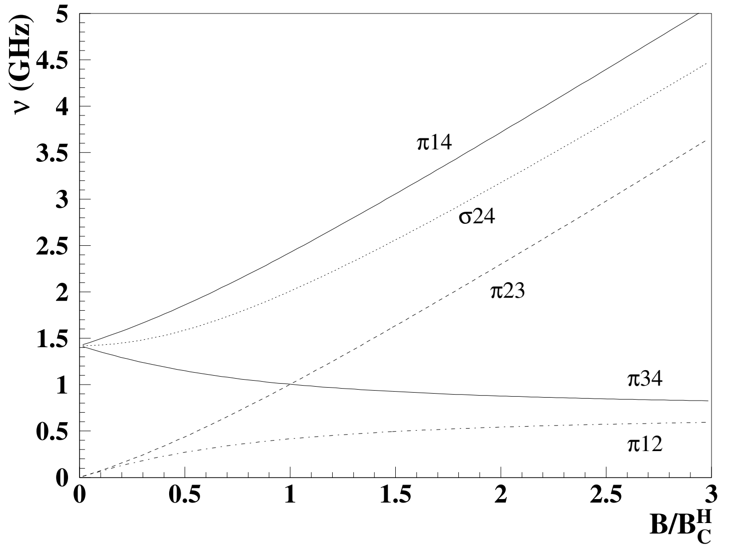

Figure 1.5:
Frequencies of hydrogen hyperfine transitions plotted as functions of the holding field. The field values are normalized to the critical field B_C^H.

where $c = \cos\theta$, $s = \sin\theta$, $y_\sigma = \frac{b_\parallel}{B_C^H}$ and the constant $\varepsilon_H \ll 1$ has been neglected.
Hence, the superposition of a time dependent magnetic field parallel to the holding field results in the connection of hyperfine states $|\,2\,\rangle$ and $|\,4\,\rangle$ of hydrogen. This leads to the possible transition

$$\sigma\,|\,2\,\rangle \leftrightarrow |\,4\,\rangle \qquad\qquad (\Delta F = \pm 1, \Delta m_F = 0)$$

Let us choose now the time-dependent component of the field to be perpendicular to the holding field so that $b(t)$ is either directed along x or along y. In order to describe this scenario, one has to rewrite the matrix form of the Hamilton operator (1.2) in the following way:

$$\mathcal{H}_0 = \mathcal{H}_0^{st} + \mathcal{H}_0^{\pi} \tag{1.40}$$

where $\mathcal{H}_0^{st}$ designates the static part of the Hamiltonian and the index 0 denotes the representation given by the basis (1.3).
By applying the orthogonal transformation (1.12) to $\mathcal{H}_0^{\pi}$, one finds:

$$\mathcal{H}_1^{\pi} = U_0^T \mathcal{H}_0^{\pi} U_0 \tag{1.41}$$

If one aligns the time dependent field along x[1], so that

$$\mathbf{B} = (b(t), 0, B_z^{st}) \tag{1.42}$$

defining $b(t) = b_\perp \cos(\nu t)$ and neglecting the constant $\varepsilon_H \ll 1$, one finds

$$\mathcal{H}_1^{\pi} \simeq i\frac{E_{HFS}^H}{2} y_\pi \cos\nu t \begin{pmatrix} 0 & \sin\theta & 0 & -\cos\theta \\ \sin\theta & 0 & -\cos\theta & 0 \\ 0 & \cos\theta & 0 & -\sin\theta \\ \cos\theta & 0 & -\sin\theta & 0 \end{pmatrix} \tag{1.43}$$

[1]Selecting $b(t)$ along y would lead to the same conclusions.

where $y_\pi = \frac{b_\perp}{B_C^H}$.
Thus, from the (1.43) one can conclude that the presence of a time dependent field perpendicular to the static one connects the four pairs of hyperfine states, leading to the following possible transitions:

$$
\begin{array}{ll}
\pi\,|\,1\,\rangle \leftrightarrow |\,2\,\rangle & (\Delta F = 0, \Delta m_F = \pm 1) \\
\pi\,|\,2\,\rangle \leftrightarrow |\,3\,\rangle & (\Delta F = 0, \Delta m_F = \pm 1) \\
\pi\,|\,1\,\rangle \leftrightarrow |\,4\,\rangle & (\Delta F = \pm 1, \Delta m_F = \pm 1) \\
\pi\,|\,3\,\rangle \leftrightarrow |\,4\,\rangle & (\Delta F = \pm 1, \Delta m_F = \pm 1)
\end{array}
$$

In figure 1.5 the resonance frequencies of all hydrogen transitions are plotted as function of the holding field.

1.2.2 Deuterium

By choosing the time dependent field $b(t) = b_\parallel \cos \nu t$ to be parallel to the static one and neglecting the constant $\varepsilon_D \ll 1$, one gets:

$$
\mathcal{H}_1^\sigma = i\hbar \begin{pmatrix}
0 & 0 & 0 & 0 & 0 & 0 \\
0 & s_+\dot{s}_+ + c_+\dot{c}_+ & 0 & 0 & 0 & -s_+\dot{c}_+ + c_+\dot{s}_+ \\
0 & 0 & s_+\dot{s}_- + c_+\dot{c}_- & 0 & -s_-\dot{c}_- + c_-\dot{s}_- & 0 \\
0 & 0 & 0 & 0 & 0 & 0 \\
0 & 0 & s_-\dot{c}_- - c_-\dot{s}_- & 0 & s_+\dot{s}_- + c_+\dot{c}_- & 0 \\
0 & s_+\dot{c}_+ - c_+\dot{s}_+ & 0 & 0 & 0 & s_+\dot{s}_- + c_+\dot{c}_-
\end{pmatrix} =
$$

$$
= \frac{3i\hbar\nu}{4\sqrt{2}} y_\sigma \sin \nu t \begin{pmatrix}
0 & 0 & 0 & 0 & 0 & 0 \\
0 & 0 & 0 & 0 & 0 & \sin^2 2\theta \\
0 & 0 & 0 & 0 & \sin^2 2\theta & 0 \\
0 & 0 & 0 & 0 & 0 & 0 \\
0 & 0 & -\sin^2 2\theta & 0 & 0 & 0 \\
0 & -\sin^2 2\theta & 0 & 0 & 0 & 0
\end{pmatrix} \tag{1.44}
$$

where $c_\pm = \cos \theta_\pm$ and $s_\pm = \sin \theta_\pm$.
Thus, in case of deuterium there are two possible σ transitions:

$$
\begin{array}{ll}
|\,2\,\rangle \leftrightarrow |\,6\,\rangle & (\Delta F = \pm 1, \Delta m_F = 0) \\
|\,3\,\rangle \leftrightarrow |\,5\,\rangle & (\Delta F = \pm 1, \Delta m_F = 0)
\end{array}
$$

The effect of the superposition of a time dependent field $b(t) = b_\perp \cos \nu t$ perpendicular to the static one can be analyzed like in the hydrogen case. Neglecting again $\varepsilon_D \ll 1$, one finds:

$$
\mathcal{H}_1^\pi = i\frac{E_{HFS}^2}{2} y_\pi \cos \nu t \begin{pmatrix}
0 & -s_+ & 0 & 0 & 0 & -c_- \\
s_+ & 0 & -s_-c_+ & 0 & -c_-c_+ & 0 \\
0 & s_-c_+ & 0 & -c_- & 0 & -s_-s_+ \\
0 & 0 & c_- & 0 & -s_- & 0 \\
0 & c_-c_+ & 0 & s_- & 0 & -s_+c_- \\
c_+ & 0 & s_-s_+ & 0 & s_+c_- & 0
\end{pmatrix} \tag{1.45}
$$

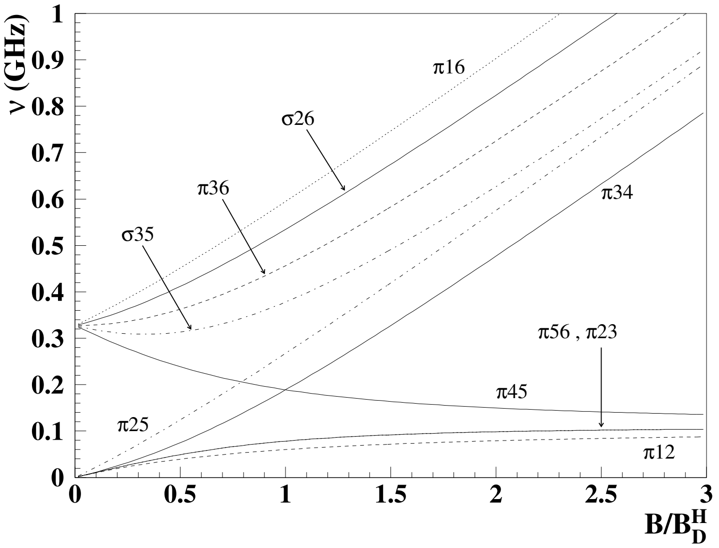

Figure 1.6:
Frequencies of deuterium hyperfine transitions plotted as functions of the holding field. The field values are normalized to the critical field B_D^H.

where again the shortcuts $s_\pm = \sin\theta_\pm$ e $c_\pm = \cos\theta_\pm$ have been applied.
Eight π transitions are thus allowed in case of deuterium:

$$
\begin{array}{ll}
|\,1\,\rangle \leftrightarrow |\,2\,\rangle & (\Delta F = 0, \Delta m_F = \pm 1) \\
|\,2\,\rangle \leftrightarrow |\,3\,\rangle & (\Delta F = 0, \Delta m_F = \pm 1) \\
|\,3\,\rangle \leftrightarrow |\,4\,\rangle & (\Delta F = 0, \Delta m_F = \pm 1) \\
|\,5\,\rangle \leftrightarrow |\,6\,\rangle & (\Delta F = 0, \Delta m_F = \pm 1) \\
|\,1\,\rangle \leftrightarrow |\,6\,\rangle & (\Delta F = \pm 1, \Delta m_F = \pm 1) \\
|\,2\,\rangle \leftrightarrow |\,5\,\rangle & (\Delta F = \pm 1, \Delta m_F = \pm 1) \\
|\,3\,\rangle \leftrightarrow |\,6\,\rangle & (\Delta F = \pm 1, \Delta m_F = \pm 1) \\
|\,4\,\rangle \leftrightarrow |\,5\,\rangle & (\Delta F = \pm 1, \Delta m_F = \pm 1)
\end{array}
$$

The holding field dependence of the deuterium hyperfine transitions is shown in figure 1.6.

1.2.3 Transition probability

If the strength of the time dependent field is small compared to the intensity of the static holding field, then the additional potential can be treated perturbatively. In such a case, for a fixed interaction time τ, the transition probability between states $|\,a\,\rangle$ and $|\,b\,\rangle$ for an atom is given at the first perturbative order by [Mes61, Coh77]:

$$W_{ab} \simeq \left(\frac{y_{\pi,\sigma} E_{HFS}}{\hbar}\right)^2 |V_{ab}|^2 f(\nu - \nu_{ab}, \tau) \tag{1.46}$$

where the matrix element V_{ab} is defined like

$$V_{ab} = \frac{\langle\, i\,|\,\mathcal{H}_1^{\pi,\sigma}\,|\,n\,\rangle}{\bar{y}_{\pi,\sigma} E_{HFS}} \tag{1.47}$$

with $\bar{y}_{\pi,\sigma} = \frac{b_{(t)}}{B_C}$.
For a periodic field $b(t) = b_{\parallel,\perp} \cos \nu t$, the function $f(\nu - \nu_{ab}, \tau)$ is given by:

$$f(\nu - \nu_{ab}, \tau) = 4\frac{\sin^2 \frac{(\nu-\nu_{ab})\tau}{2}}{(\nu - \nu_{ab})^2} \tag{1.48}$$

Figure 1.7 shows the behavior of (1.48) for a fixed time τ. The function is basically zero outside the range $|\nu - \nu_{ab}| \leq \frac{2\pi}{\tau}$, whereas it reaches its maximum value τ^2 at the *resonance condition*

$$\lim_{\nu \to \nu_{ab}} f(\nu - \nu_{ab}, \tau) = \tau^2 \tag{1.49}$$

If (1.49) holds, the transition probability becomes

$$W_{ab} \simeq \nu^2_{HFS} y^2_{\pi,\sigma} |V_{ab}|^2 \tau^2 \tag{1.50}$$

Through the relations $\nu_{HFS} = \frac{E_{HFS}}{\hbar}$, $y_{\pi,\sigma} = \frac{b_{x,y}}{B_C}$ (where $b_{x,y}$ represents the amplitude of the oscillating field) and $B_C = \frac{E_{HFS}}{g_S \mu_B}$, the (1.50) can be written like the following:

$$W_{ab} \simeq \left(\frac{\mu_B}{\hbar}\right) b^2_{x,y} |V_{ab}|^2 g^2_S \tau^2 \tag{1.51}$$

One can now conclude that, at the resonance condition, the transition probability between two hyperfine states $|\, a \,\rangle$ and $|\, b \,\rangle$ due to the presence of an oscillating magnetic field depends quadratically on:

- the amplitude of the time dependent oscillating magnetic field;
- the matrix element $|V_{ab}|$, function of the static holding field;

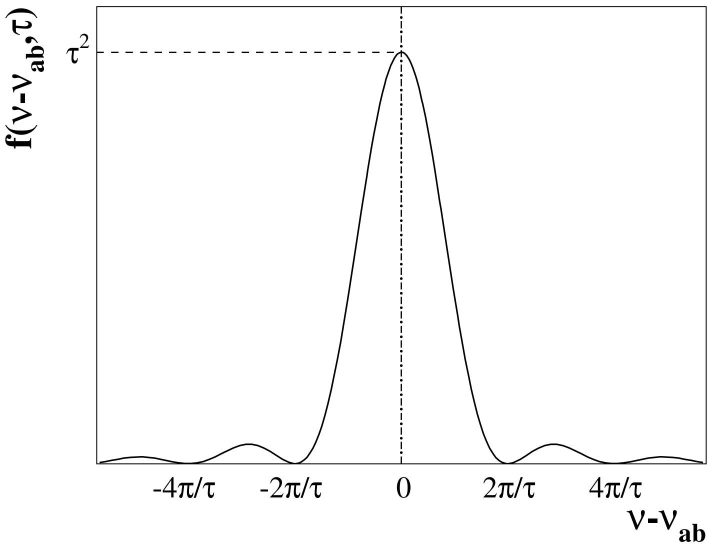

Figure 1.7:
The function $f(\nu - \nu_{ab}, \tau)$ at fixed τ. The expression $\nu - \nu_{ab} = \frac{2\pi}{\tau} n$ $(n = \pm 1, \pm 2, ...)$ defines the zeros of the function. At the resonant condition $\nu = \nu_{ab}$, $f(\nu - \nu_{ab}, \tau) = \tau^2$.

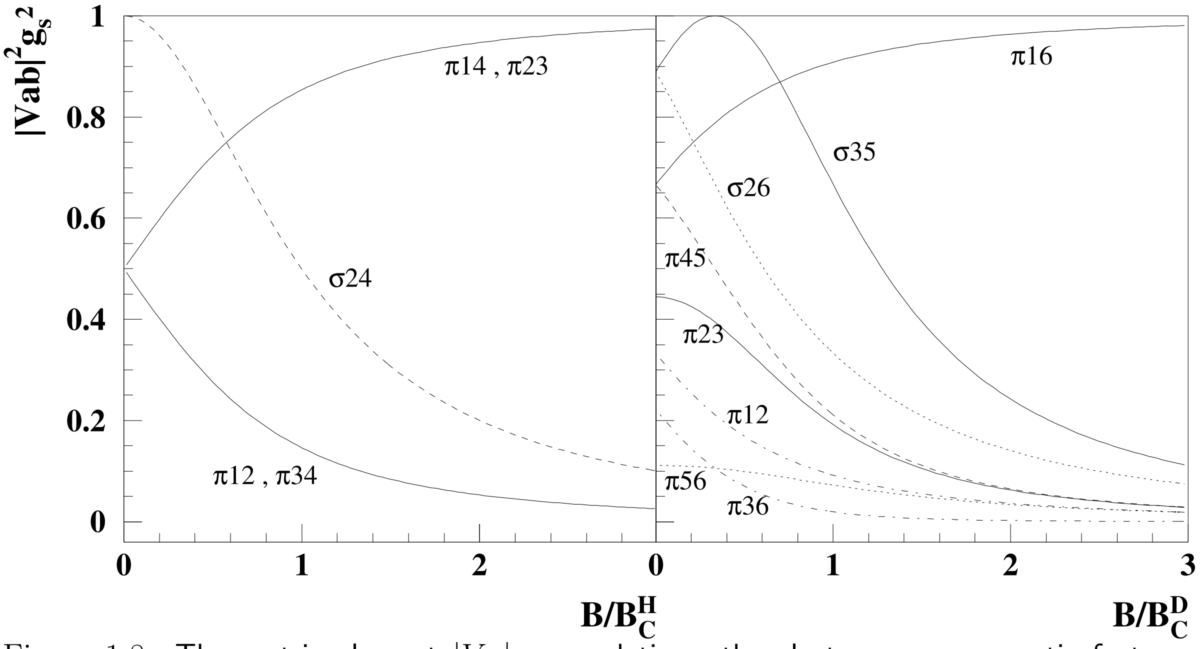

Figure 1.8: The matrix element $|V_{ab}|$ squared times the electron gyro-magnetic factor g_S squared for hydrogen (left) and deuterium hyperfine transitions (transitions $\pi 26$ and $\pi 34$ are not shown because very close to the $\pi 16$ curve). At any given holding field, this quantity expresses the relative probability of the different transitions.

- the time τ during which the atom experiences the oscillating field.

The quantity $|V_{ab}|^2 g_s^2$ for hydrogen and deuterium hyperfine transitions is shown in figure 1.8 as function of the static holding field.

1.2.4 Adiabatic high frequency transitions

In the last section it has been shown that an atom in hyperfine state $|\,a\,\rangle$ experiencing a periodic magnetic field with frequency $\nu \simeq \nu_{ab}$ can undergo a transition toward the hyperfine state $|\,b\,\rangle$. If the interaction time τ is long ($\tau >> \frac{1}{\nu}$), the atom oscillates between the two energy levels with a period $t = \pi/\nu$. It follows that, among an ensemble of atoms, the exchange between two hyperfine states is possible only by fixing the interaction time of each atom, a condition not possible to fulfill within a jet of particle with thermal velocity distribution[2].

An efficient exchange between two hyperfine states can be performed by means of a so-called *adiabatic high frequency transition* (HFT) [Abr58, Hae67, Oh70, Phi87], where a gradient field along the axis of the atomic beam ensures that the resonance condition is met only at one particular position for each atom. A detailed calculation of the adiabatic

[2]This is the case inside the atomic beam source and the atomic polarimeter of the HERMES target, as it will be shown in chapter 2.

Hamiltonian and its diagonalization can be found in [Bau00]. With this method, transition efficiencies very close to 100 % can be reached with a resonant region of a few cm length.

Adiabatic high frequency transitions are usually distinguished between strong field transitions (SFTs), with $\Delta m_F = 1$, and medium or weak field transitions (MFTs/WFTs), with $\Delta m_F = 0$ [Hlm71, Oh70, Dre83, Rob92]. In order to fill the energy gap between two different Zeeman multiplets, SFTs have to run at frequencies in the order of $\nu_{HFS} = E_{HFS}/2\pi\hbar$ or higher. This condition is usually realized by means of resonator cavities. MFTs/WFTs exchange hyperfine states within the same multiplet, so that the required frequency is approximately proportional to the applied static magnetic field. Therefore, high frequency coils are usually adequate to achieve MFT/WFT transition units.

In order to describe the hyperfine population exchange between two given states $|\,a\,\rangle$ and $|\,b\,\rangle$ undergone by an atomic beam when passing through a HFT, one can use the efficiency matrix T_{ab}:

$$N_a = \sum_b T_{ab} N_b \tag{1.52}$$

where N_b and N_a are the populations vectors $N_i = (N_1, N_2, ...)^T$ before and after the HFT.

In case of a transition SFT 2-4 the matrix T_{24} can be written as follows:

Orientation	σ/π	Type	Δm_F	ΔF	Δm_I	Δm_S	Hydrogen	Deuterium
$B(t)\|B^{st}$	σ	SFT	0	±1	±1	±1	$2 \leftrightarrow 4$	$2 \leftrightarrow 6$
$B(t)\|B^{st}$	σ	SFT	0	±1	±1	±1		$3 \leftrightarrow 5$
$B(t)\perp B^{st}$	π	SFT	±1	±1	0	±1	$1 \leftrightarrow 4$	$1 \leftrightarrow 6$
$B(t)\perp B^{st}$	π	SFT	±1	±1	0	±1		$2 \leftrightarrow 5$
$B(t)\perp B^{st}$	π	SFT	±1	±1	±2	±1		$3 \leftrightarrow 6$
$B(t)\perp B^{st}$	π	SFT	±1	±1	±1	0	$3 \leftrightarrow 4$	$4 \leftrightarrow 5$
$B(t)\perp B^{st}$	π	MFT	±1	0	±1	0	$1 \leftrightarrow 2$	$1 \leftrightarrow 2$
$B(t)\perp B^{st}$	π	MFT	±1	0	±1	0		$2 \leftrightarrow 3$
$B(t)\perp B^{st}$	π	MFT	±1	0	±1	0		$5 \leftrightarrow 6$
$B(t)\perp B^{st}$	π	MFT	±1	0	0	±1	$2 \leftrightarrow 3$	
$B(t)\perp B^{st}$	π	MFT	±1	0	0	±1		$3 \leftrightarrow 4$

Table 1.1: Hyperfine transitions of hydrogen and deuterium and their features. The values Δm_I and Δm_S are valid in the high holding field regime, where the eigenstates of the static Hamiltonian can be approximated by (1.3) for hydrogen and (1.21) for deuterium.

$$T_{24} = \begin{pmatrix} 1 & 0 & 0 & 0 \\ 0 & 1-\varepsilon_{42} & 0 & \varepsilon_{42} \\ 0 & 0 & 1 & 0 \\ 0 & \varepsilon_{24} & 0 & 1-\varepsilon_{24} \end{pmatrix} \tag{1.53}$$

where $\varepsilon_{24} = \varepsilon_{42}$ is the efficiency of the transition unit.
While SFTs are always single step transitions, MFTs/WFTs are usually employed as multiple transitions. Depending on the strength and gradient of the static field, a MFT/WFT unit can be tuned in order to perform subsequent transitions within the same resonant region[3]. For example, the deuterium transition unit MFT 1-4 with negative gradient can be represented, in the ideal case of 100 % efficiency, in the following way:

$$\begin{pmatrix} N_1 \\ N_2 \\ N_3 \\ N_4 \\ N_5 \\ N_6 \end{pmatrix} \xrightarrow{1\leftrightarrow 2} \begin{pmatrix} N_2 \\ N_1 \\ N_3 \\ N_4 \\ N_5 \\ N_6 \end{pmatrix} \xrightarrow{2\leftrightarrow 3} \begin{pmatrix} N_2 \\ N_3 \\ N_1 \\ N_4 \\ N_5 \\ N_6 \end{pmatrix} \xrightarrow{3\leftrightarrow 4} \begin{pmatrix} N_2 \\ N_3 \\ N_4 \\ N_1 \\ N_5 \\ N_6 \end{pmatrix} \tag{1.54}$$

The result does not correspond to the population exchange of states $|\,1\,\rangle$ and $|\,4\,\rangle$, but rather to the rotation of the first four states[4].
The efficiency matrix of a multi step transition unit can be described by the product of the single transitions matrices. In case of the MFT 1-4 with negative gradient one has:

$$T_{14}^{neg} = T_{34}T_{23}T_{12} \tag{1.55}$$

In table 1.1 all the possible single step hyperfine transitions for the hydrogen and deuterium cases are summarized.

1.3 Bunch field induced hyperfine transitions

If an electron or nuclear polarized gas undergoes unwanted hyperfine transitions, a significant loss of polarization can occur. In the HERMES target[5] hydrogen/deuterium hyperfine states are selected and injected into a storage cell. The gas is immersed in a static high magnetic field which provides the target spin direction and, at the same time, ensures high polarization of the mixed hyperfine states by effectively decoupling the electrons and nucleons magnetic moments (see section 1.1). During HERA beam operation (data taking), an additional time dependent field induced by the electron bunched

[3]The difference between the two kind of transitions is that MFTs are operated at higher frequency where it is possible to distinguish and separate each step. On the contrary, WFTs are multi-photon transitions.
[4]By choosing a positive gradient one would obtain a rotation in the opposite direction.
[5]A complete hardware description of the HERMES polarized target is given in chapter 2.

current is present. The field temporal structure can be decomposed in terms of Fourier's harmonics, each of them produces a resonance condition for a particular transition at given holding field values, as shown in section 1.2.3. In order to avoid target depolarization, it is crucial to study the electron beam structure and locate the resonance conditions as functions of the static holding field.

1.3.1 The HERA electron beam structure

The HERA electron beam is composed by 220 bunches, each of them can be filled with $p_b^{max} = 3.6 \cdot 10^{10}$ particles. The revolution frequency is $\nu_L = 47.36\,\mathrm{kHz}$ so that the time between two bunches is $\tau = 96\,\mathrm{ns}$. The longitudinal structure of the single bunch has a Gaussian shape, whose width is made very short ($\sigma_z = 11.3\,\mathrm{mm}$ or, equivalently, $\sigma_t = 37.7\,\mathrm{ps}$) in order to provide optimized luminosity for the collider experiments.
Since usually almost all bunches are filled with nearly the same amount of particles (see figure 1.9), the total beam current can be approximated by a periodic function:

$$I(t) = I_0 \exp\Big[-\frac{t^2}{2{\sigma_t}^2}\Big] \qquad -\frac{\tau}{2} \leq t \leq \frac{\tau}{2} \qquad \tau = 96\,\mathrm{ns} \tag{1.56}$$

where I_0 is the single bunch peak current.
The Fourier analysis of the (1.56) gives the amplitude of the infinite harmonics in which the beam current can be decomposed:

$$a_n(\nu_n) = 2I_{tot} \exp\Big[-\frac{{\nu_n}^2}{2{\sigma_\nu}^2}\Big] \qquad \text{n=1,2,...} \tag{1.57}$$

where I_{tot} is the integrated beam current, n is the harmonic number and $\nu_n = \frac{n}{\tau}$ the correspondent frequency.

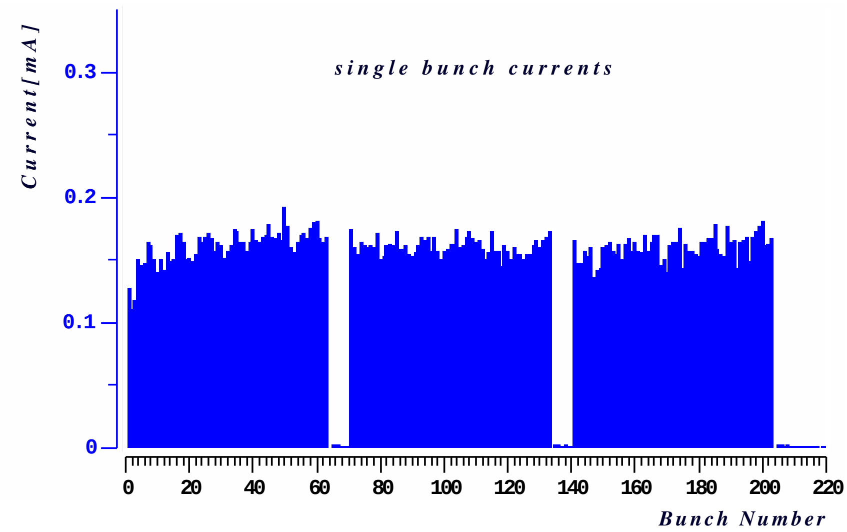

Figure 1.9:
The structure of the HERA electron beam. Typically almost all 220 bunches are filled with approximately the same amount of electrons.

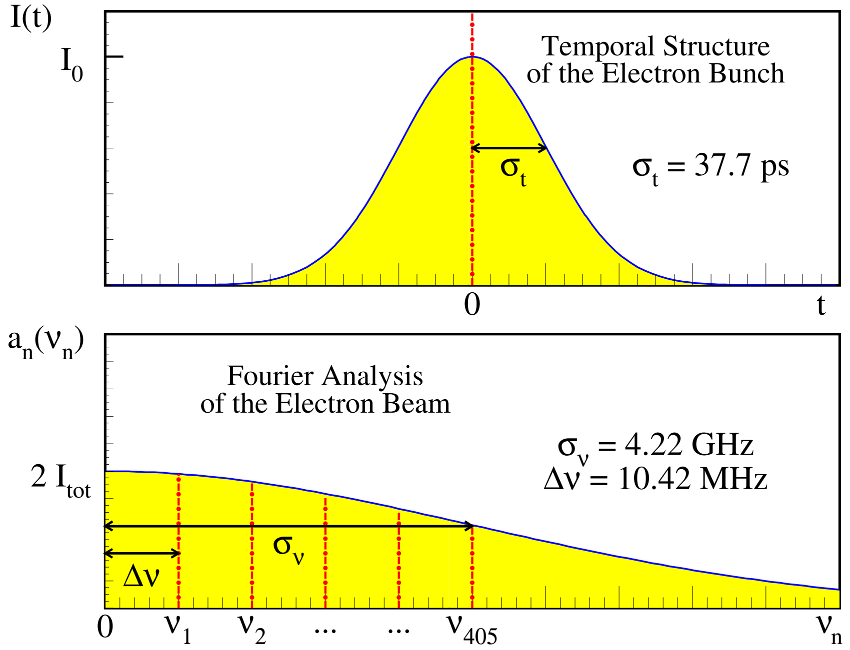

Figure 1.10:
Pictorial view of the temporal current distribution of one of 220 HERA e-beam bunches (top). The Fourier decomposition of the beam current structure gives the amplitude of the induced field harmonics (bottom) as described in the text.

The frequency spacing between two subsequent harmonics is

$$\Delta\nu = \frac{1}{\tau} = 10.42\,\mathrm{MHz} \tag{1.58}$$

On the other hand, the width of the Fourier convolution is given by

$$\sigma_\nu = \frac{1}{2\pi\sigma_t} = 4.22\,\mathrm{GHz} \tag{1.59}$$

Comparing the two values, one may notice that a huge number of harmonics is present whose amplitude is comparable with the one of the fundamental (more than 400 within one sigma.)
All these considerations are summarized in figure 1.10. The same harmonics structure applies of course to the induced electromagnetic field, whose lines "circulate" around the beam axis as shown in figure 1.11.

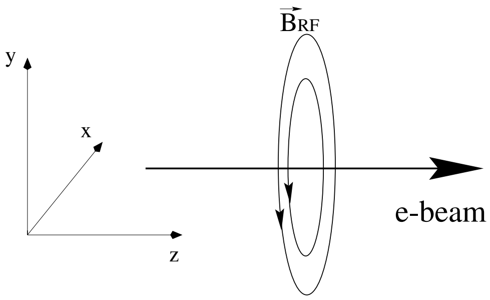

Figure 1.11:
The orientation of the electromagnetic field induced by the HERA beam current. In the drawing, the field direction corresponds to a positron beam.

1.3.2 Resonance conditions

In the storage cell, a resonance condition between a pair of hydrogen or deuterium hyperfine states $|\,a\,\rangle$ and $|\,b\,\rangle$ is met when the frequency difference ν_{ab} between the two states matches the frequency ν_n of one of the beam harmonics (resonance condition):

$$\nu_{ab} = \frac{|E_a - E_b|}{2\pi\hbar} = \nu_n \qquad \text{n=1,2,...} \tag{1.60}$$

where E_a and E_b are the eigenenergies of states $|\,a\,\rangle$ and $|\,b\,\rangle$.
By solving the parametric equation (1.60) as function of the external magnetic field, one finds the holding field values for which a transition between the two states can take place. In a high holding field regime, all hyperfine states are polarized, so that most of the transitions reverse either the nuclear or the electron spin. Only exceptions are the $\sigma\,|\,2\,\rangle \leftrightarrow |\,4\,\rangle$ for hydrogen and $\sigma\,|\,2\,\rangle \leftrightarrow |\,6\,\rangle$, $\sigma\,|\,3\,\rangle \leftrightarrow |\,5\,\rangle$ and $\pi\,|\,3\,\rangle \leftrightarrow |\,6\,\rangle$ for deuterium which change both spins.

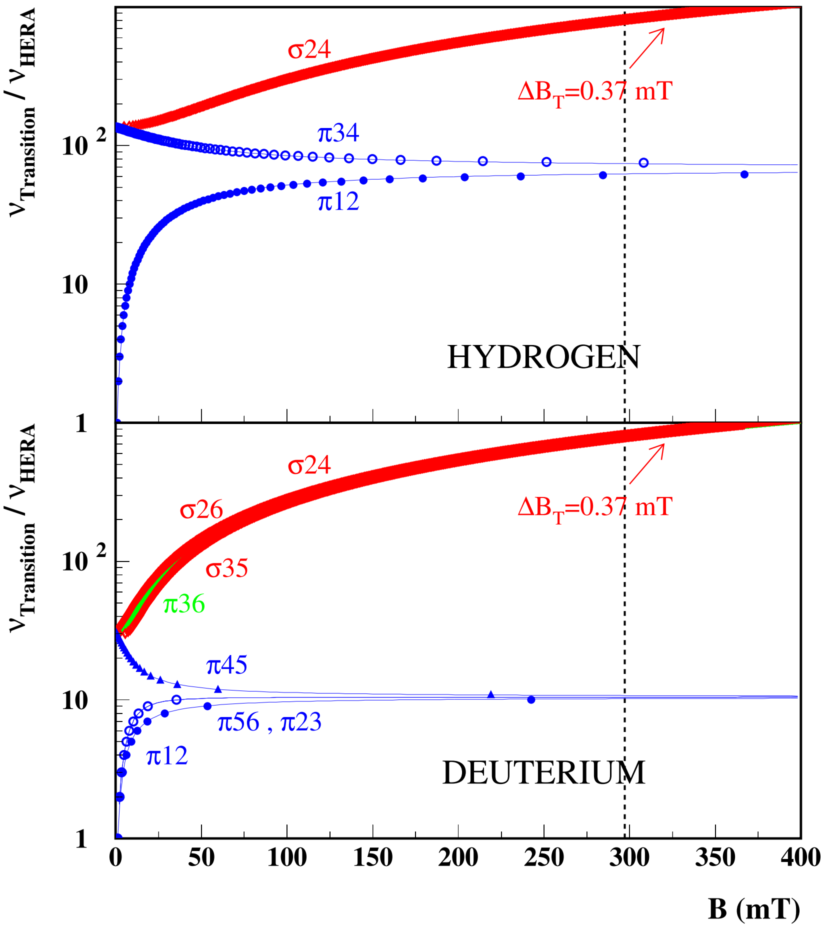

Figure 1.12: Possible beam induced nuclear depolarizing resonances in the HERMES target. The frequency difference between pairs of hydrogen hyperfine states whose transitions lead to nuclear depolarization are plotted as a function of the holding field. The frequency values are normalized to $\nu_{HERA} = 10.42\,$MHz. The marks, representing the resonance condition, are clearly distinguishable for the π transitions, while they overlap with each other in case of σ and $\pi\,|\,3\,\rangle \leftrightarrow |\,6\,\rangle$ transitions. The dashed line represents the working point of the transversely polarized target.

The solution of equation (1.60) is shown in figure 1.12 for all possible nuclear depolarizing transitions[6]. It is interesting to notice the different behavior of the nuclear transitions only, from the one of the transitions reversing additionally the electron spin which are much more densely spaced at high fields. Around the working point of the HERMES target (roughly 300 mT), the interval between two σ or $\pi\,|\,3\,\rangle \leftrightarrow |\,6\,\rangle$ resonances is $\Delta B = 0.37\,\mathrm{mT}$. It is worthwhile to recall here that the the σ transitions are caused by the harmonic field component parallel to the holding field, whereas the π_s are due to the perpendicular harmonic component. Therefore, the σ resonances can happen only if the target field is transverse to the beam direction.
For a given beam current, and assuming that the time during which an atom experiences the oscillating field is fixed, the relative transition probability can be calculated by multiplying the square of the matrix element of the transition (compare figure 1.8) for the amplitude a_n of the harmonic causing the transition. The result is shown in figure 1.13.

[6]Only the nuclear polarization is needed for HERMES data taking purpose.

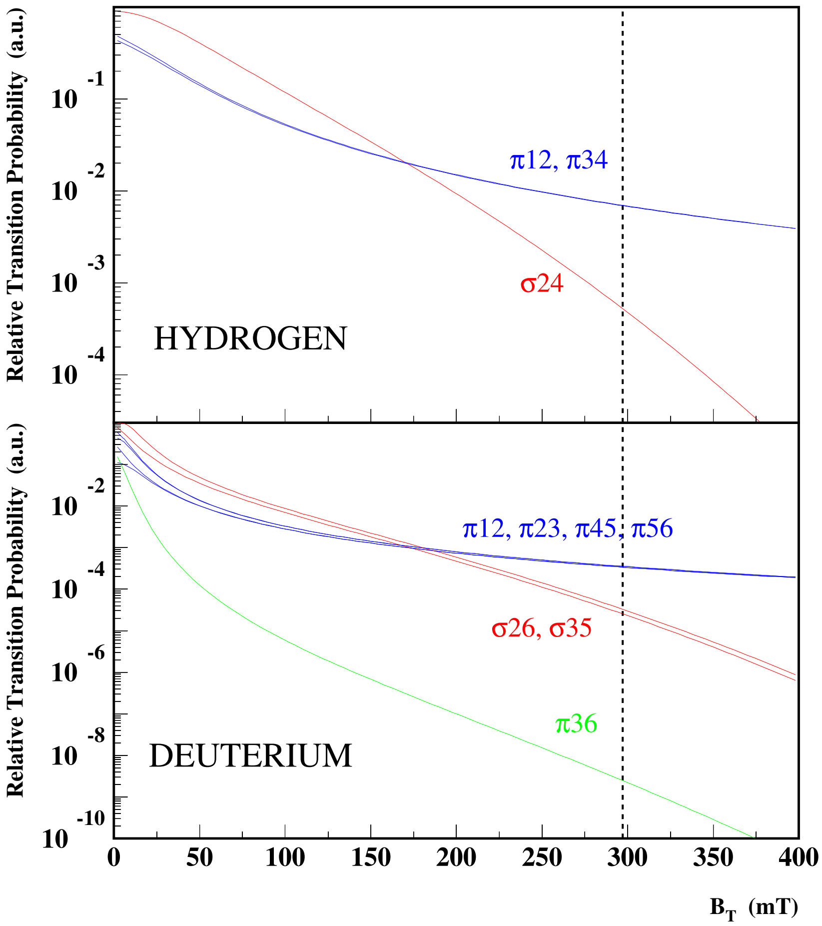

Figure 1.13:
Relative probabilities of the nuclear depolarizing resonances. At the working point of the HERMES transversely polarized target (dashed line), the σ resonances are by roughly one order of magnitude less probable than the nuclear only π. The probability of the $\pi\,|\,3\,\rangle \leftrightarrow |\,6\,\rangle$ is strongly suppressed with respect to all other transitions.

Beam induced depolarization in the HERMES target has already been observed in the longitudinal case [Ack99] where only the π resonances can occur. A transverse target test was performed in spring 1999 but, at that time, an estimation of the effect of the σ resonances was not possible [Reg99]. Some preliminary results about the depolarization due to the σ transition in the recently developed transversely polarized target are shown in section 3.3.1.

1.4 Spin separation in permanent sextupole magnets

An atom with a magnetic dipole moment passing through a magnetic gradient field undergoes the Stern-Gerlach force [Ger21]. Moreover, in case of hydrogen or deuterium, the hyperfine eigenenrgies are modified by the presence of the field as discussed in section 1.1. The Lagrange function for an atom in hyperfine state $|\, a \,\rangle$ is then given by:

$$\mathcal{L} = \frac{m}{2}(\dot{x}^2 + \dot{y}^2 + \dot{z}^2) - E_{|\,a\,\rangle}(|\mathbf{B}|) \tag{1.61}$$

In case of a permanent sextupole magnet, the field strength presents a radial quadratical dependence [Hal80]:

$$B(r) = B_{\rho t}\Big(\frac{r}{r_{\rho t}}\Big)^2 \tag{1.62}$$

with the radius $r = \sqrt{x^2 + y^2}$ and $B_{\rho t}$ given by

$$B_{\rho t} = \frac{3}{2}\frac{J \cdot \sin(4\pi\varepsilon/M)}{4\pi\varepsilon/M}\Big(1 - \frac{r_{\rho t}^2}{r_o}\Big) \tag{1.63}$$

being J the magnetization of the sextupole material, M the number of segments, r_o the outer and $r_{\rho t}$ the inner radius of the magnet, while the *filling factor* ε describes the relative amount of magnetized material in the magnet ($0 < \varepsilon < 1$).

Hydrogen	Deuterium
$\mu_1^H = \frac{1}{2} g_s \mu_B$	$\mu_1^D = \frac{1}{2} g_s \mu_B$
$\mu_2^H = \frac{1}{2} g_s \mu_B \cos(2\theta)$	$\mu_2^D = \frac{1}{2} g_s \mu_B \cos(2\theta+)$
$\mu_3^H = -\frac{1}{2} g_s \mu_B$	$\mu_3^D = \frac{1}{2} g_s \mu_B \cos(2\theta-)$
$\mu_4^H = -\frac{1}{2} g_s \mu_B \cos(2\theta)$	$\mu_4^D = -\frac{1}{2} g_s \mu_B$
	$\mu_5^D = -\frac{1}{2} g_s \mu_B \cos(2\theta-)$
	$\mu_6^D = -\frac{1}{2} g_s \mu_B \cos(2\theta+)$

Table 1.2:
Magnetic moments of hydrogen and deuterium hyperfine states. During the calculation, the eigenenergies (1.14) and (1.28) have been approximated by setting $\varepsilon_H \simeq \varepsilon_D \simeq 0$.

Thus, the equations of motion can be written as

$$m\,\ddot{x} = -\mu_{|\,a\,\rangle}\frac{2B_{\rho t}}{r_{\rho t}^2}x \tag{1.64}$$

$$m\,\ddot{y} = -\mu_{|\,a\,\rangle}\frac{2B_{\rho t}}{r_{\rho t}^2}y \tag{1.65}$$

$$m\,\ddot{z} = 0 \tag{1.66}$$

where $\mu_{|\,a\,\rangle}$ is the magnetic moment of the atom in hyperfine state $|\,a\,\rangle$ defined by:

$$\mu_{|\,a\,\rangle} = \frac{dE_{|\,a\,\rangle}}{dB} = \frac{dE_{|\,a\,\rangle}}{dx}\frac{1}{B_C} \tag{1.67}$$

and shown in table 1.2 for hydrogen and deuterium cases.
Hence, atoms with positive magnetic moment ($m_s = \frac{1}{2}$) are focused toward the axis of the magnet, while atoms with negative magnetic moments ($m_s = -\frac{1}{2}$) are defocused toward the pole tips. Moreover, as the magnetic moments of mixed hyperfine states is field dependent, the intensity the Stern-Gerlach force differs for each state. This difference can be made very small in a high field regime, where the magnetic moments of the mixed states can be approximated to the ones of the correspondent pure state.

Chapter 2

The Experimental Setup

The HERMES hydrogen/deuterium polarized target has been running since 1996. An Atomic Beam Source (ABS) produces a polarized jet of atomic hydrogen or deuterium and focuses it into a storage cell, a windowless elliptical tube through which the HERA electron or positron beam passes. A sample of gas (ca. 5%) diffuses from the middle of the cell into a Breit Rabi Polarimeter (BRP), which measures the atomic polarization, and a Target Gas Analizer (TGA), which measures the atomic and molecular relative contents. A magnet sorrounding the storage cell provides an holding field defining the polarization axis and preventing spin relaxation by effectively decoupling the magnetic moments of electrons and nucleons. A schematic view of the whole target setup is given in figure 2.1

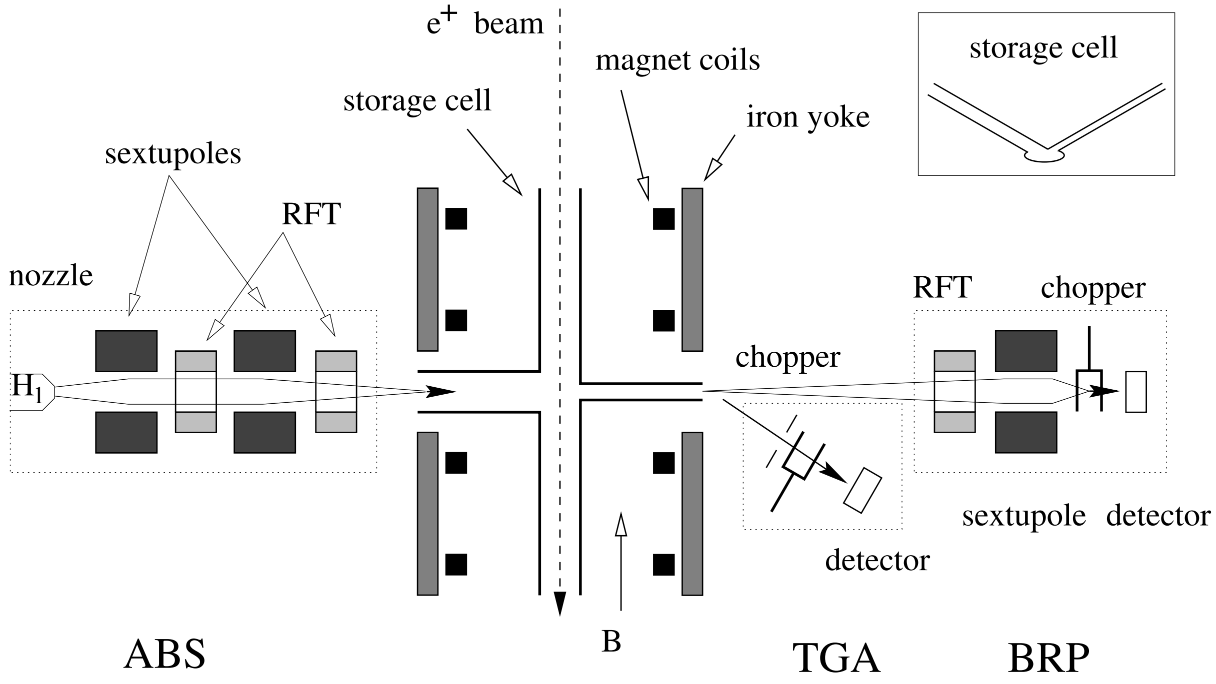

Figure 2.1: A schematic view of the HERMES polarized target. All components are described in the text.

The HERMES target has supplied longitudinally polarized hydrogen/deuterium nuclei till the end of 2000. During the HERA shutdown in 2001, a considerable effort has been made in order to provide the HERMES experiment with a transversely polarized target. This goal has been achieved by conceiving a new magnet whose design is detailed described along the chapter.

2.1 The Atomic Beam Source

In the HERMES ABS [Nas02] atomic hydrogen (or deuterium), produced by means of a radio-frequency dissociator, flows through an aluminum nozzle, a skimmer and a collimator, gets into a sextupolar magnetic system, which focuses an electron polarized beam, and then into high frequency transition units, which transfer the polarization to the nuclei. The polarized beam is then injected into the storage cell through a side tube (injection tube). A powerful differential pumping system with a total nominal pumping speed of over 15000 l/s ensures low attenuation of the beam caused by residual gas. The HERMES ABS is capable of a throughput of $6.6 \cdot 10^{16}$ atoms/s for hydrogen (two hyperfine states injected) and $5.0 \cdot 10^{16}$ atoms/s for deuterium (three states). The injected nuclear polarization is above 97 % for hydrogen and above 91 % for deuterium. A simplified scheme of the ABS setup is shown in figure 2.2.
The radio-frequency dissociator[7] operates at a frequency of 13.56 MHz with a nominal power of 300 W. The discharge takes place inside a glass tube where 1 mbar·l/s of hydro-

[7]During the 2000 running period, the radio-frequency dissociator has been replaced with a microwave running at a frequency of 2.45 GHz and a power of 600 W [Koc98].

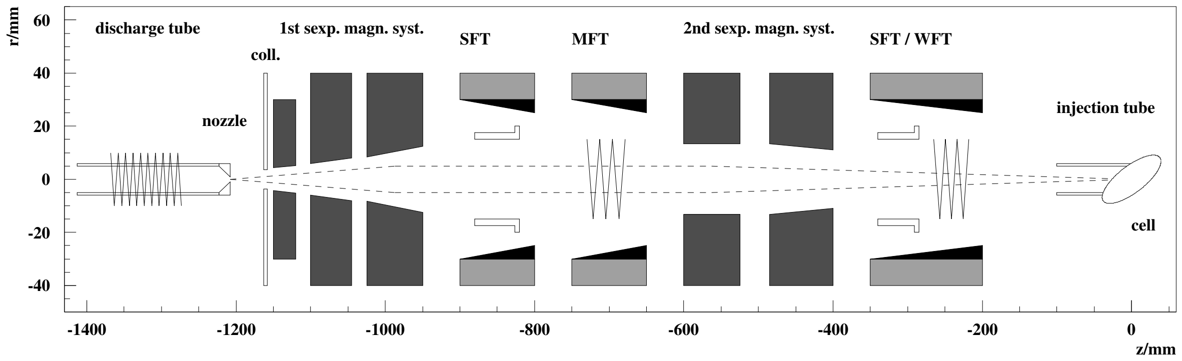

Figure 2.2: Schematic view of the HERMES ABS. The dark gray elements represent the sextupolar magnets, while the light gray ones are the transition units. The SFTs (Strong Field Transitions) have to be replaced, while the MFT and WFT (Medium and Weak Field Transitions have to be re-tuned, when switching between hydrogen and deuterium.

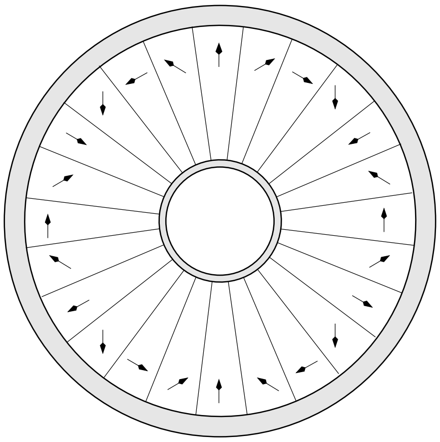

Figure 2.3:
Schematic cross section view of a permanent sextupole magnet. The magnet consists of 24 segments of *Vacodym* with varying magnetization direction. To prevent chemical destruction by atomic hydrogen, the magnets are enclosed in vacuum tight stainless steal cans.

gen flows along with a small amount of oxygen[8]. The combination of the two gases leads to the formation of an ice coating on the nozzle surface, constantly kept at 100 K during normal operation. In order to prevent blocking, the nozzle is periodically warmed up to room temperature with a typical cycle between four and seven days for hydrogen. The degree of dissociation measured out of the dissociator is about 80 %.

The sextupolar magnetic system is composed by five radially segmented high gradient permanent magnets (fig. 2.3) with pole tip fields up to 1.5 T. According to the Stern-Gerlach separation explained in section 1.4, the sextupole magnets focus atoms with $m_s = +\frac{1}{2}$ and deflect atoms with $m_s = -\frac{1}{2}$ away from the atomic beam axis. The magnets are grouped in two subsystems and tapered in order to maximize the acceptance of the diverging beam. The first subsystem, split in three magnets, is designed in order to minimize the attenuation due to residual gas pressure caused by the deflected atoms.

Four adiabatic hyperfine transition units are used to interchange the atomic states populations[9]. The strong field transition (SFT) units consist of a resonator cavity, while

[8] The oxygen improves the discharge performance.

[9] An explanation of the high frequency transition nomenclature and working principle is given in the first chapter

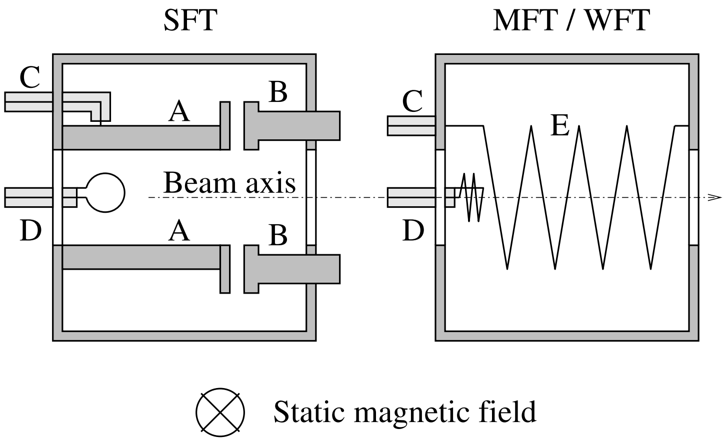

Figure 2.4:
Schematic view of the SFT resonator and the MFT/WFT coil system. The different components are the resonator rods (A), the adjustable capacitor (B), the coaxial RF power input (C), the pick-up loop (D) and the RF coil (E).

the weak or medium field ones (WFT/MFT) employ a high frequency coil (fig. 2.4). All HF-transitions are immersed in a static magnetic field whose strength and gradient along the atomic beam path can be individually adjusted. Two units (a SFT and a WFT) are placed in the so called ABS-appendix, just before the injection tube, while the other two (a SFT and a WFT/MFT) are located between the sextuple subsystems. In the deuterium case all units are needed to supply positive and negative nuclear polarization, whereas for hydrogen only the appendix ones are requested for this purpose. Thanks to

Gas	HFT (betw. 6-poles)	HFT (appendix)	Inj. States	P_e	P_z	P_{zz}	Use
	-	-	$\vert 1\rangle, \vert 2\rangle$	+1	0	-	Cal
H	-	WFT 1-3	$\vert 2\rangle, \vert 3\rangle$	0	-1	-	Data
	-	SFT 2-4	$\vert 1\rangle, \vert 4\rangle$	0	+1	-	Data
	SFT 2-4 / MFT 2-3	-	$\vert 1\rangle$	+1	+1	-	Cal
	WFT 1-3 / MFT 1-3	-	$\vert 2\rangle$	+1	-1	-	Cal
	SFT 2-4 / MFT 2-3	WFT 1-3	$\vert 3\rangle$	-1	-1	-	Cal
	WFT 1-3 / MFT 1-3	SFT 2-4	$\vert 4\rangle$	-1	+1	-	Cal
	WFT 1-3, SFT 2-4	-	none	-	-	-	Cal
	-	-	$\vert 1\rangle \vert 2\rangle \vert 3\rangle$	+1	0	0	Cal
D	SFT 2-5	WFT 1-4	$\vert 3\rangle \vert 4\rangle$	0	-1	+1	Data
	SFT 3-5	SFT 2-6	$\vert 1\rangle \vert 6\rangle$	0	+1	+1	Data
	MFT 1-4	SFT 3-5	$\vert 2\rangle \vert 5\rangle$	0	0	-2	Data
	MFT 1-4	SFT 2-6	$\vert 3\rangle \vert 6\rangle$	0	0	+1	Data
	MFT 3-4, SFT 2-6	-	$\vert 1\rangle$	+1	+1	+1	Cal
	WFT 1-4, SFT 2-6	-	$\vert 2\rangle$	+1	0	-2	Cal
	WFT 1-4, SFT 3-5	-	$\vert 3\rangle$	+1	-1	+1	Cal
	MFT 3-4, SFT 2-6	WFT 1-4	$\vert 4\rangle$	-1	-1	+1	Cal
	WFT 1-4, SFT 3-5	SFT 3-5	$\vert 5\rangle$	+1	0	-2	Cal
	WFT 1-4, SFT 2-6	SFT 2-6	$\vert 6\rangle$	-1	+1	+1	Cal

Table 2.1: Injection modes of the atomic beam source. The table shows the high frequency transition units employed (2^{nd} and 3^{rd} column), the injected hyperfine states and the resulting electron (P_e), nuclear (P_z) and tensor (P_{zz}) polarizations in the ideal case of unitary efficiencies of sextupole system and transition units and no depolarization inside the target cell. The last column clarifies the purpose of each mode (Cal: calibration, monitoring; Data: HERMES data taking). For some injection mode (i.e. the hydrogen no state and some deuterium single states [Bau00]) The MFT between the sextupoles has to be tuned as a WFT 1-4. The no state injection mode is possible only for the hydrogen case and it is operational since April 2002.

the installed transition units, nearly all combinations of hyperfine states can be injected into the storage cell. The most relevant injection modes for hydrogen and deuterium are shown in table 2.1.

In the most general case, the description of the history of an atom through the ABS has to take into account the possibility that all transition units are used. This means that the atom is affected by the first sextupole subsystem, then by the transition units located between the magnets, by the second sextupole subsystem and finally by the transitions in the appendix. The transmissions probabilities of the sextupole system can be described in the hydrogen (deuterium) case by a 4x4 (6x6) matrix whose elements σ_{ab} represent the transmission probability of an atom which enter the first subsystem in state $|\, a\,\rangle$ and the second in state $|\, b\,\rangle$. If all transitions between the sextupoles are represented by the matrix $B = \prod_i T^{(i)}$ and all transitions in the appendix by $A = \prod_j T^{(j)}$ [10], then the relative population of atoms injected into the storage cell in state $|\, a\,\rangle$ is given by

$$n_a = \sum_c A_{ac} \sum_b \sigma_{bc} B_{bc} \tag{2.1}$$

If the transition units between the sextupole magnets are not used, the transmission probabilities of the sextupole system can be described by vectors instead of matrices and the equation the 2.1 becomes:

$$n_a = \sum_b A_{ab} \sigma_{bb} \tag{2.2}$$

In the most simple case that even the appendix transitions are off, one has:

$$n_a = \sigma_{aa} \tag{2.3}$$

[10] The meaning of the T matrices is explained in section 1.2.4

State	$\|1\rangle$	$\|2\rangle$	$\|3\rangle$	$\|4\rangle$
$\|1\rangle$	0.45	0.45	0.033	0.047
$\|2\rangle$	0.45	0.45	0.03	0.043
$\|3\rangle$	0.009	0.0085	0	0
$\|4\rangle$	0.013	0.013	0	0

State	$\uparrow$	$\downarrow$
$\uparrow$	0.45	0.035
$\downarrow$	0.009	0.0

Table 2.2: Absolute transmission probabilities σ_{ab} of the ABS sextupole system calculated by a tracking program for hydrogen (left table) and deuterium (right table) at the working point of the ABS. The number of the row refers to the hyperfine state in the first subsystem and the number of the column to the state in the second subsystem. Due to the low critical field $B_C^D = 11.7\,mT$ of Deuterium, the transmissions probabilities depend only on the value of m_S. $\sigma_{\uparrow\downarrow}$ is the transmission probability for an atom, which is in state $m_S = \frac{1}{2}$ in the first sextupole subsystem and in state $m_S = -\frac{1}{2}$ in the second.

Estimations of the matrix elements σ_{ab} have been provided by Braun and Baumgarten [Bra95, Bau00] using a montecarlo simulation and are shown in table 2.2.

2.2 The unpolarized gas feed system

In addiction to the ABS, the HERMES target is furnished with an unpolarized gas feed system (UGFS). The UGFS can inject a constant gas flow either into the cell, through a small capillary (see fig. 2.5), or directly into the target chamber. The flow is kept stable either by a flow regulator or by a feedback controlled thermovalve and can be measured with a 2 % accuracy. The UGFS is used for target unpolarized data taking as well as for target related measurement such as the *rest gas calibration* explained in section 3.2.1.

2.3 The storage cell

The target storage cell (fig. 2.5) consists of an elliptical cross section beam tube 400 mm long made from 75 micron thick aluminum and electrically connected to the HERA electron beam pipe. The polarized atomic hydrogen is injected through a 100 mm long 10 mm diameter tube and flows out of the cell through its open ends into the scattering vacuum chamber and through a 100 mm long 5 mm diameter sample tube (elongated by a 10 mm diameter extension tube) toward the diagnostic devices. Both injection and sample tubes are mounted at an angle of 30° with respect to the horizontal plane. The target cell is enclosed in a scattering chamber (fig. 2.6) kept under ultra high vacuum by two molecular turbo pumps with a total pumping speed of 4400 l/s.
The use of a storage cell results in an increase of the target density of about two orders of magnitude compared to a free jet target. Moreover, since December 1999, a further raise

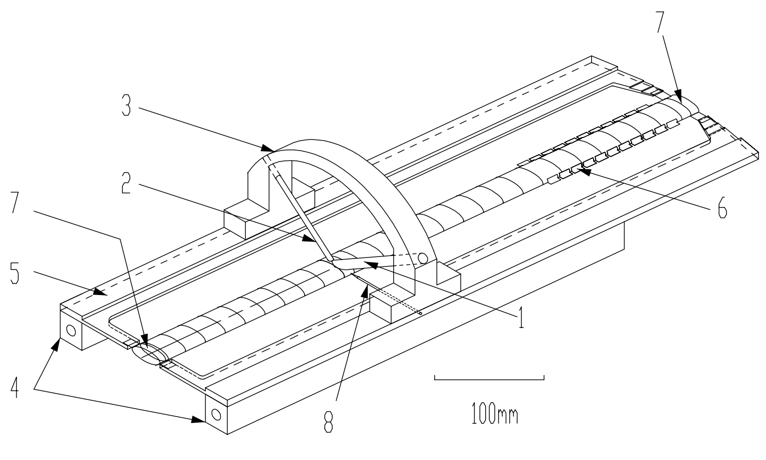

Figure 2.5:
The HERMES target cell. The different components are: 1) H/D injection tube; 2) Sample tube; 3) Support arch; 4) Cryogenic-cooling and support rails; 5) Support plates; 6) Cell extension with pumping apertures; 7) Cell end support collars; 8) Unpolarized gas feed capillary.

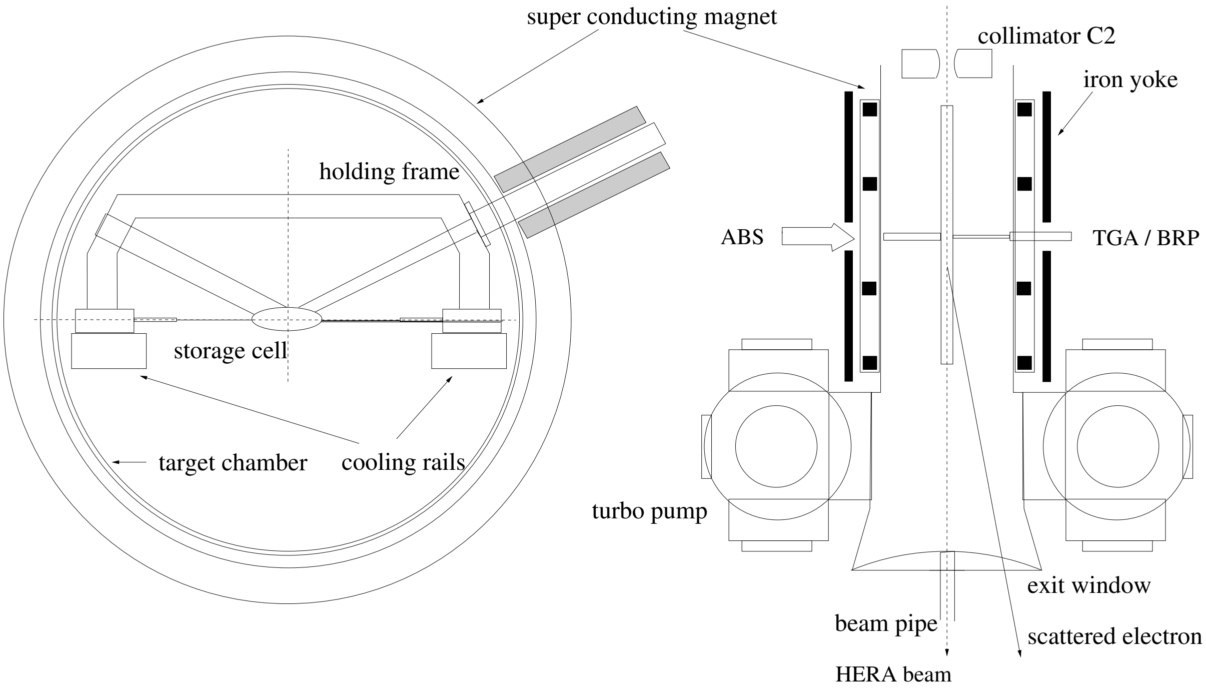

Figure 2.6: Schematic views of the longitudinal target chamber and the superconducting magnet along the HERA beam direction (left) and from the top (right).

of the density by a factor 1.6 was obtained by reducing the cell cross section from 29 x 9.8 mm (*bigger cell*) to 21 x 8.9 mm (*smaller cell*).

Wall collisions can cause atomic depolarization and recombination [Bau00, Bau02d]. In order to inhibit as much as possible these effects, the HERMES cell is coated with Drifilm. During HERA beam operation, this coating can be partially spoiled by synchrotron radiation. As a small amount of oxygen is coming from the dissociator, an additional water coating gradually covers the cell wall. This ice coverage has been found to compensate for the loss of the Drifilm surface.

A gaseous helium cooling system mounted on the cell support structure, in combination with a heater resistor placed inside the helium line, can lower the cell temperature down to about 35 K and keep it constant[11]. This is important to increase the target thickness, which rises as $1/\sqrt{T}$, and, at the same time, to optimize the target performance by setting temperature values where atoms are less sensitive to the depolarization and recombination mechanisms. Those values have been found to be 100 K for hydrogen and 60 K for deuterium. At those temperatures, areal densities of $7.6 \cdot 10^{13}$ nucleons/cm^2 for hydrogen and $2.1 \cdot 10^{14}$ nucleons/cm^2 for deuterium have been achieved.

The HERMES storage cell is currently manufactured at the Physics Department Workshop of the University of Ferrara.

[11]The cell temperature is monitored by means of two platinum resistors.

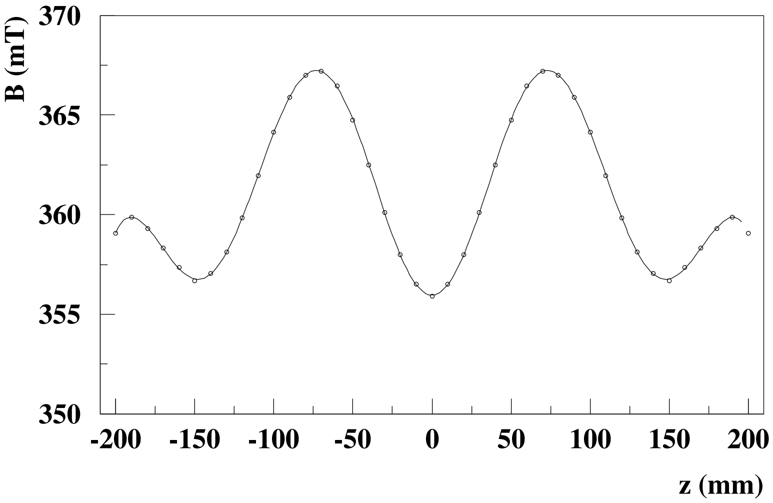

Figure 2.7:
Field strength of the longitudinal target magnet measured along the HERA beam direction z overall the storage cell length.

2.4 The Longitudinal Target Magnet

The HERMES storage cell is immersed in a static high magnetic field which provides the target spin direction and, at the same time, ensures high polarization of the mixed hyperfine states by effectively decoupling the electrons and nucleons magnetic moments. From 1996 till the end of 2000, the HERMES hydrogen/deuterium target was longitudinally polarized with respect to the electron beam axis. The employed magnet was a superconducting solenoid consisting of four coils surrounding the scattering vacuum chamber (fig. 2.6). The nominal provided axial field strength was 335 mT, while the overall uniformity of ±3% (fig. 2.7) was required in order to avoid possible beam induced resonant depolarization in the storage cell, as explained in section 2.5.

2.5 The Transverse Target Magnet

In 1999 the HERMES collaboration decided to run with a transversely polarized hydrogen (and optionally deuterium) target, starting from 2001. For that purpose, a completely new target magnet had to be designed taking into account severe problems related to the interaction of the generated vertical field with the HERA e-beam. The magnet was successfully installed in the HERMES target setup in July 2001 during the one year long HERA luminosity upgrade shutdown.
As already mentioned in the previous section, the target magnet has two purposes: to determine the orientation of the target spin and to effectively decouple the magnetic moments of electrons and nucleons. This latter feature is of fundamental importance in order to achieve a high injected polarization and to preserve it from spin relaxation processes. Indeed, in the HERMES storage cell one can distinguish between different depolarization mechanisms (see section 3.3.1): wall depolarization, taking place when an atom hits the cell wall, spin exchange, occurring when two atoms collide in the gas

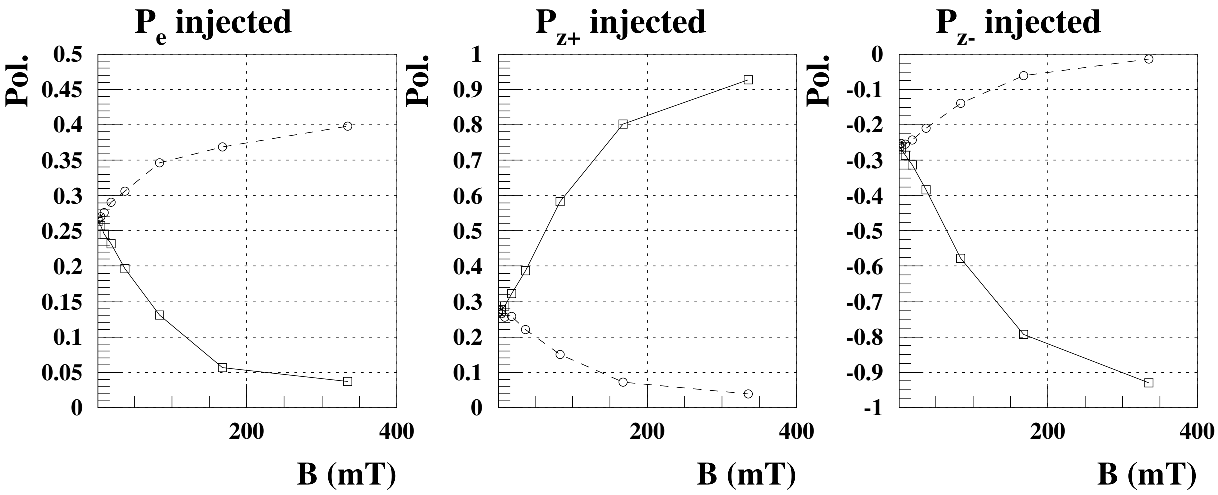

Figure 2.8: The polarization of the atoms sampled by the Breit-Rabi Polarimeter plotted as function of the holding field in case of hydrogen. The open circles (squares) represent the electron (proton) polarization. The three graphs show different ABS injection modes: electron, nuclear positive and nuclear negative polarizations (from left to right).

phase, and bunch field induced resonant depolarization, originating when the frequency of a harmonic induced by the HERA e-beam matches the frequency difference between two different hyperfine states present in the cell. The first two processes can be prevented or at least limited by applying an adequately strong magnetic field, whereas a high field uniformity is required in order to avoid the third one. On the other hand, in the transverse target magnet case serious constraints on the maximum applicable field originate from the bending of the HERA electron beam passing through the vertical field and the consequent emission of synchrotron light toward the HERMES spectrometer.

2.5.1 The magnet design

The lower limit for the field intensity has been derived from the experience accumulated with the longitudinal target: in case of hydrogen[12], in order to maintain the atomic polarization above 85 % and the total polarization relative uncertainty below 4.5 %, a field strength of around 300 mT is highly desirable (fig. 2.8).

The problem of the upper applicable field strength has been carefully studied. A particle with electric charge e moving in a static uniform magnetic field perpendicular to the particle trajectory undergoes a circular uniform motion with radius of curvature ρ given by [Cer94]

$$\frac{1}{\rho}\,[\mathrm{m}^{-1}] = \frac{eB}{p} = 0.2998\frac{B\,[\mathrm{T}]}{p\,[\mathrm{GeV/c}]} \tag{2.4}$$

[12]Because of the five time less critical field, the deuterium case is less critical in that respect (see chapter 1).

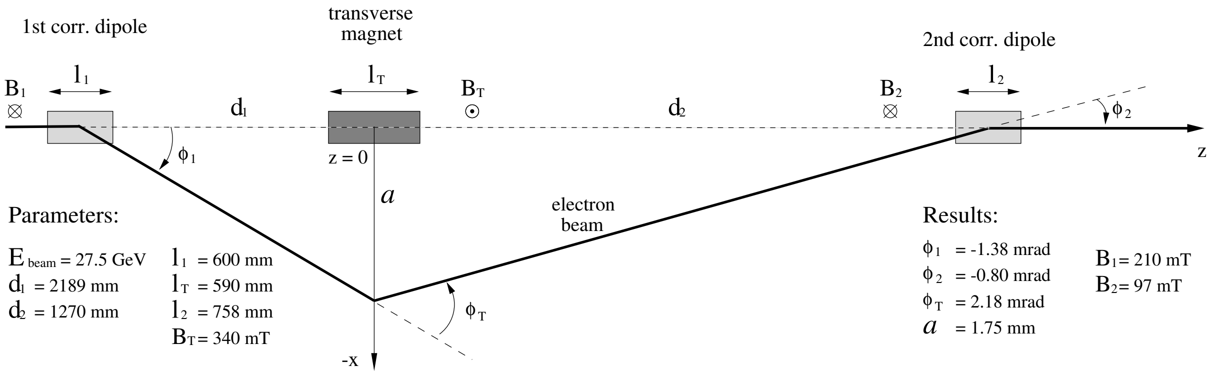

Figure 2.9: Scheme of the compensation of the HERA beam trajectory through the HERMES transverse polarized target (top view). The bending angels and the total beam displacement a have been calculated for a target field of 340 mT.

where B is the field strength and p is the particle's momentum.
Hence, for the bending angle Φ one finds:

$$|\phi| = \frac{0.2998}{p} \int B(z)dz \tag{2.5}$$

where the integration is performed along the particle's direction z.
In order to compensate for this deflection, two correction magnets, already existing upstream and downstream of the target at a distance of $z = -1270\,\mathrm{mm}$ and $z = 2189\,\mathrm{mm}$ respectively, could be used. The maximum target field strength the can be counterbalanced in this way results to be $B = 340\,\mathrm{mT}$, which corresponds, at the nominal beam momentum of 27.5 GeV/c, to a total bending angle $\Phi = 2.2\,\mathrm{mrad}$ and a beam displacement inside the storage cell $d = 1.75\,\mathrm{mm}$, as shown in figure 2.9.
The *synchrotron radiation* [Eld47] released by a deflecting charge particle is emitted tangentially to the motion of the particle itself and, therefore, within and angle Φ which equals the beam bending angle. As shown in figure 2.10, at $B = 340\,\mathrm{mT}$ the emitted synchrotron light does not enter inside the acceptance of the HERMES spectrometer, hitting the HERA beam pipe far beyond the last detector.
The emitted power for single particle is given by

$$P = \frac{2}{3}\frac{e^2 c}{4\pi\epsilon_0}\frac{\beta^4\gamma^4}{\rho^2} \tag{2.6}$$

where ε_0 is the vacuum dielectric constant, c is the speed of light, $\beta = v/c$ and $\gamma = m/m_0$ is ratio between the lab- and rest-frame particle mass.
For a beam current of 45 mA (close to the highest value that the HERA storage ring can reach) a total emitted power around 5 kW has been estimated, a value absolutely compatible with the accelerator design.

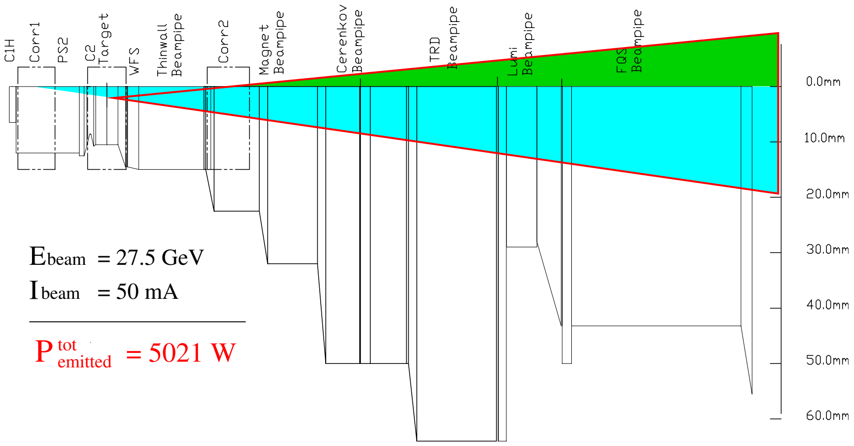

Figure 2.10: The synchrotron radiation cone emitted by the HERA electron beam through the transverse target setup (for $B = 340\,\mathrm{mT}$) compared to the right-half beam pipe profile. The total emitted power has been computed for a beam current of 50 mA.

The most critical requirement for the transverse field comes from the study of the possible beam induced depolarization. As shown in section 1.3, when the frequency difference between a pair of hyperfine states matches the frequency of one of the beam harmonics, resonant depolarization occurs with a probability proportional to the square of the beam current. In order to determine for which values of the target field this mechanism can take place, one has to study the harmonic structure of the time dependent magnetic field induced by the 220 bunches of the electron beam.

Depending on which pair of hyperfine states is involved, transitions are distinguished between π, occurring when the rf-field component is perpendicular to the static one, and σ, taking place when the two fields are parallel. Around the working point of the target magnet (300 to 340 mT), the π resonances are easily avoidable with a field uniformity of the percent level[13]. This is unfortunately not the case for the σ, whose spacing is only 0.37 mT.

Taking into account the theoretical width of the σ resonances, the requirement for the target field uniformity has been fixed to the conservative value of $\Delta B = 0.14\,\mathrm{mT}$.

Due to geometrical constraints imposed by the HERMES setup, the design of a magnet which would meet all the listed requirements was not possible. After the construction, the field uniformity has been improved by shimming the magnet pole tips with very thin iron bars. At a field intensity of $B = 297\,\mathrm{mT}$, values of $\Delta B_z = 0.05\,\mathrm{mT}$, $\Delta B_y = 0.15\,\mathrm{mT}$, $\Delta B_x = 0.60\,\mathrm{mT}$ have been achieved [Reg02], all measured overall the storage cell dimensions, where z is the longitudinal direction, while y and x are the two transverse ones (fig. 2.11). The magnet has been installed into the HERMES target and the whole experimental setup has been arranged in order to produce and measure polarized hydrogen. Due to the poor performance of the HERA machine after the startup in September 2001, a serious

[13] The exception of the electronic and nuclear deuterium transition $\pi\,|3\rangle \leftrightarrow |6\rangle$ can be neglected because its probability is strongly suppressed, as shown in figure 1.13.

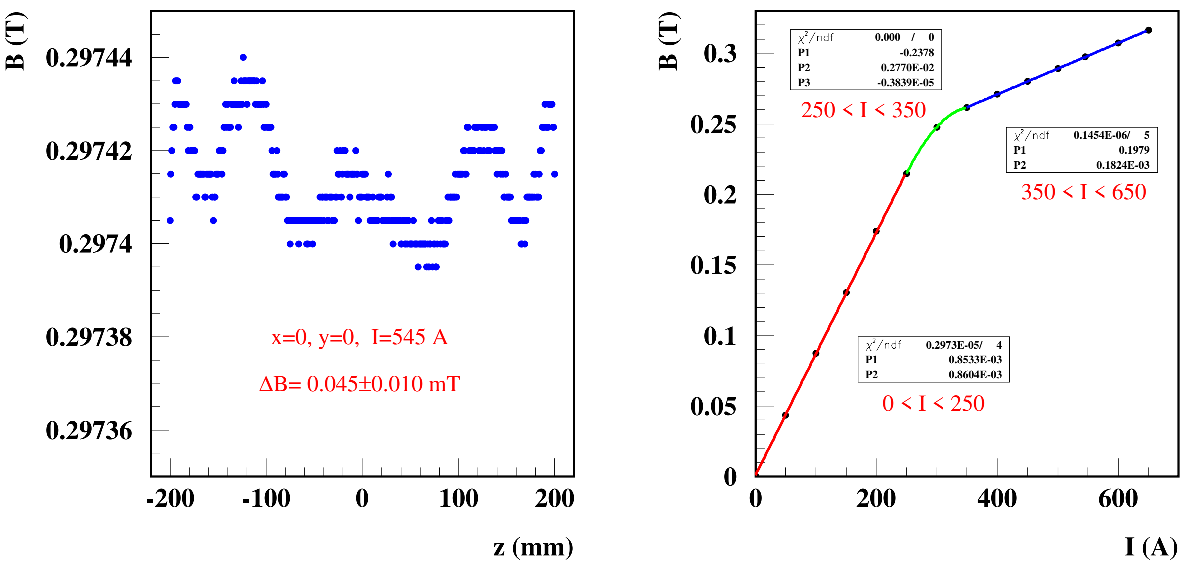

Figure 2.11: The left plot shows the transverse magnet field uniformity measured along the magnetic axis at the nominal field strength $B = 297\,\mathrm{mT}$. Along the other directions, uniformities of $\Delta B_y = 0.15\,\mathrm{mT}$ and $\Delta B_x = 0.60\,\mathrm{mT}$ have been measured. On the right, the relation between applied current and generated field, measured in the center of the magnet, is shown. The two distinguishable regions of proportionality are an effect of the two different kinds of iron used for the pole tip design.

study of the effect of the field non-uniformity along x has not been possible up to now. Nevertheless, some preliminary measurements have been taken whose results are shown in section 3.3.1. The potential improvement of the field uniformity is still under study and a feasible solution making use of two correction coils embedded inside the storage cell support structure is currently under test.

2.6 The Target Gas Analyzer

The target gas analyzer (TGA) [Bau02f] measures the atomic and the molecular contents of the gas coming from the storage cell through the sample and extension tubes. The TGA setup, shown in figure 2.12, consists of a pair of baffles, a chopper, a 90° off-axis quadrupole mass spectrometer (QMS) with a cross beam ionizer and a channel electron multiplier (CEM) for single ion detection. The TGA shares the same vacuum system of the BRP sextupole chamber (as shown in figure 2.16), composed by two cryo pumps and a titanium sublimation pump, with a total pumping speed of about 7000 l/s. During operation, the pressure is about $3.5{\cdot}10^{-9}$ mbar. The TGA vacuum chamber is backed out

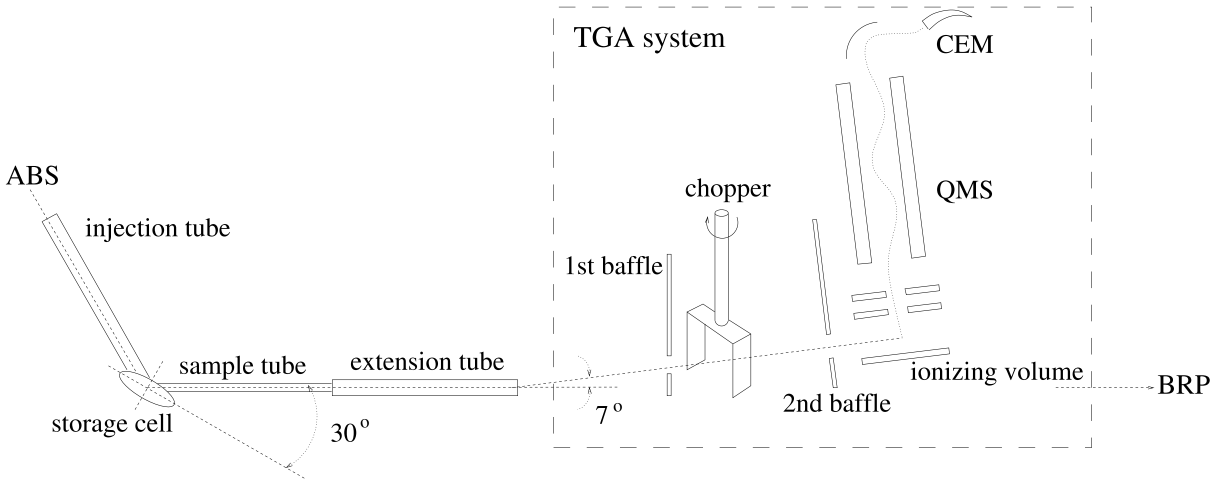

Figure 2.12: Schematic view of the TGA. The gas of atoms and molecules diffuses through the extension tube and the two baffles toward the ionizing volume. The chopper is used for background subtraction.

with temperatures up to 180 °C.
The TGA is mounted 7° off-axis with respect to the BRP, in order not to interfere with the beam entering the polarimeter. The first baffle ensures that only gas from the sample beam can reach the detector, while the second one acts as a collimator, so that no atoms can hit the ionizing volume walls and recombine. The chopper, placed between the two baffles, rotates at 5.5 Hz periodically shutting the sample beam in order to allow the residual gas measurement. Particles entering the detector are first ionized by 70 eV electrons, than mass filtered by the QMS and finally detected by the CEM. The generated pulses are electronically treated and counted by a 2048 bins time resolving counter (TRC). The bin length is typically set to 175 μs so that two chopper turns are collected within the whole bin range as shown in figure 2.13. The synchronization between the chopper status and the counting rate is given by a trigger signal coming from the chopper electronics.

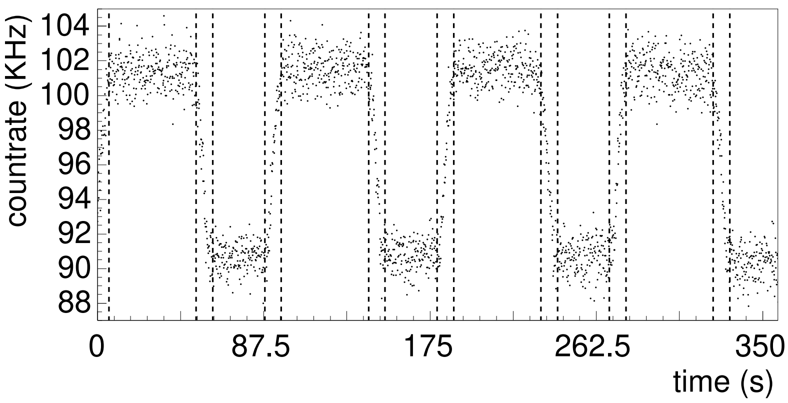

Figure 2.13:
Time spectrum of atomic countrates in the TGA. The vertical lines indicate the bin numbers corresponding to the limits between the chopper positions open, undefined and closed.

The beam rate is calculated by the difference between chopper open and closed measured signals.

2.6.1 Interpretation of the TGA signals

The measured TGA atomic (molecular) signal S_a (S_m) is proportional to the particle flux Φ_a (Φ_m) into the TGA, the ionization cross section σ_a^{ion} (σ_m^{ion}), the detection probability ϵ_a (ϵ_m) and the mean inverse velocity of the particles $\left\langle\frac{1}{v_a}\right\rangle$ ($\left\langle\frac{1}{v_m}\right\rangle$). The further dependence of the signal on the emission current is measured and taken into account by the normalization function $f(I_{emiss})$. Taking all parameters into account one fins[14]

$$S_{a,m} \propto f(I_{emiss})\ \sigma_{a,m}^{ion}\ \epsilon_{a,m} \left\langle \frac{1}{v_{a,m}} \right\rangle \Phi_{a,m} \tag{2.7}$$

The total effective flux of hydrogen (or deuterium) atoms into the TGA is given by:

$$\Phi^{TGA} = \Phi_a + 2\Phi_m \tag{2.8}$$

For thermalized atoms and molecules one has:

$$\left\langle \frac{1}{v_m} \right\rangle = \sqrt{2} \left\langle \frac{1}{v_a} \right\rangle \tag{2.9}$$

From (2.7), (2.8) and (2.9) the total TGA signal $S_{tot} \propto \Phi^{TGA}$ can be derived:

$$S_{tot} = S_a + \sqrt{2}\,\kappa\ S_m \tag{2.10}$$

where κ gives the relative sensitivity of the TGA for atoms and molecules:

$$\kappa = \frac{\sigma_a^{ion}\ \epsilon_a}{\sigma_m^{ion}\ \epsilon_m} \tag{2.11}$$

The TGA geometrical acceptance is so that the detectable particles have to bounce, on average, more than 100 times onto the extension tube (ET) inner surface [Bau00]. For this reason, particles entering the TGA detector have thermalized with the ET tube wall. The temperature dependence of the TGA signal is then given by the function $g(T_{ext}) = 1/\sqrt{T_{ext}}$, where T_{ext} is the measured ET temperature[15].

One can now define the temperature and emission current normalized nucleon flowrates $\phi_{a,m}$ as

$$\phi_a = \frac{S_a}{g(T_{ext})\ f(I_{emiss})} \tag{2.12}$$

[14]The influence of external magnetic fringe fields of target and spectrometer magnets can be neglected as both magnets are always kept on during data taking and target calibrations.

[15]A thermocouple on the extension tube was first installed at the beginning of 1999. In the 1997 analysis, the extension tube temperature has been derived using the expression $T_{ext}(T) = T_0 + \frac{300-T_0}{300}T$, where T_0 is a constant and T is the measured cell temperature in K [Kol98].

$$\phi_m = \frac{\sqrt{2}\,\kappa\; S_m}{g(T_{ext})\; f(I_{emiss})} \tag{2.13}$$

The total normalized flowrate is proportional to the injected ABS intensity Φ^{ABS}

$$\phi_{tot} = \phi_a + \phi_m \propto \Phi^{ABS} \tag{2.14}$$

and is therefore a good indicator of the ABS stability.
The degree of dissociation of the sample beam, defined as the fraction of nucleons in atoms relative to all nucleons of particles entering the TGA, is given by

$$\alpha^{TGA} = \frac{\phi_a}{\phi_a + \phi_m} = \frac{S_a}{S_a + \sqrt{2}\,\kappa\; S_m} \tag{2.15}$$

The degree of dissociation α^{TGA}, also called atomic fraction, is constantly monitored by the TGA at measurement rate of roughly once per minute.

2.6.2 The calibration of the TGA

The purpose of the TGA calibration [Bru01] is to determine the relative sensitivity κ defined by (2.11). The calibration can be performed by varying the relative amount of atoms and molecules at a constant injected ABS total flux:

$$\phi_{tot} = \phi_a + \phi_m = const \tag{2.16}$$

Using the definitions (2.12) and (2.13), one can write

$$\frac{\partial\left(\frac{S_m}{g(T_{ext})\; f(I_{emiss})}\right)}{\partial\left(\frac{S_a}{g(T_{ext})\; f(I_{emiss})}\right)} = -\frac{1}{\sqrt{2}\,\kappa} \tag{2.17}$$

so that a fit over the corrected molecular signal as function of the corrected atomic one results in a straight line with a slope of $-\frac{1}{\sqrt{2}\,\kappa}$.
As in the HERMES target the recombination process is strongly temperature dependent, a variation of the atomic fraction can be obtained in a controllable way by changing the temperature of the storage cell. A second possibility is to take advantage of an accidental beam loss in the region of the HERMES target which might temporary change the surface property of the cell and cause a sharp drop of α^{TGA}. This beam loss calibration method does not require any knowledge about the temperature correction function $g(T_{ext})$.

Temperature scans

The storage cell temperature can be changed by varying the helium flowrate through its rails (see section 2.3). After having reached a stable temperature value, the TGA is let

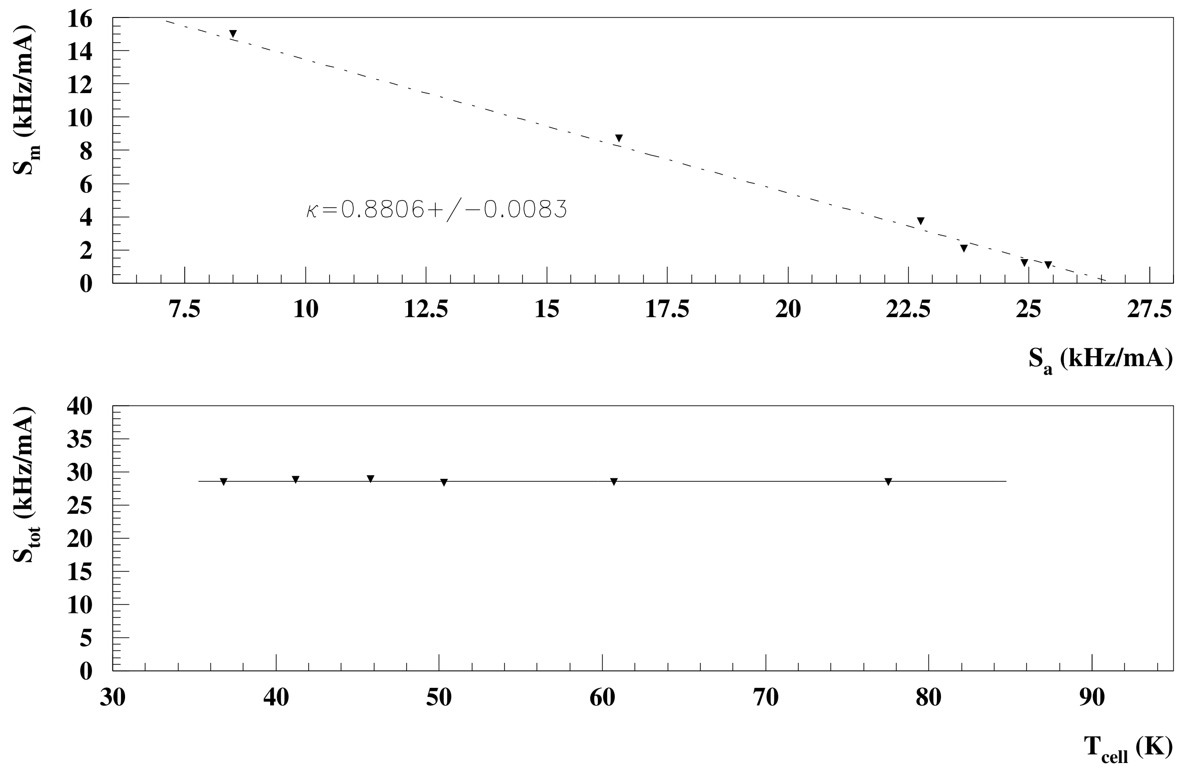

Figure 2.14: Analysis of the data from a temperature scan. The upper plot shows the fit to the corrected molecular rate as function of the corrected atomic one. Each point results from the average over the data collected during one temperature step. The lower plot shows the total normalized nucleon flowrate (see equation (2.14) and (2.16)) versus the cell temperature, proving the validity of the calibration.

measure over a period of time of 30 minutes to one hour in order to collect enough statistics. A significant variation of α^{TGA} is usually possible by changing the cell temperature between 30 and 100 K.

An example of cell temperature scan performed using the polarized deuterium target is shown in figure 2.14. The plotted rates are corrected for $g(T)$ and $f(I_{emiss})$. During the same analysis, the calibration result has been cross checked by looking at the consistency of equation (2.16) for different cell temperatures.

The several cell temperature scans performed between 1997 and 2000 have provided the following average results:

$$\kappa = 0.551 \pm 0.026 \qquad \text{(Hydrogen)} \tag{2.18}$$

$$\kappa = 0.861 \pm 0.024 \qquad \text{(Deuterium)} \tag{2.19}$$

The discrepancy between the two values can be interpreted as consequence of the different masses involved (resulting in different ionization and detection efficiencies) and of the ionoptic voltages tuning.

HERA beam losses

A beam loss close to the HERMES target causes a sudden and sharp drop of α^{TGA} without varying the cell temperature. The change in the atomic fraction is related to the sublimation of the ice coating and to a possible damage of the Drifilm surface (see section 2.3). After this event, α_{TGA} typically recovers slowly over a period of time which can vary between a couple of hours and a few days. The collected data can be analyzed as described for the temperature scan method, but without need to apply any temperature correction function.
The average κ value over a total of three beam loss events happened during the deuterium running period is:

$$\kappa = 0.859 \pm 0.007 \qquad \text{(Deuterium)} \qquad (2.20)$$

2.7 The Breit-Rabi Polarimeter

The Breit-Rabi polarimeter [Bau02b] measures the relative populations n_i of the hyperfine states of hydrogen (or deuterium) atoms contained in the sample beam. From this measurement, the absolute atomic polarization can be calculated by applying the knowledge of the target magnetic field strength, as described by equations (1.16) and (1.17), for hydrogen, and (1.30) to (1.32) for deuterium.
A schematic view of the Breit-Rabi polarimeter is shown in figure 2.15. The sample

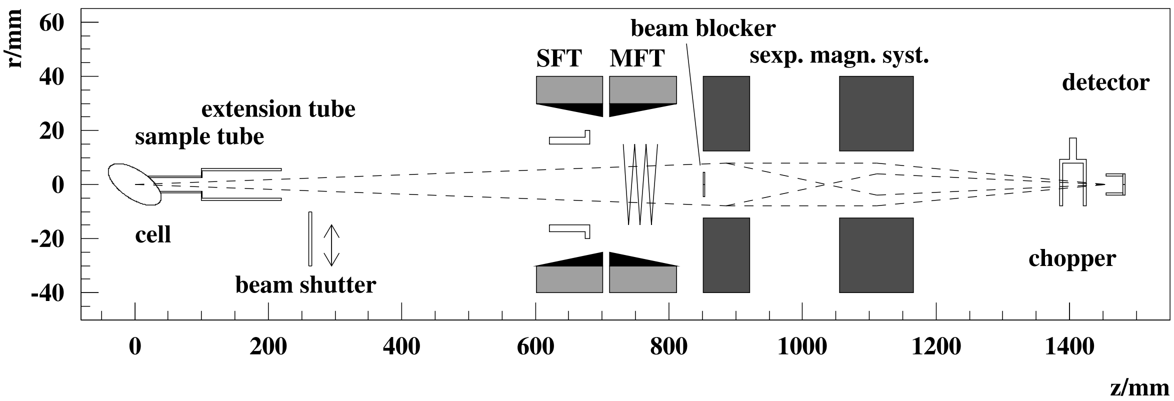

Figure 2.15: Schematic of the BRP. The light gray elements are the two transition units. As in the ABS case, the SFT needs to be replaced and the MFT re-tuned when switching between hydrogen and deuterium. The dark gray elements are the sextupoles. The beam shutter is used to measure the hydrogen contribution coming from dissociative water.

beam, going from left to right, leaves the extension tube encountering first two hyperfine transition units, then a sextuple magnets system and eventually the detector stage. The BRP/TGA vacuum scheme is shown in figure 2.16. A differential pumping system keeps - during operation - pressures of $3{\cdot}10^{-9}$ mbar in the sextupole chamber and $1{\cdot}10^{-10}$ mbar in the detector chamber. This latter chamber is backed out with temperatures up to 220 °C. As already described for the atomic beam source, the transition units are used to exchange the populations between pairs of hyperfine states. The ones employed in the BRP are a strong field transition (SFT) with tilted resonator which can be tuned both as π and σ transition, and a medium field transition (MFT) which can induce different π transitions according to the static field strength and gradient setting. The sextupole system, composed by two magnets, spin filters the sample beam by focusing atoms with $m_s = +\frac{1}{2}$ toward the BRP geometrical axis and defocussing atoms with $m_s = -\frac{1}{2}$ away. The sextupole system has been recently redesigned in order to improve the transmission probability at the working temperature typical of the HERMES target [Bru01]. A 9 mm diameter beam blocker placed in front of the first sextupole magnet ensures that no atoms in the lower energy states can pass through. The detector stage is a copy of the one employed for the target gas analyzer: a cross beam ionizer, a quadrupole mass spectrometer (QMS) and a channel electron multiplier (CEM). In contrast to the TGA, only hydrogen (or deuterium) atoms are detected by the BRP. The chamber residual gas measurement is carried out by using a chopper in the same way described for the TGA.

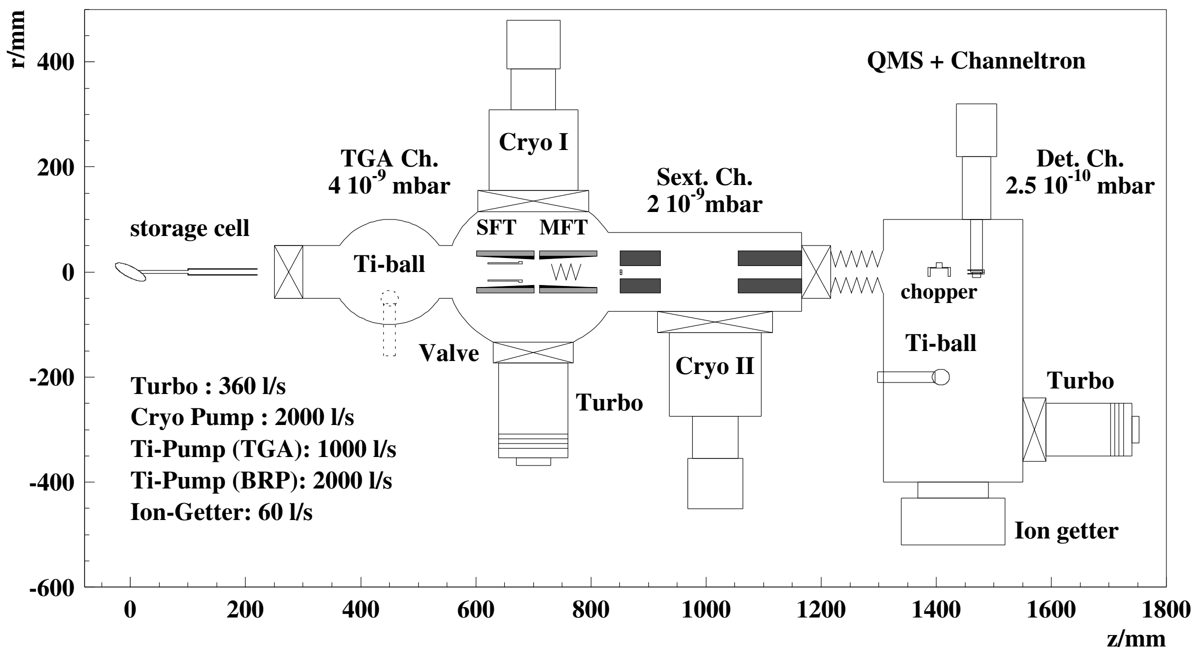

Figure 2.16: Schematic view of the BRP/TGA vacuum system.

An additional beam shutter, placed just after the extension tube exit, is used to measure the possible contribution of atomic hydrogen coming from the dissociation of H_2O and H_2 (D_2O, DHO, D_2 and DH in the deuterium case) present on the vacuum chambers walls[16].

2.7.1 The polarization measurement

The the atomic signal detected by the BRP depends on the transmission probabilities of the sextupole system and on the setting of the transition units. For a stable storage cell temperature, the performance of the magnetic system is fixed. On the contrary, the transition units can be switched on and off, accordingly changing the intensity of the beam reaching the detector.
The BRP signal can be described by the following expression:

$$S_i = c \sum_a \left(\sum_b \sigma_b T^i_{ab} \right) I_a \tag{2.21}$$

where I_a is the sample beam intensity (in atoms·s^{-1}) of the atoms in hyperfine state $|\, a\,\rangle$, T^i_{ab} describes the exchange of hyperfine states by the transition unit i[17], σ_b the sextupole transmission probability for state $|\, b\,\rangle$ and c is a proportionality factor[18].
For a stable sample beam, one can operate the transition units in order to collect a set of linear equations described by

$$S_i = c \sum_a M_{ia} I_a \tag{2.22}$$

where the *measurement matrix* M_{ia} includes information concerning transmission probabilities and transition units efficiencies.
Assuming the knowledge of M_{ia}, one can solve the (2.22) if, during a given ABS injection status, the BRP transition units are operated in at least four (six) different modes in case of hydrogen (deuterium).
The solution is then given by

$$I_a = c^{-1} \sum_i R_{ai} S_i \tag{2.23}$$

[16]The beam shutter was installed at the beginning of the deuterium running period, in 1998. During the 1996/'97 hydrogen running period, the contribution of dissociative hydrogen was taken into account by detecting the amount of masses 2 and 18 amu in addition to mass 1 amu [Bau00].

[17]If both units are working, the matrix T^i has to be replaced by $A = \prod_i T^{(i)}$, as described in section 2.1

[18]The expression (2.21) simplifies into $S_{off} = c \sum_a \sigma_a I_a$ in case that no transition unit is switched on.

where $R = M^{-1}$ [19]. The total intensity I_{tot} can be obtained by the sum over all hyperfine states:

$$I_{tot} = \sum_a I_a \tag{2.24}$$

Finally, the relative hyperfine populations n_a are given by the normalization of the intensities I_a:

$$n_a = \frac{I_a}{I_{tot}} \tag{2.25}$$

The atomic polarization of the sample beam can be now calculated by applying the knowledge of the target magnetic field strength and expressed by the following vectorial forms for hydrogen and deuterium respectively:

$$(P_e, P_z)^T = M_P^H (n_1, n_2, n_3, n_4)^T \tag{2.26}$$

$$(P_e, P_z, P_{zz})^T = M_P^D (n_1, n_2, n_3, n_4, n_5, n_6)^T \tag{2.27}$$

where the matrices M_P^H and M_P^D contain the knowledge of the mixing angles θ (hydrogen) and $\theta_\pm$ (deuterium).

The statistical errors of the measured signals S_i can be represented by the diagonal covariance matrix C_S. Hence, the covariance matrix C_I of the intensities I_a is given by:

$$C_I = R C_S R^T = \left(M^T C_S^{-1} M\right)^{-1} \tag{2.28}$$

The sum over all the elements of C_I gives the statistical error ΔI_{tot} of the total intensity I_{tot}:

$$\Delta I_{tot} = \sum_{ab} (C_I)_{ab} \tag{2.29}$$

The covariance matrix C_N of the hyperfine populations n_a is

$$(C_N)_{ab} = \sum_{cd} \left(\frac{\partial n_a}{\partial I_c}\right) (C_I)_{cd} \left(\frac{\partial n_b}{\partial I_d}\right) \tag{2.30}$$

while the covariance matrix of the polarization vector can be calculated in the following way:

$$C_P = M_P^{H,D} C_N \,(M_P^{H,D})^T \tag{2.31}$$

From C_P one can extract the statistical error of the polarization measurement.

During normal running conditions, the entire procedure lasts roughly 60 s (90 s) for hydrogen (deuterium), resulting in a statistical uncertainty around± 0.013 (for deuterium ± 0.031 for positive and ± 0.022 for negative nuclear polarization). After the optimization of the sextupole system, the statistical error of a 60 s measurement dropped to less than 0.5 %.

[19]If the number of collected signals is larger than the number of unknown, one has to use the *pseudo-inverse* matrix $R = (M^T G_S M)^{-1} M^T G_S$, where G_S is the inverse covariance matrix of the measured signals. This procedure is equivalent to a fit of the intensities I_a to the signals S_i.

2.7.2 The BRP calibration

In the previous section it has been shown that the atomic polarization can be calculated from the measured BRP signals assuming the knowledge of the measurement matrix M. This includes the efficiencies of the transition units and the transmission probabilities of the sextupole system for different hyperfine states. The procedure used to determine these parameters is called BRP calibration.

The basic idea of the calibration measurement is to make the system of equations (2.22) overdetermined so that additional parameters like efficiencies or sextuple transmissions can be extracted through a fit to the data. Due to the several possible combinations of transition units, the amount of signals which can be collected during a polarization measurement exceeds the number of hyperfine states N_{hfs}. Yet, the number of unknowns which can be determined in this way is still less than the total number of parameters. The problem can be easily overcome by cycling this measurement through different N_{ABS} injection modes so that an adequate number of signals can be collected.

The transitions efficiencies

The BRP contains two transition units, a strong field (SFT) and a medium field (MFT). The SFT can drive two transitions for hydrogen ($|1\rangle \leftrightarrow |4\rangle$ and $|2\rangle \leftrightarrow |4\rangle$) and five for deuterium. The efficiencies of the SFT transitions in case of hydrogen are called ε_{s14} and ε_{s24}.

The MFT is a multiple-step transition unit which can drive two sub-transitions for hydrogen ($|1\rangle \leftrightarrow |2\rangle$ and $|2\rangle \leftrightarrow |3\rangle$[20]) and three for deuterium. For hydrogen, the MFT is tuned either as a $|1\rangle \leftrightarrow |3\rangle$ or as $|2\rangle \leftrightarrow |3\rangle$. In the first case the efficiencies of the sub-transitions are called ε_{m13r12} and ε_{m13r23}, whereas in the second case one has ε_{m23r12} and ε_{m23r23}[21]. For deuterium, the scheme of the MFT efficiencies is much more complicated.

Due to the limited space, a cross talk between the two BRP transition units is present when both static fields are switched on, so that the setting of the MFT is influenced by the possible contemporary presence of the SFT field. This means that the MFT has to be tuned as many times as the possible "SFT on" settings (two in case of hydrogen)[22]. As a consequence, the MFT efficiencies have to be measured separately depending on the SFT setting, as they depend on the exact static field. This leads, for hydrogen, to a

[20] The order of the sub-transitions depends on the sign of the gradient field which is, in the HERMES BRP, negative [Bra95].

[21] Although close to zero, the efficiency ε_{m23r12} has to be taken into account.

[22] In order two avoid the additional "SFT off" setting, the SFT static field is always kept on while the MFT is working.

BRP-Signal	Name	MFT-RF	MFT-B	SFT-RF	SFT-B
OFF	off	OFF	OFF	OFF	OFF
SFT 1-4	s14	OFF	OFF	ON	1-4
SFT 2-4	s24	OFF	OFF	ON	2-4
MFT 1-3	m13c14	ON	1-3	OFF	1-4
MFT 1-3	m13c24	ON	1-3	OFF	2-4
MFT 2-3	m23c14	ON	2-3	OFF	1-4
MFT 2-3	m23c24	ON	2-3	OFF	2-4
MFT 1-3/SFT 1-4	m13s14	ON	1-3	ON	1-4
MFT 1-3/SFT 2-4	m13s24	ON	1-3	ON	2-4
MFT 2-3/SFT 1-4	m23s14	ON	2-3	ON	1-4
MFT 2-3/SFT 2-4	m23s24	ON	2-3	ON	2-4

Table 2.3: Possible switching modes of the BRP transition units and corresponding signals for hydrogen running. During a calibration measurement all signals are collected, while for a polarization measurement only a subset of them is chosen.

raise in the number of MFT efficiencies from four to eight. The different MFT efficiencies are identified by means of the subscripts $C14$ (for SFT 1-4 static field on) or $C24$ (SFT 2-4 static field on). For example, the notation $\varepsilon_{m13r23c24}$ represents the efficiency of the transition MFT 1-3, step 2-3, tuned together with the static field of the SFT 2-4. The influence of the MFT field on the SFT is small and can be neglected.
The total number of efficiencies N_{eff} is 10 for hydrogen and 41 in case of deuterium. The number N_{BRP} of possible BRP signals related to different transition states is 11 for hydrogen (as shown in table 2.3) and 29 for deuterium.
If the ABS is operated in N_{ABS} different injection modes, and the BRP transition units switch through all possible N_{BRP} states, than the total number of collected signals is $N_s = N_{ABS}\,N_{BRP}$. In this way, recalling eq. (2.22), one obtains a system of N_s equations containing $N_u = N_{eff} + N_{ABS}\,N_{hfs}$ unknowns[23], where $N_{hft} = 4\,(6)$ in case of hydrogen (deuterium). The system can be solved if $N_f \geq 0$, where N_f is the degree of freedom given by

$$N_f = N_s - N_u = (N_{BRP} - N_{hfs})\,N_{ABS} - N_{eff} \tag{2.32}$$

In such a case, both the hyperfine states intensities I_a and the transitions efficiencies ε can be determined. For hydrogen, the calibration measurement makes use of 7 ABS

[23]During the transitions efficiencies evaluation, the sextuple system transmissions probabilities are kept fixed.

Name	MFT-B	SFT-B	Efficiency	Error
ε_{s14}	-	1-4	99.3	1.34
ε_{s24}	-	2-4	101.0	1.03
$\varepsilon_{s13r12c14}$	1-3	1-4	101.0	1.03
$\varepsilon_{s13r23c14}$			98.6	1.41
$\varepsilon_{s23r12c14}$	2-3	1-4	-1.0	1.13
$\varepsilon_{s23r23c14}$			94.9	1.23
$\varepsilon_{s13r12c24}$	1-3	2-4	99.9	0.42
$\varepsilon_{s13r23c24}$			90.3	0.82
$\varepsilon_{s23r12c24}$	2-3	2-4	0.0	1.10
$\varepsilon_{s23r23c24}$			97.4	1.04

Table 2.4:
BRP transition units efficiencies [%] measured during the 1997 hydrogen running fixing the syxtupole transmission ratio to $\frac{\sigma_2}{\sigma_1} = 1.029$. Each efficiency is shown along with an explanation of the MFT and SFT static field setting.

injection modes, resulting in $N_f = 39$. In case of deuterium two possible options have been developed, one with 5 ABS modes ($N_f = 74$) and the other with 6 ($N_f = 97$).
The solution of the system is carried out by applying a numerical method explained in [Bau02b]. The resulting covariance matrix C_x has the form

$$C_x = \begin{pmatrix} C_\varepsilon & C_{\varepsilon,I} \\ C_{I,\varepsilon} & C_I \end{pmatrix} \tag{2.33}$$

where C_ε contains uncertainties and covariances of the efficiencies and it is used to calculate the systematic uncertainty of the polarization measurement which results in the order of 1.5 %.
Table 2.4 summarizes the transition efficiencies measurement performed in 1997 with hydrogen.

The sextupole transmissions

In the previous section it has been shown how the efficiencies ε_i of the BRP transition can be measured, assuming the a priori knowledge of the sextupole transmissions σ_n for different hyperfine states. The attempt to fit both ε_i and σ_n within the same algorithm fails. Nevertheless, the transmission probabilities can be determined by splitting the fitting procedure in two steps, as it will be shown in the following.
In the BRP setup, atoms with $m_S = -\frac{1}{2}$ are either defocused or stopped by the beam blocker, having therefore zero transmission probability. Moreover, due to the normalization (2.25), only ratios of transmission probabilities are required for measuring the hyperfine populations. Thus, the remaining required parameters are σ_2/σ_1 for hydrogen and σ_2/σ_1 and σ_3/σ_1 for deuterium. Due to the smaller electron-nucleon coupling

(B_C^D =11.7 mT against B_C^H =50.7 mT), in the deuterium case the Stern-Gerlach force depends entirely, in high fields, on m_S, so that the ratios σ_2/σ_1 and σ_3/σ_1 for deuterium can assumed to be one. From these consideration it follows that the only transmission ratio that needs to be measured is $r_{21} = \sigma_2/\sigma_1$ for hydrogen.
From the BRP calibration the transition efficiencies are extracted as functions of the parameter r_{21}. The transmission ratio can than be evaluated by minimizing the χ^2 of the calibration results. As the transmission probability of the sextupole system depends on the velocity distribution of the atomic sample, the storage cell temperature T_{cell} has to stay constant over the calibration measurement. This procedure applied to a calibration measurement taken at T_{cell} =95 K has produced the following result [Bau00]:

$$\left.\frac{\sigma_2}{\sigma_1}\right|_{95\,K} = 1.029 \pm 0.0015 \tag{2.34}$$

The small error of the measured ratio is neglected in the calculation of the systematic uncertainty of the polarization measurement.
The potential cell temperature dependence of the transition efficiencies can be neglected as the velocity distribution of the sample is fixed by the sextupole system. Therefore, a polarization measurement performed collecting at least one signal more than the minimum required number (as it always the case) can be used to fit the ratio r_{21} for different cell temperatures.

2.8 The luminosity monitor

The HERMES luminosity monitor (Lumi) [Due90, Ben94, Ben98, Wei98] is a part of the HERMES spectrometer[24] [Ack98] and detects the Bhabha scattering ($e^+e^- \rightarrow e^+e^-$) and the positron electron annihilation ($e^+e^- \rightarrow \gamma\gamma$) of the HERA positron beam with the electrons of the target gas under small angles. If the HERA storage ring is filled with electrons, the detected process is represented by the Moeller scattering ($e^-e^- \rightarrow e^-e^-$). The number of events is proportional to the electron density inside the storage cell and therefore to the number of nucleons in the target.
The (coincidence-) countrate in the luminosity monitor R_L is given by:

$$R_L = \sigma \,\frac{I_{beam}}{e}\, D_t\,, \tag{2.35}$$

where I_{beam} is the HERA beam current, e is the charge of the electron and D_t the integrated target thickness (of electrons). σ is the total cross section for detectable processes integrated over the detector acceptance and can be obtained by a Monte Carlo simulation.

[24]An overview of the HERMES spectrometer is given in appendix B.

The resulting average nucleus[25] volume density $\langle\, n \,\rangle$ is then:

$$\langle\, n \,\rangle = \frac{e}{\sigma\, 2\, L}\, S_L\,, \tag{2.36}$$

where L is the length of one wing of the storage cell ($L = 20\, cm$ and $S_L = \frac{R_L}{I_{beam}}$ is the relative Lumi countrate.
As the target density scales like $1/\sqrt{T_{cell}}$, where T_{cell} is the temperature of the storage cell, one can define a the normalized quantity[26]

$$\langle\, n \,\rangle_{norm} = \langle\, n \,\rangle\, \sqrt{\frac{T_{cell}}{100}} \tag{2.37}$$

which can be related to the target average atomic fraction, provided that the ABS performance is stable.

Besides the density measurement, the luminosity monitor can be used to determine the electron polarization of the target. This can be done by looking at the rate asymmetry for different target injection modes:

$$A = \frac{\sigma^{\uparrow\uparrow} - \sigma^{\uparrow\downarrow}}{\sigma^{\uparrow\uparrow} + \sigma^{\uparrow\downarrow}} = \frac{N^{\uparrow\uparrow} L^{\uparrow\downarrow} - N^{\uparrow\downarrow} L^{\uparrow\uparrow}}{N^{\uparrow\uparrow} L^{\uparrow\downarrow} + N^{\uparrow\downarrow} L^{\uparrow\uparrow}} \tag{2.38}$$

where $\sigma^{\uparrow\uparrow}$ ($\sigma^{\uparrow\downarrow}$) is the total polarized cross section for pairs of particles with parallel (antiparallel) spin integrated over the detector acceptance, whereas $N^{\uparrow\uparrow} L^{\uparrow\downarrow}$ ($N^{\uparrow\downarrow} L^{\uparrow\uparrow}$) is the correspondent luminosity corrected count rate.
The target electron polarization P^T is related to the measured asymmetry A through:

$$P^T = \frac{A}{\bar{a}_{zz}\, P_b} \tag{2.39}$$

P_b representing the beam polarization[27] measured by the two HERA e-beam polarimeters, while $\bar{a}_{zz}$ is either given by the average between the Bhabha scattering and e^+e^- annihilation asymmetry factors for a positron beam, or by the Moeller scattering asymmetry factor for an electron beam. The acceptance corrected term $\bar{a}_{zz}$ can be computed numerically using the analytical expressions of cross sections and asymmetry factors or, alternatively, through a montecarlo simulation [Pot98]. During "normal" data taking, the target is alternately filled with positive - hydrogen (deuterium) hyperfine states $|\, 1 \,\rangle$ and $|\, 4 \,\rangle$ ($|\, 1 \,\rangle$ and $|\, 6 \,\rangle$) - and negative - $|\, 2 \,\rangle$ and $|\, 3 \,\rangle$ ($|\, 3 \,\rangle$ and $|\, 4 \,\rangle$) - nuclear polarization, so that the polarization of the electrons is typically very close to zero and no asymmetry can be measured by the lumi. However, this possibility can be exploited during special so-called *Bhabha* or *Moeller* runs, during which the target electron polarization is flipped.

[25] The number of electrons in the target gas is equal to the number of nuclei.

[26] The reference value $T_{cell} = 100\,\mathrm{K}$ corresponds to the working point temperature of the hydrogen target.

[27] The electron/positron beam of the HERA storage ring is self polarized due to the Sokolov-Ternov mechanism [Sok64].

Chapter 3

The Polarization of the HERMES Target

The average polarization P^T of nucleons in the target is a fundamental parameter of the HERMES experiment. In particular, since the systematic uncertainty of any polarized data analysis is directly affected by the target polarization total error, a great effort has to be made in order to increase as much as possible its accuracy. In this chapter the target polarization formula is given along with a detailed explanation of the calculation of all the single terms.

3.1 Target average polarization definition

An ideal target would be composed by polarized hydrogen or deuterium atoms only. In reality, a non negligible amount of molecules is present as well. If all molecules were unpolarized, the target polarization formula would be

$$P_u^T = \alpha P_a \tag{3.1}$$

P_a representing the polarization of atoms and α the fraction of nucleons contained in atoms:

$$\alpha = \frac{N_a}{N_a + 2N_m} \tag{3.2}$$

where N_a and N_m are the atomic and molecular populations.
The situation is complicated due to the potential presence of molecules which recombined after entering the storage cell [Bau02d]. These molecules may have a remnant nuclear polarization $P_m = \beta P_a$ that has to be taken into account. Hence, the atomic fraction must be factorized into two pieces:

$$\alpha = \alpha_0 \cdot \alpha_r \tag{3.3}$$

where α_0 is the atomic fraction accounting for unpolarized molecules and α_r is the fraction of atoms that do not recombine before leaving the cell:

$$\alpha_0 = \frac{N_a + 2N_r}{N_a + 2N_m} \tag{3.4}$$

$$\alpha_r = \frac{N_a}{N_a + 2N_r} \tag{3.5}$$

where N_r is the population of recombined molecules.
Now the average target polarization final formula can be written in the following way:

$$P^T = \alpha_0[\alpha_r + (1 - \alpha_r)\beta]P_a \tag{3.6}$$

None of the terms of the (3.6) can be measured directly. P_a and α_r can be estimated from the BRP and TGA measurements P_a^{BRP} and α_r^{TGA}[28] by applying the so-called *sampling corrections* c_P and c_α respectively, as explained in section 3.5:

$$P_a = c_P \cdot P_a^{BRP} \tag{3.7}$$

$$\alpha_r = c_\alpha \cdot \alpha_r^{TGA} \tag{3.8}$$

whereas, in the limit of small recombination, the nominal atomic fraction α_0 can be derived from the TGA measurements as shown in the next section.
The evaluation of the polarization of recombined molecules goes beyond the capabilities of the HERMES target alone[29]. Nevertheless, an estimation of β for the hydrogen running period has been made by taking advantage of a set of high temperature data and using the parallel double spin asymmetry measurement from the HERMES spectrometer. This measurement will be shown in the next chapter.

3.2 The atomic fractions α_0 and α_r

In the previous section the cell average atomic fractions α_0 and α_r were defined in terms of populations N_i. In the following, it will be shown that two correspondent quantities, α_0^{TGA} and α_r^{TGA} can be measured by the TGA in terms of flowrates ϕ_i. Hence, a relation between populations and flowrates has to be developed in oder to transfer the TGA results to the target cell. Moreover, the atomic fractions of the gas sample are different from the average target correspondent values for two reasons. First, the gas sample comes from the center of the cell, where the particles collision age and density differ from the average values. Further, potential recombination of atoms inside the sample tube can change the relative atomic and molecular flowrates. The relation between the properties of the sample gas and the whole target is discussed in section 3.5.

[28] A definition of α_r^{TGA} will be given in section 3.2.1
[29] The Breit-Rabi polarimeter can measure the atomic polarization only.

3.2.1 The factorization of the measured atomic fraction α^{TGA}

In section 2.6.1 the definition of the measured atomic fraction α^{TGA} was given:

$$\alpha^{TGA} = \frac{\phi_a}{\phi_a + \phi_m} \tag{3.9}$$

where ϕ_a and ϕ_m are the normalized atomic and molecular flowrates measured by the TGA and defined by (2.12) and (2.13) respectively.
The molecules present inside the storage cell come from three sources:

- Undissociated molecules ballistically injected through the ABS. Since the efficiency of the dissociator is around 80 %, a consintent amount of molecules passes through the nozzle toward the polarizing stage, unaffected neither by the sixtupole magnet nor by the transition units. The majority of these molecules hits the vacuum chamber wall and is pumped away; still a not negligible amount has the right trajectory to enter into the storage cell through the injection tube. These unpolarized molecules present a triangular density distribution along the cell axis, constantly decreasing going from the center to the edges.

- The rest gas in the target chamber. These molecules are mainly due to the recombination of atoms that have left the storage cell and have thermalized on the vacuum chamber walls (at room temperature). This molecular component is clearly unpolarized and presents a constant density distribution along the longitudinal direction of the storage cell.

- Atoms that recombine into molecules after entering the cell. As explained in section 2.3, the cell material and temperature are optimized in order to limit the potential degradation of target atomic gas. Nevertheless, atoms can stick on the cell surface and recombine. The resulting molecules may carry a residual nuclear polarization and present a triangular density distribution along the cell longitudinal dimension.

Hence, the normalized total molecular flowrate ϕ_m can be decomposed in the following way:

$$\phi_m = \phi_{bal} + \phi_{rg} + \phi_r \tag{3.10}$$

where ϕ_{bal}, ϕ_{rg} and ϕ_r represent the ballistic, the rest gas and the recombination components respectively.
The TGA measured quantity correspondent to α_0 is called α_0^{TGA} and defined by:

$$\alpha_0^{TGA} = \frac{\phi_a + \phi_r}{\phi_a + \phi_r + \phi_{bal} + \phi_{rg}} \tag{3.11}$$

The measured atomic fraction surviving recombination, α_r^{TGA}, is given by:

$$\alpha_r^{TGA} = \frac{\phi_a}{\phi_a + \phi_r} \tag{3.12}$$

so that, also for the measured quantities, the relation $\alpha^{TGA} = \alpha_0^{TGA} \cdot \alpha_r^{TGA}$ holds.
The separation of the total molecular flowrate into the single components can be performed by means of standard *target calibrations* which can be usually performed between two HERA electron fills, when HERMES is not taking data.

The rest-gas calibration

The rest gas contribution ϕ_{rg} to the total molecular flowrate ϕ_m can be estimated by injecting H_2 (or D_2) through the unpolarized gas feed system into the target vacuum chamber[30]. By varying the amount of injected gas and measuring TGA molecular rate and target chamber pressure p_{tc}, one can get the rest gas calibration constant c_{rg} through

[30]During this calibration, the separation valve between the ABS and the storage cell/target chamber is closed, so that no molecular contribution can come from the atomic beam source.

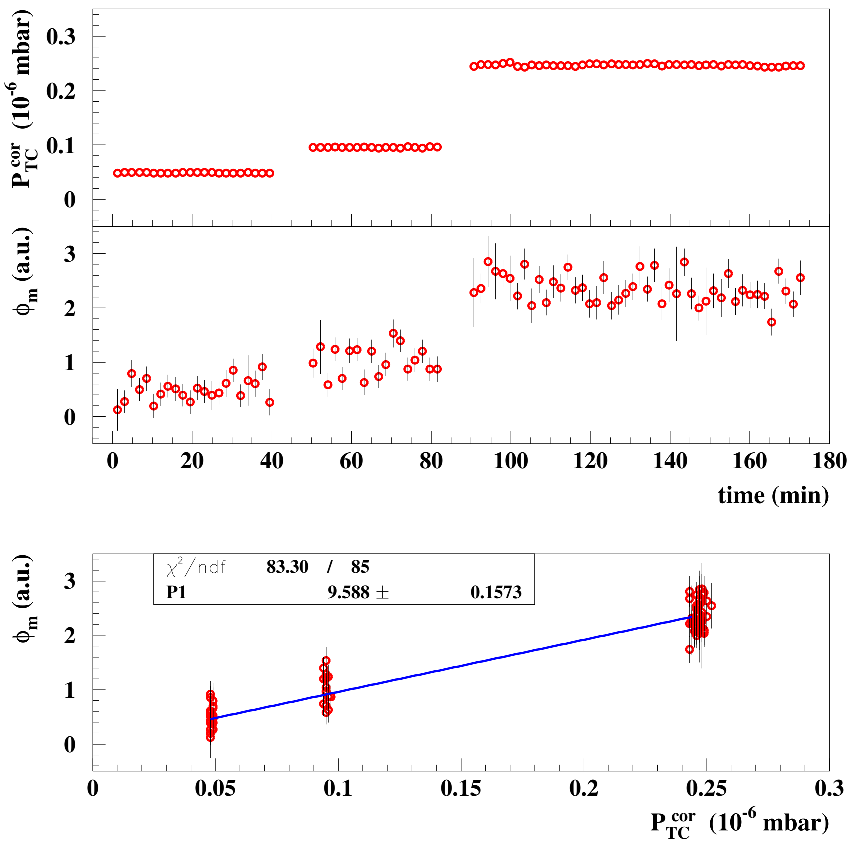

Figure 3.1:
A deuterium rest gas calibration. The upper graphs show the target chamber pressure (corrected for the base pressure) and the TGA molecular flowrate as functions of time. For each step, a measurement of at least 40 minutes was taken in order to collect statistics. The lower graph presents the straight line fit giving the calibration constant c_{rg}. All flowrates are expressed in arbitrary units because of the applied emission current normalization.

a straight line fit to the data:

$$\phi_{rg} = c_{rg} \cdot (p_{tc} - p_{tc}^{bas}) \tag{3.13}$$

where p_{tc}^{bas} is the target chamber *base pressure*, i.e. when no gas is being injected. The measurement is typically performed by increasing stepwise the molecular density in order to get three pressure average values corresponding to roughly one half, one and two times the nominal pressure when the ABS is used. Figure 3.1 shows a deuterium rest gas calibration taken in 2000, on March the 13^{th}.
The possibility of retrieving at any time the rest gas flowrate from the pressure value is somehow limited by the non perfect temporal stability of the pressure gauges[31]. In order to overcome this problem, the rest gas calibration is usually performed on a weekly basis.

The ballistic flux calibration

The amount of ballistically injected molecules can be measured by taking advantage of the ABS high frequency transition units. Indeed, as the molecules trajectory are not affected by magnetic fields, by switching on and off the transitions between the sextupole magnets one can vary the total injected atomic flux keeping constant the molecular one. During the 1996-'97 hydrogen running period, the atomic density could be halved by using the MFT 1-3/2-3 unit. With deuterium, the additional SFT allowed the choice between three densities, obtained by injected one, two or three hyperfine states.
As in the HERMES storage cell the volume recombination is negligible, one can assume that the fraction of recombined molecules is proportional to the injected atomic flux. Hence, the following equation for the total molecular flowrate ϕ_m holds:

$$\phi_m^{(i)} - \phi_{bal} - \phi_{rg}^{(i)} = \Big(\frac{1}{\alpha_r^{TGA}} - 1\Big)\phi_a^{(i)} \tag{3.14}$$

where the index (i) represents the ABS injection mode.
By the division of the equations for two injection modes providing different target densities, one finds:

$$\phi_{bal} = \frac{(\phi_m^{(2)} - \phi_{rg}^{(2)})\phi_a^{(1)} - (\phi_m^{(1)} - \phi_{rg}^{(1)})\phi_a^{(2)}}{\phi_a^{(1)} - \phi_a^{(2)}} \tag{3.15}$$

with ϕ_a and ϕ_m measured by the TGA and ϕ_{rg} provided by the (3.13).
With this technique a measurement time of several hours is necessary in order to get an acceptable statistical uncertainty (roughly 30% in five hours). This is usually not possible in the framework of the HERMES experiment, as the time between two electron fills is

[31]The rest gas pressure in the target chamber is proportional to the ABS atomic flux injected into the storage cell. The number of rest gas molecules reaching the TGA depends in addition on the conductance from the vacuum chamber to the ionizing volume. If the geometry of the system doesn't change and the ABS runs in a stable way, the amount of rest gas seen by the target gas analyzer should not change.

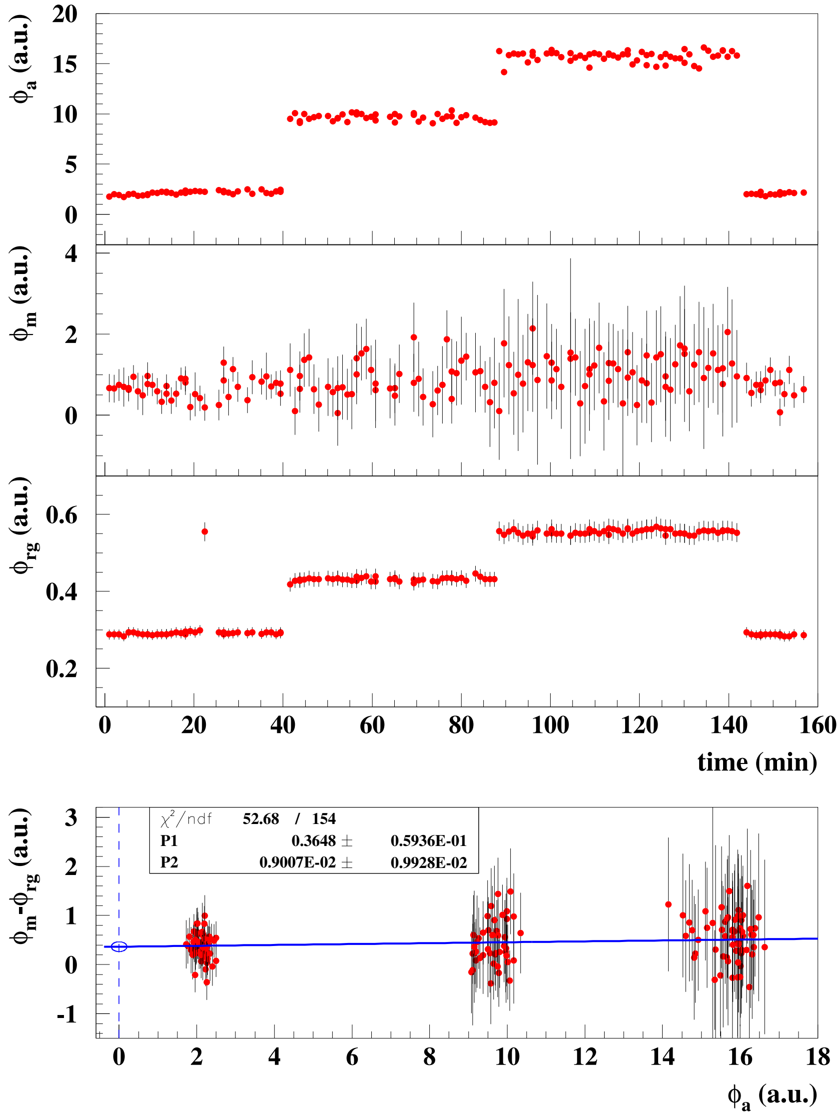

Figure 3.2:
A hydrogen ballistic flux calibration. The upper graphs show atomic, total molecular and rest gas flowrates respectively. This latter has been calculated from the measurement of the corrected target chamber pressure. The three densities steps have been produced injecting zero, one and two hyperfine states respectively. The lower graph presents the straight line fit giving the calibration constants ϕ_{bal} (intercept) and c_r (slope). All flowrates are expressed in arbitrary units because of the applied emission current normalization.

limited to one to two hours. This problem has been overcome during the 2002 hydrogen running period, by installing an additional strong field transition unit between the ABS sextupole magnets. The combined use of SFT 2-4 and MFT/WFT 1-3 allows to defocus all hyperfine states ($|3\rangle$ and $|4\rangle$ by means of the first sextupole subsystem and $|1\rangle$ and $|2\rangle$ with the second one), obtaining therefore an almoust pure flux of ballistically injected molecules[32]. By using this so-called *zero state* injection mode in combination with the one and two states modes, one can measure the total molecular rate as function of the atomic one for three different target densities. The ballistic flowrate ϕ_{bal} is then given by the linear extrapolation of the rest gas subtracted molecular flowrate at zero injected

[32]A residual atomic contamination is due to the non perfect efficiencies of the HFT units.

atomic flux[33]:

$$\phi_{bal} = (\phi_m - \phi_{rg})|_{\phi_a=0} \tag{3.16}$$

This measurement technique has lead to a large reduction of the statistical uncertainty which is now in the order of 30 % after only one and half hours.
Besides, the slope of the fitting straight line c_r relates the recombination flowrate ϕ_r with the atomic flowrate ϕ_a:

$$\phi_r(\phi_a) = c_r \cdot \phi_a \tag{3.17}$$

Figure 3.2 shows a ballistic flux calibration performed in 2002, on November the 18^{th}.

3.2.2 The relation between target average populations and TGA flowrates

In the pressure conditions of the HERMES target, atoms and molecules move along the storage cell tube in a molecular flow regime[34] [Knu09, Smo10, Gae13]. As already mentioned in section 2.3, particles are injected through a side tube directly into the center of the cell from where they steadily flow toward the edges of the beam tube and through the sample tube[35]. One can therefore relate the particles flow Φ to the pressure drop along the tube Δp with the following expression:

$$\Phi = C\Delta p \tag{3.18}$$

where C, called *conductance* of the tube, depends on geometry and the temperature of the tube, as well as the mass of the particles.
If the total atomic flux Φ_a^{tot} delivered by the ABS is constant, one has[36]:

$$\Phi_a + 2\Phi_r = -C_a\, L\, \frac{dp_a}{dz} - 2\, C_m\, L\, \frac{dp_r}{dz} = \Phi_a^{tot} = const \tag{3.19}$$

where $\Phi_{a,r}$ are the atomic and molecular recombination fluxes, $C_{a,m}$ the atomic and molecular conductances, z is the distance from the center along the cell axis and L is the length of the beam tube.
For fixed geometry and temperature, the relation between the atomic and molecular conductance is given by

$$C_a = \frac{1}{\sqrt{2}} C_m \tag{3.20}$$

[33] The subtraction of the rest gas from the total molecular flowrate is necessary because, due to the pressure gradient, even at zero injected atomic flux a certain amount of atoms can flow from the ABS to the target vacuum chamber and there recombine.

[34] Molecular flow in long tubes takes place when the mean free path length is large compared to the typical transverse dimension of the tube. The opposite regime is usually called continuum or viscous flow.

[35] In this context," sample tube" means the systems composed by sample and extension tube.

[36] In what follows, the rest gas and ballistic molecular fluxes are neglected.

From the (3.19) and (3.20), the pressure drop along the storage cell beam tube can be calculated, finding the following result:

$$p(z) = p_a(z) + \sqrt{2}\,p_r(z) = p_0\Big(1 - \frac{|z|}{L}\Big) \tag{3.21}$$

where $p_{a,r}$ are the atomic and molecular (recombined atoms) partial pressures and p_0 is the central total pressure.
As the atomic recombination probability increases with the number of wall collisions, the atomic and molecular partial pressures change along the beam tube. Following the notation of [Bau02a], one can define the normalized atomic, molecular recombination and total densities:

$$\rho_a(z) = \frac{p_a(z)}{p_a(z) + \sqrt{2}\,p_r(z)} \tag{3.22}$$

$$\rho_r(z) = \frac{\sqrt{2}\,p_r(z)}{p_a(z) + \sqrt{2}\,p_r(z)} \tag{3.23}$$

$$\rho_t(z) = \frac{p_a(z) + 2\,p_r(z)}{p_a(z) + \sqrt{2}\,p_r(z)} \tag{3.24}$$

so that

$$\rho_a(z) + \rho_r(z) = 1 \tag{3.25}$$

and

$$\rho_t(z) = \rho_a(z) + \sqrt{2}\,p_r = \sqrt{2} - (\sqrt{2} - 1)\rho_a(z) \tag{3.26}$$

hold.
Thus, the z dependence of the atomic fraction α_r can be expressed in the following way:

$$\alpha_r(z) = \frac{\rho_a(z)}{\rho_t(z)} = \frac{\rho_a(z)}{\sqrt{2} - (\sqrt{2} - 1)\rho_a(z)} \tag{3.27}$$

while ρ_a is related to α_r through

$$\rho_a(z) = \frac{\sqrt{2}\,\alpha_r(z)}{1 + (\sqrt{2} - 1)\alpha_r(z)} \tag{3.28}$$

All the equations from (3.23) to (3.28) hold of course also for the target average values ρ_a, ρ_r, ρ_t and α_r.
If there is no recombination inside the sample tube, the flowrates ϕ_a and ϕ_r are directly proportional to the corresponding atomic and molecular partial pressures in the storage cell center:

$$\begin{aligned} \phi_a &\propto p_a(0)\,C_a \\ \phi_r &\propto 2\,p_r(0)\,C_m \end{aligned} \tag{3.29}$$

Applying the (3.20), one finds:

$$\alpha_r^{TGA} = \frac{\phi_a}{\phi_a + \phi_r} \underset{no\ rec.\ in\ s.t.}{=} \frac{p_a(0)}{p_a(0) + \sqrt{2}\, p_r(0)} = \rho_a(0) \tag{3.30}$$

As the average atomic densities in the beam tube ρ_a is always less than its central value $\rho_a(0)$,

$$\rho_a \leq \rho_a(0) \tag{3.31}$$

applying the (3.28) and the (3.30) to the (3.31), one finds that, in case that no recombination happens in the sample tube, the following upper limit for α_r holds

$$\alpha_r \underset{no\ rec.\ in\ s.t.}{\leq} \frac{\alpha_r^{TGA}}{\sqrt{2} - (\sqrt{2} - 1)\alpha_r^{TGA}} \tag{3.32}$$

The average atomic fractions α_0 and α_r were defined in section 3.1 in terms of populations N_i:

$$\alpha_0 = \frac{N_a + 2N_r}{N_a + 2N_r + 2N_{bal} + 2N_{rg}} \tag{3.33}$$

$$\alpha_r = \frac{N_a}{N_a + 2N_r} \tag{3.34}$$

One can now relate the populations N_i to the corresponding central partial pressure $p_i(0)$ through:

$$N_a + 2\, N_r \propto p(0) = [p_a(0) + \sqrt{2}\, p_r(0)]\, \rho_t \tag{3.35}$$

$$2\, N_{bal} \propto 2\, p_{bal}(0) \tag{3.36}$$

$$2\, N_{rg} \propto 2\, p_{rg}(0)\, q_{rg} \tag{3.37}$$

The term ρ_t in the (3.36) weights the atomic and recombination pressures by taking into account the relative number of recombined molecules over the total injected atomic population.

The parameter q_{rg} in the (3.37) is defined as:

$$q_{rg} = \frac{p_{bal}(0)}{p_{bal}} \frac{p_{rg}}{p_{rg}(0)} \simeq 2 \tag{3.38}$$

where p_{bal} (p_{rg}) indicates the average pressure due to ballistically injected (rest gas) molecules. q_{rg} takes into account the different spatial distribution of $p_{rg}(z)$ compared to $p(z)$ and $p_{bal}(z)$. As the first distribution is almost uniform, while the second ones are approximately triangular, one can assume $q_{rg} \simeq 2$ as a reasonable estimation.

On the other hand, also the TGA measured flowrates ϕ_i can be related to the central pressures p_i through the expressions:

$$\phi_a + \phi_r \;\propto\; C_a^s\, p_a(0) + 2\, C_m^s\, p_r(0) \propto p_a(0) + \sqrt{2}\, p_r(0) \tag{3.39}$$

$$\phi_{bal} \;\propto\; 2\, C_m^s\, p_{bal}(0) \propto \sqrt{2}\, p_{bal}(0) \tag{3.40}$$

$$\phi_{rg} \;\propto\; 2\, C_m^s\, p_{rg}(0) \propto \sqrt{2}\, p_{rg}(0) \tag{3.41}$$

where C_a^s (C_m^s) is the atomic (molecular) conductance of the sample tube.
Putting together the (3.36) to (3.37) and the (3.40) to (3.41), one can operate the following substitutions:

$$N_a + 2\, N_r \;\rightarrow\; (\phi_a + \phi_r)\, \rho_t \tag{3.42}$$

$$2\, N_{bal} \;\rightarrow\; \sqrt{2}\, \phi_{bal} \tag{3.43}$$

$$2\, N_{rg} \;\rightarrow\; 2\sqrt{2}\, \phi_{rg} \tag{3.44}$$

Hence, the nominal atomic fraction α_0 can be now rewritten in terms of flowrates:

$$\alpha_0 = \frac{\rho_t\, (\phi_a + \phi_r)}{\rho_t\, (\phi_a + \phi_r) + \sqrt{2}\, (\phi_{bal} + 2\, \phi_{rg})} \tag{3.45}$$

where the average total normalized density ρ_t is given in terms of α_r by

$$\rho_t = \frac{\sqrt{2}}{1 + (\sqrt{2} - 1)\alpha_r} \tag{3.46}$$

If very low recombination occurs, $\alpha_r \simeq 1$ and therefore $\rho_t \simeq 1$. In such a case, the dependence of α_0 on α_r can be neglected:

$$\alpha_0 \simeq \frac{\phi_a + \phi_r}{\phi_a + \phi_r + \sqrt{2}(\phi_{bal} + 2\, \phi_{rg})} \tag{3.47}$$

In order to calculate α_r, one needs to disentangle the contributions of N_a and N_r in the (3.43). This can be realized only by applying the sampling correction c_α as explained in section 3.5.

3.3 The atomic polarization P_a

Two factors contribute to the average value of the atomic polarization P_a: the ABS performance, which gives the atomic injected polarization P_a^{inj}, and the spin relaxation processes which can potentially happen inside the storage cell, causing a relative polarization loss ΔP_a defined by:

$$\Delta P_a = \frac{P_a^{inj} - P_a}{P_a^{inj}} \tag{3.48}$$

The atomic polarization measurement, P_a^{BRP} is carried out by the BRP on a gas sample coming from the center of the cell. The relation correspondent to the (3.50) is

$$\Delta P_a^{BRP} = \frac{P_a^{inj} - P_a^{BRP}}{P_a^{inj}} \tag{3.49}$$

As the depolarization mechanisms depend on the particles collision age as well as the atomic density, ΔP_a and ΔP_a^{BRP} do not necessarily match. Moreover, as the spin relaxation is due to different processes, ΔP_a^{BRP} can be related to ΔP_a only after the separation of the single depolarization contributions. BRP measurements and target average values can then be connected through the sampling correction c_P that will be introduced in section 3.5. The complete formula for the calculation of the atomic polarization P_a will be presented in section 3.6.2.

3.3.1 Spin relaxation processes in the HERMES target

In the HERMES hydrogen/deuterium target there are three known causes for spin relaxation [Bra95, Kol98, Bau00]:

- wall collisions [And63, Bou63a, Bou63b, Bou65];
- spin exchange collisions [Pur56, All72, Des76, Koe88, Wal93];
- bunch field induced depolarization [Ack99, Reg99].

Therefore, the total atomic depolarization ΔP_a can be separated into three components:

$$\Delta P_a = \Delta P_a^{wd} + \Delta P_a^{se} + \Delta P_a^{bd} \tag{3.50}$$

where the indices *wd*, *se* and *bd* refer to wall, spin exchange and bunched field depolarization respectively.

Wall collisions

An atom diffusing along the cell collides several times onto the wall before exiting through the beam tube's ends. A Van-der-Waal force between the atom and the surface constrains the particle to stay for a certain period of time close to the wall until its energy, following the Boltzmann distribution, is large enough to cause the desorption. The mean occupation time on the wall τ_s is given by the Arrenius equation:

$$\tau_s = \tau_0 \, e^{\left(\frac{E_b}{kT}\right)} \tag{3.51}$$

where τ_0 is the high temperature limit of τ_s, E_b and T are the adsorption energy and temperature respectively and k is the Boltzmann constant. During the time τ_s (in the order of $10^{-10}\,s$ for the HERMES), the electronic magnetic moment of the adsorbed atom interacts with magnetic moments on the surface by means of dipolar coupling and/or with other unpaired electrons through exchange interactions. As a result, during a wall collision there is a certain probability γ_z (γ_e) for an atom to change its nuclear (electron) spin state through a hyperfine transition $|\,a\,\rangle \rightarrow |\,b\,\rangle$ (compare section 1.2):

$$\gamma_z, \gamma_e \propto \tau_s^2 \tag{3.52}$$

In a high magnetic holding field limit where the electron and nucleon spins are effectively decoupled, the nuclear depolarization probability is strongly suppressed compared to the electron one.

Spin exchange collisions

Atoms colliding with each other in the gas phase undergo spin exchange, where the hyperfine states can be modified via an interaction between the electron spins. The number of spin exchange collisions per unit time and volume is

$$\dot{N}_{se} = n\sigma_{se}\,\langle\, v_r\,\rangle \tag{3.53}$$

where n is the gas density, σ_{se} is the spin exchange cross section and v_r is the relative velocity of the atoms. Due to the conservation of the angular momentum, the sum of the magnetic quantum numbers m_F before and after the spin exchange collision has to be the same:

$$\Delta \sum_i m_F = 0 \tag{3.54}$$

The allowed hyperfine transitions for any given pair of colliding hydrogen or deuterium atoms is shown in table 3.1.
The depolarization probability per spin exchange collision γ_{se} is given by

$$\gamma_{se} \approx \frac{1}{x^2} \tag{3.55}$$

$\sum_i m_F$	Hydrogen	Deuterium
3		$|\,11\,\rangle$
2	$|\,11\,\rangle$	$|\,12\,\rangle$ $|\,16\,\rangle$
1	$|\,12\,\rangle$ $|\,14\,\rangle$	$|\,13\,\rangle$ $|\,15\,\rangle$ $|\,22\,\rangle$ $|\,26\,\rangle$ $|\,66\,\rangle$
0	$|\,13\,\rangle$ $|\,22\,\rangle$ $|\,24\,\rangle$ $|\,44\,\rangle$	$|\,14\,\rangle$ $|\,23\,\rangle$ $|\,25\,\rangle$ $|\,36\,\rangle$ $|\,56\,\rangle$
-1	$|\,23\,\rangle$ $|\,34\,\rangle$	$|\,24\,\rangle$ $|\,33\,\rangle$ $|\,35\,\rangle$ $|\,46\,\rangle$ $|\,55\,\rangle$
-2	$|\,33\,\rangle$	$|\,34\,\rangle$ $|\,45\,\rangle$
-3		$|\,44\,\rangle$

Table 3.1: Pairs of hyperfine states of hydrogen and deuterium, for which spin exchange collisions are allowed by angular momentum conservation.

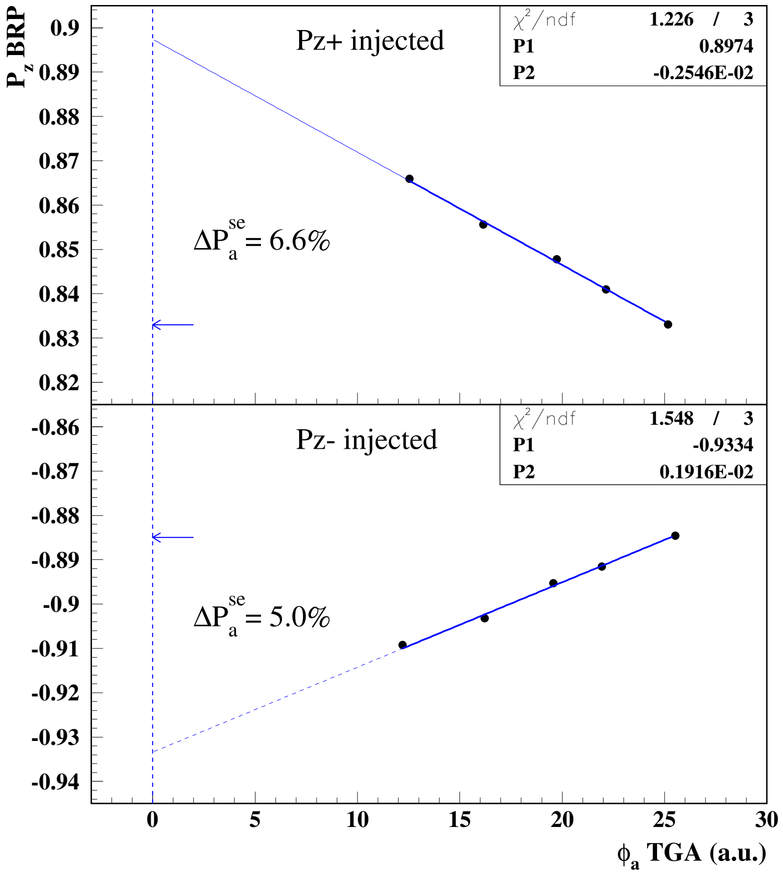

Figure 3.3: Measurement of the spin exchange contribution ΔP_a^{se} taken during the transverse running period and smaller cell for positive (top) and negative injected nuclear polarization. Each plot shows the dependence of the measured nuclear polarization P_z on the atomic target density, here expressed in terms of TGA atomic flowrate ϕ_a. The intercepts of the fitting straight lines give the extrapolated polarizations if no spin exchange relaxation were present. The arrows indicate the polarizations at nominal atomic density. The discrepancy between the two values is an artifact of the missing BRP calibration.

where $x = B/B_C$ is the external magnetic field strength normalized to the critical field, already introduced in the first chapter.

The density dependence of the spin exchange collisions can be used to evaluate the contribution ΔP_a^{se} to the total target depolarization ΔP_a. If one measures the BRP atomic polarization P_a^{BRP} and the TGA atomic flowrate ϕ_a for different target atomic densities[37] and fits the data with a straight line, the extrapolation to the case of zero injected atomic flux (zero atomic density) gives the polarization value $(P_a^{BRP})_0$ that one would have if no spin exchange relaxation were present. Hence, the quantity $\Delta(P_a^{se})^{BRP}$, defined by

$$\Delta(P_a^{se})^{BRP} = \frac{(P_a^{BRP})_0 - (P_a^{BRP})_1}{P_a^{inj}} \tag{3.56}$$

where $(P_a^{BRP})_1$ is the atomic polarization measured at nominal density, represents the BRP measurement of the relative polarization loss by spin exchange. Estimations of the injectid polarization for hydrogen and deuterium are given in section 3.3.2.

Since the sampling correction for the spin exchange relaxation is negligible, as it will be

[37]The atomic density of the polarized target can by decreased in several steps either by lowering the power of the radio-frequency dissociator, or by changing the nozzle temperature.

Running Period	Cell cross section	Holding field	ΔP_a^{se}
Hydrogen '97	29x9.8 mm	335 mT	3.3 %
Deuterium '00	21x8.9 mm	335 mT	0.3 %
Hydrogen '02	21x8.9 mm	297 mT	5.5 %

Table 3.2:
Target depolarization via spin exchange collisions for different running periods.

shown in section 3.5, this result can be extended to the whole target.
This measurement was first performed during the hydrogen '97 running period, resulting in a polarization loss $\Delta P_a^{se} \simeq 3.3\,\%$ [Bau00]. Due to the lower critical field, the deuterium spin exchange probability is roughly 20 times less than for hydrogen at the same working conditions. In 2000, this reduction was counterbalanced by a factor 1.8 because of the employment of the smaller target cell and the decrease of the working temperature from 100 to 60 K[38]. The resulting spin exchange depolarization contribution during the 2000 running period can therefore be quantified in $\Delta P_a^{se} \simeq 0.3\,\%$[39]. For the hydrogen tranverse running the rescaling with respect to 1997 has to take into account the different holding field strength (297 mT), the smaller cell (1.6 times increased density) and the lower ABS atomic flux[40]. The estimated polarization loss for this period is $\Delta P_a^{se} \simeq 5.5\,\%$. This result can be compared with a measurement taken in september 2002 and shown in figure 3.3: although affected by a polarimeter calibration problem causing the results for P_{z+} and P_{z-} to be asymmetric, the measurement shows an average depolarization of 5.8 %, not far from the predicted value. In table 3.2, the spin exchange contribution to the total target depolarization for the different running periods are summarized.

Bunch field induced resonant depolarization

As already explained in section 1.3, the elecromagnetic field produced by the HERA bunched electron beam can induce target resonant depolarization when the frequency of one of its high amplitude harmonics matches the frequency of one hyperfine transition. Since the energy difference between two states depends on the external magnetic field, the transitions occurr only for particular settings of the holding field. The transition probablility, depending on the states involved, is proportional to the square of the beam current. During the longitunal polarized running period (1996-2000), the potential presence of sufficiently separated π transitions allowed to set the target field to a working

[38] As a result of the lower temperature, the density increases but the mean relative velocity of the atoms decreases, so that the spin exchange probability is changed in two opposite directions.

[39] A direct measurement of such a small contribution was not possible of that time beacause of the not sufficient statistical precision of the polarimeter.

[40] Due to the larger "diameter" of the transverse magnet compared to the longidudinal one, the ABS had to be moved a few centimeters away from the injection tube, causing the atomic injected flux to drop by roughly 20 %.

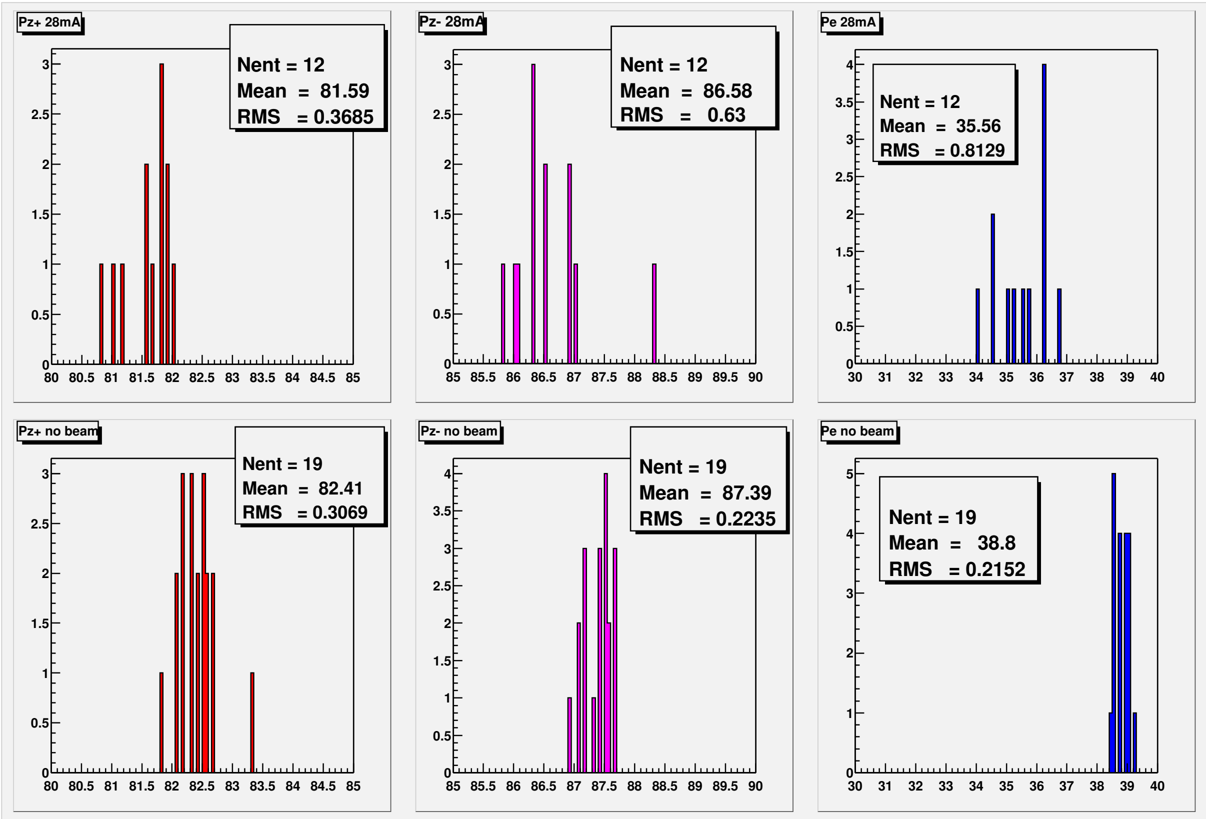

Figure 3.4: A measurement of the beam induced depolarization taken in November 2002. The upper plots show the polarization values for P_z+ (left), P_z- (center) and P_e- injected, with an electron beam current of 28 mA. The same measurements without beam are displayed in the lower plots. The resulting nuclear depolarization is $\Delta P_a^{BRP} = 0.8\,\%$ for both P_z+ and P_z-.

point (335 mT) where no beam induced depolarization could be observed. Due to the magnetic field orientation, the transverse polarized target operational since october 2001 soffers the occurence of densely spaced σ resonances. In this case, the identification of a field intensity for which beam resonant depolarization can be totaly avoided failed so far. Figure 3.4 shows two polarization measurements, one taken with electron beam at 28 mA and the second one just after the beam was dumped. The comparison between the two average results for either nuclear injected polarizations (P_z+ and P_z-) $\Delta P_a^{bd}|_{BRP} \simeq 0.8\,\%$. Taking into account the quadratic dependence on the beam current, a measured depolarization of about 2 % is expected for the upper limit of 45 mA of beam current. Although further studies are going on in order to improve the field quality (compare chapter 2), it is possible that the target polarization calculation for the transverse running will have to take into account also this additional spin relaxation process.

3.3.2 The injected atomic polarization

The injected polarization of each ABS operating mode (compare table 2.1) can be calculated if one knows the transmission probabilities of the sextupole system and the efficiencies of the used adiabatic transition units. As already written in section 2.1, the sextupole transmission probabilities for hydrogen and deuterium have been calculated using a montecarlo simulation and the results are displayed in table 2.2. The transition efficiencies can be extracted by measuring the magnetic field dependence of the spin relaxation processes and fitting the data with a theoretical model called *master equation* and described in [Bra95, Bau00].
From the HERMES data taking point of view, the important ABS injection modes are the (two hyperfine states) positive and negative nuclear polarization, P_z+ and P_z- respectively, and, in case of deuterium, the two additional positive and negative tensor polarization $P_{zz}+$ and $P_{zz}-$ (compare table 2.1).
For hydrogen, only the two appendix transitions (i.e. after the sextupole system) are used: the SFT 2-4 for P_z+ and WFT 1-3 for P_z-. Therefore, the injected polarizations are directly given by the transitions efficiencies[41], whose values have been calculated by Baumgarten using the mentioned technique and crosscheked using a more direct method based on the symmetry of the spin relaxation processes for the two injection modes.
In case of deuterium, several transition units are used to provide the four mentioned polarizations, some of them located between the two sextupole subsystems. Hence, the injected polarizations have to be calculated taking into account the transitions efficiencies as well as the transmission probabilities for atoms whose hyperfine state gets changed between the two subsystems.
The calculated injected polarizations for hydrogen and deuterium are summarized in table 3.3.

[41] As shown in table 2.1, the sextupole system is assumed to provide a 100 % elecron polarized atomic beam.

Mode	Hydrogen	Deuterium
P_{z+}	97.26 ± 0.05	87.78 ± 0.07
P_{z-}	-97.38 ± 0.07	-89.50 ± 0.10
P_{zz+}	-	96.22 ± 0.38
P_{zz-}	-	-177.30 ± 0.61

Table 3.3:
Estimated ABS injected polarization values for hydrogen and deuterium data taking modes. All values are given in percent. The quoted errors take only the uncertainty of the ABS efficiencies into account.

3.4 The molecular polarization β

As already explained in section 3.2.1, in the storage cell a certain amount of polarized hydrogen or deuterium atoms can recombine. A direct estimation of the remnant polarization contained in the so produced molecules is not possible at HERMES, as the Breit-Rabi polarimeter can measure the atomic polarization only[42].
The atomic recombination is a temperature dependent surface mediated process [Kol98, Bau00, Bau02d]. Hence, measurements of the nuclear polarization of recombined atoms performed using storage cell made of different material and/or with different coating [Vdb97, Wis01] are not directly applicable to the HERMES case.
So far, the lack of information about the molecular polarization has led to apply the conservative value $\beta = 0.5 \pm 0.5$, meaning, in case of relatively high recombination, a severe limitation of the average target polarization accuracy. Recently, a set of data taken in 1997 at warmer cell (260 K instead of the nominal 100 K) could be used to measure the hydrogen β value at that temperature with the help of the HERMES spectrometer. In the next chapter, it will be shown that the measured molecular polarization can by used as an upper limit for $\beta|_{100K}$. At the same time, some other considerations will be brought up which will allow to set an increased lower limit for β.

3.5 Sampling corrections

In section 3.1 it has been mentioned that the measured values α_r^{TGA} and P_a^{BRP} are connected to the target average atomic fraction α_r and atomic polarization P_a respectively, through the following relations:

$$\alpha_r = c_\alpha \cdot \alpha_r^{TGA} \tag{3.57}$$

$$P_a = c_P \cdot P_a^{BRP} \tag{3.58}$$

where c_α and c_P are called *sampling corrections.*
If the atomic recombination and nuclear depolarization probabilities per wall collision, γ_r and γ_z respectively, were constant all over the surface of the cell, the sampling corrections would depend only on the geometry of the beam and sample tube, as well as on the acceptance of the TGA and BRP. This is actually the case for a fresh installed cell, whose Drifilm coating is assumed to be intact and uniformly distributed. The validity of this scenario is typically preserved during normal running conditions, as no influence of the HERA beam on the target performance is observed. However, during certain limited periods of non optimal beam tune, or after an accidental beam loss near the HERMES target

[42] Using other measurement devices as the Lamb shift polarimeter (LSP) [Zel86, Lem93, Eng02], one can access the nuclear molecular polarization loosing, on the other hand, information about the hyperfine state populations, essential in the HERMES target.

region, sudden and sharp drops of α_r^{TGA} and P_e have been observed. At those times, the change of the target performance was associated to increased charged and/or synchrotron rates measured by the HERMES hodoscopes, as well as higher vacuum pressures. After such an event, α_r^{TGA} typically recovered within some ten hours of polarized running. This behavior can be explained by several mechanisms:

- radiation damage of the Drifilm coating by synchrotron light;
- removal of the ice layer on the storage cell by radio-frequency heating due to wake fields;
- ion bombardment of the storage cell walls;
- chemical reactions of ionized hydrogen radicals with the cell coating;
- contamination of the storage cell surface by sputtered material from collimator C_2[43].

Since the exact effect of the HERA beam on the surface properties is unknown, any possible distribution of recombination and wall relaxation probabilities has to be considered for a limitation of the sampling corrections. Nevertheless, following [Bau00] it is convenient to distinguish certain scenarios of special interest.

Homogeneous cell (HC): the natural assumption when the cell has not (yet) been exposed to the HERA beam. The resulting sampling corrections fix an upper limit for α_r (P_a) for any given values of α_r^{TGA} (P_a^{BRP}).

Homogeneous beam tube (HBT): the beam tube homogeneously affected by the beam, the side tubes unaffected.

Inhomogeneous beam tube (IBT): beam tube inhomogeneously affected by the beam, the side tubes unchanged. This scenario does not lead to a single sampling corrections, but it can be used to calculate a lower limit for α_r (P_a) at a given measured value α_r^{TGA} (P_a^{BRP}).

In all scenarios it is assumed for the recombination probabilities in the sample tube γ_r^{ST} and beam tube γ_r^{BT} that the relation $\gamma_r^{ST} \leq \gamma_r^{BT}$ holds at any time. The validity of this hypothesis is proven by the data, as it will by shown in the next chapter.
Numerical calculations of the sampling corrections for the big cell have been performed by Henoch using a molecular flow simulation [Hen02], and analytically by Baumgarten starting from the one-dimensional diffusion equation [Bau02a]. The sampling correction c_P has to be subdivided into two different terms, one for the wall collisions and a second

[43] Last electron beam collimator before the HERMES target cell.

one for spin exchange relaxation, as the two processes have to be treated in different ways. This can be done defining the depolarization factors $\pi_{wd} = 1 - \Delta P_a^{wd}$ (wall collisions) and $\pi_{se} = 1 - \Delta P_a^{se}$ (spin exchange relaxation) so that, for small amount of spin relaxation one has:

$$\begin{aligned} P_a &\simeq \pi_{wd}\,\pi_{se}\,P_a^{inj} \\ P_a^{BRP} &\simeq \pi_{wd}^{BRP}\,\pi_{se}^{BRP}\,P_a^{inj} \end{aligned} \tag{3.59}$$

As the spin exchange relaxation occurs in the gas phase, this process is not affected by any change of the cell surface properties, so that the relation between π_{se} and π_{se}^{BRP} has to be independent from any of the listed scenarios. Moreover, since calculations have shown that $\pi_{se} \simeq \pi_{se}^{BRP}$ [Bau00], one can conclude that the sampling correction c_P is determined by the wall depolarization only:

$$c_P = \frac{P_a}{P_a^{BRP}} \simeq \frac{\pi_{wd}}{\pi_{wd}^{BRP}} \tag{3.60}$$

The resulting sampling corrections for the three listed scenarios are given by[44]:

$$\textbf{HC:}\quad \alpha_r = \left(0.3665\,x + 0.63233\,x^2\right)^{\frac{1}{3}} \tag{3.61}$$

$$\textbf{HBT:}\quad \alpha_r = -0.054\,x + 1.836\,x^2 - 1.334\,x^3 + 0.55\,x^4 \tag{3.62}$$

$$\textbf{IBT:}\quad \alpha_r \geq x^2\left(\sqrt{2}(1 + \frac{1}{2}\varepsilon\,(1-x)) - (\sqrt{2}-1)\,x^2\right)^{-1} \tag{3.63}$$

$$\begin{aligned}\textbf{HC:}\quad \pi_{wd} = {} & 0.00463 - 0.36731\,y + 11.736\,y^2 - 35.374\,y^3 + 51.51\,y^4 \\ & -36.874\,y^5 + 10.365\,y^6\end{aligned} \tag{3.64}$$

$$\textbf{HBT:}\quad \pi_{wd} = 0.00123 - 0.054\,y + 2.577\,y^2 - 2.309\,y^3 + 0.78456\,y^4 \tag{3.65}$$

$$\textbf{IBT:}\quad \pi_{wd} \geq 2\,y^2\,\left(2 + \varepsilon\,(1-y)\right)^{-1} \tag{3.66}$$

where $x = \alpha_r^{TGA}$ and $y = \pi_{wd}^{BRP}$ respectively.
The factor ε is defined as the ratio of the sum of sample and injection tube conductances (C_{ST} and C_{IT}) to the conductance of half beam tube (C_{BT}):

$$\varepsilon = \frac{C_{ST} + C_{IT}}{C_{BT}}|_{bigger\ cell} = 0.55 \tag{3.67}$$

The sampling corrections (3.61) to (3.66) are shown in figure 3.5.
If none of the three scenarios can be identified from the data, one can not arbitrary choose one sampling correction. In such a case, the complete range between the scenario **HC** and **IBT** has to be considered. The value α_r is then given by the average of equations (3.61) and (3.63) and the systematic uncertainty by the half difference. This method of error estimation is very conservative.

[44]These relations are valid for the bigger cell only. Similar calculations can be performed in order to obtain the correpondent results for the smaller cell in use since 2000.

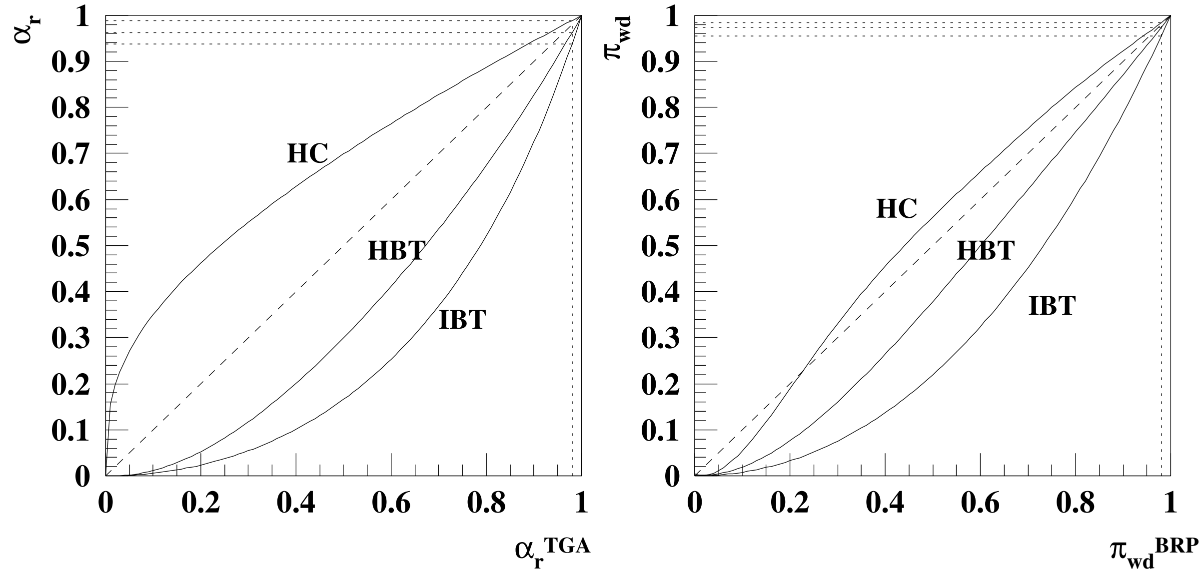

Figure 3.5: Left: Relations between α_r in the beam tube and the measured value α_r^{TGA} for a homogeneous storage cell **HC**, a homogeneous beam tube **HBT** and the lower limit of the inhomogeneous beam tube scenario **IBT** a for large storage cell. Right: The same relations for wall depolarization. The dotted lines represent examples of the corrections. For a measured value $\alpha_r^{TGA} = 0.98$, one obtains a value $\alpha_r \simeq 0.96 \pm 0.025$, while for $\pi_{wd}^{BRP} = 0.98$ one has $\pi_{wd} \simeq 0.97 \pm 0.013$. For low values of α_r^{TGA} and π_{wd}^{BRP}, the uncertainty becomes large, if none of the scenarios can be excluded by measurements.

As during data taking the measurements of α_r^{TGA} and π_{wd}^{BRP} are almost always well above 0.9, one may use linear approximations for the sampling corrections given by:

$$\alpha_r = \bar{a} + (1-\bar{a})\,\alpha_r^{TGA} = \alpha_r^{TGA} + \bar{a}\,(1-\alpha_r^{TGA}) \tag{3.68}$$

$$\pi_{wd} = \bar{b} + (1-\bar{b})\,\pi_{wd}^{BRP} = \pi_{wd}^{BRP} + \bar{b}\,(1-\pi_{wd}^{BRP}) \tag{3.69}$$

Linear Approx.	a	b
HC	0.443	0.225
HBT	-0.75	-1.138
IBT	-1.81	-0.29

	Larger Cell	Smaller Cell
$\bar{a}$	-0.683	-0.83
Δa	1.126	1.27
$\bar{b}$	-0.456	-0.55
Δb	0.681	0.77

Table 3.4: Left table: Values of the linear approximations a (c_α) and b (c_P) for the sampling corrections resulting from the three scenarios explained in the text. These figures have been calculated for the bigger cell geometry. Right table: average values and errors of the linear approximations for bigger (Baumgarten) and smaller (Henoch) cell geometries calculated considering the whole range between the **HC** and **IBT** scenario. These values have to be used when none of the existing models can be applied to the data.

Values of the parameters $\bar{a}$ and $\bar{b}$ and their errors Δa and Δb for both cell geometries as well as the linear approximations of the single scenarios for the bigger cell are listed in table 3.4.
As it can be noticed from the plots in figure 3.5, reasonably small errors on α_r and P_a can only be achieved if the values of α_r^{TGA} and π_{wd}^{BRP} are close to unity.

3.6 The determination of the target polarization P^T and its error

Now that all terms of the target polarization formula (3.6) have been discussed, one can put everything together and express P^T as function of measured quantities. In order to proceed, it is convenient to write the target polarization in the following way:

$$P^T = \alpha_0 \left(\alpha_r + (1-\alpha_r)\,\beta\right) P_a = \alpha_{tot} \cdot P_a \tag{3.70}$$

where the term $\alpha_{tot} = \alpha_0 \left(\alpha_r + (1-\alpha_r)\,\beta\right)$ is called *total* atomic fraction.

3.6.1 The total atomic fraction α_{tot}

Combining equations (3.70), (3.68), (3.12) and (3.47), α_{tot} can be expressed by

$$\alpha_{tot} = \frac{\phi_a + (\bar{a}\,(1-\beta)+\beta)(\phi_m - \phi_{bal} - \phi_{rg})}{\phi_a + \phi_m + (\sqrt{2}-1)\phi_{bal} + (2\sqrt{2}-1)\phi_{rg}} \tag{3.71}$$

The systematic uncertainty of α_{tot} is determined by the measured flowrates ϕ_a, ϕ_m, ϕ_{bal} and ϕ_{rg} and their errors as well as the values and uncertainties of β, $\bar{a}$ and the TGA calibration constant κ. With the matrix T defined by

$$T = \left(\frac{\partial \alpha_{tot}}{\partial \phi_i}, \ldots, \frac{\partial \alpha_{tot}}{\partial \kappa}\right) \tag{3.72}$$

and the diagonal covariance matrix C of all calibration costants, the systematic uncertainty $\Delta_{sys}\alpha_{tot}$ is given by

$$\Delta_{sys}\alpha_{tot} = \sqrt{TCT^T} \tag{3.73}$$

The matrix T contains 10 independent derivatives, i.e. for κ, the rest gas calibration constant c_{rg}, $\bar{a}$, β and the terms related to the ballistic flux calibration $\phi_a^{(1,2)}$, $\phi_m^{(1,2)}$ and $p_{tc}^{(1,2)}$[45]. The error source connected to last six values may be collected in a reduced

[45] This error calculation assumes that the ballistic flux calibration has been performed following the first method described in section 3.2.1 , which was actually the case till the end of the 2000 running period.

uncertainty $\tilde{\Delta}\phi_{bal}$ which does not take into account c_{rg}. The remaining derivatives can by calculated from the (3.71) by

$$\frac{\partial\alpha_{tot}}{\partial\kappa} = \left[(\bar{a}(1-\beta)+\beta-\alpha_{tot})\phi_r - \alpha_{tot}\sqrt{2}(2\phi_{rg}+\phi_{bal})\right]/(\kappa N) \tag{3.74}$$

$$\frac{\partial\alpha_{tot}}{\partial c_{rg}} = -\left[(\bar{a}(1-\beta)+\beta+(\sqrt{2}-1)\alpha_{tot})(p_{tc}+\frac{\partial\phi_{bal}}{\partial c_{rg}})+\alpha_{tot}\sqrt{2}p_{tc}\right]/N \tag{3.75}$$

$$\frac{\partial\alpha_{tot}}{\partial\bar{a}} = (1-\beta)\phi_r/N \tag{3.76}$$

$$\frac{\partial\alpha_{tot}}{\partial\beta} = (1-\bar{a})\phi_r/N \tag{3.77}$$

$$\frac{\partial\alpha_{tot}}{\partial\phi_{bal}} = -\left[\bar{a}(1-\beta)+\beta+(\sqrt{2}-1)\alpha_{tot}\right]/N \tag{3.78}$$

where $N = \phi_a + \phi_m + (\sqrt{2}-1)\phi_{bal} + (2\sqrt{2}-1)\phi_{rg}$ is the denominator of equation (3.71) and ϕ_r is given by (3.10).
The derivative $\frac{\partial\phi_{bal}}{\partial c_{rg}}$ and the value of $\tilde{\Delta}\phi_{bal}$ can be derived from equation (3.15):

$$\frac{\partial\phi_{bal}}{\partial c_{rg}} = -(\phi_a^{(1)}p_{tc}^{(2)} - \phi_a^{(2)}p_{tc}^{(1)})/(\phi_a^{(1)}-\phi_a^{(2)}) \tag{3.79}$$

$$\begin{aligned}\tilde{\Delta}\phi_{bal}^2 &= [(\phi_r^{(2)}\Delta\phi_a^{(1)})^2 + (\phi_r^{(1)}\Delta\phi_a^{(2)})^2 + (\phi_a^{(2)}\Delta\phi_m^{(1)})^2 + (\phi_a^{(1)}\Delta\phi_m^{(2)})^2 \\ &+ (\phi_a^{(2)}c_{rg}\Delta p_{tc}^{(1)})^2 + (\phi_a^{(1)}c_{rg}\Delta p_{tc}^{(2)})^2]/(\phi_a^{(1)}-\phi_a^{(2)})^2 \end{aligned} \tag{3.80}$$

3.6.2 The atomic polarization P_a

Combining equations (3.59) and (3.69), and using the approximation

$$\pi_{se}^{BRP} \simeq \frac{1}{1+\Delta(P_a^{se})^{BRP}} \tag{3.81}$$

the formula for the determination of the average atomic polarization P_a can be written in the following way

$$P_a = P_a^{BRP} + \bar{b}\,(\pi_{se}\,P^{inj} - P_a^{BRP}) \simeq P_a^{BRP} + \bar{b}\left(\frac{P^{inj}}{1+\Delta P_a^{se}} - P_a^{BRP}\right) \tag{3.82}$$

For the calculation of the systematic uncertainty $\Delta_{sys}\,P_a$, the important error sources that have to be included are Δb and $\Delta_{sys}\,P_a^{BRP}$[46]. As a result, one finds:

$$\Delta_{sys}\,P_a = \left((1-\bar{b})^2\,(\Delta_{sys}P_a^{BRP})^2 + (1-\pi_{wd})^2\pi_{se}^2(P^{inj})^2\Delta b^2\right)^{\frac{1}{2}} \tag{3.83}$$

During the analysis one tipically averages over a large dataset, so that the statistcal uncertainty of the polarization measurement $\Delta_{sta}\,P_a$ results very close to zero.

[46]The uncertainties on ΔP_{se} and on P_a^{inj} are negligible.

Chapter 4

Analysis of the Hydrogen Running Period in 1997

During the 1997 HERMES data taking period, the polarized target run with hydrogen. Kolster provided a preliminary evaluation of the target polarization for this dataset [Kol98]. Recently, significant improvements in the understanding and use of the sampling corrections (compare section 3.5) as well as the measurement of the polarization of recombined molecules led to the possibility of performing a new analysis with an enhanced estimation of the total uncertainty. In this chapter, the guidelines adopted during the analysis will be shown in details, devoting particular emphasis to the measurement of β. Finally, the average target polarization value together with its uncertainty will be given.

4.1 Overview of the dataset

Figure 4.1 shows the atomic fraction α^{TGA} measured by the target gas analyzer during the 1997 running period. The atomic nuclear polarization measured by the BRP is plotted in figure 4.2. Besides some startup problems, the target performance was relatively smooth. Unfortunately, a severe HERA beam loss close to the HERMES region occurred (first dashed line), resulting in a change of the cell surface properties. After this bad event, it was decided to collect a set of data at higher temperature ($T_{cell} = 260\,\mathrm{K}$ instead of the nominal value $T_{cell} = 100\,\mathrm{K}$), at the end of which the storage cell was exchanged (solid line). Also the second cell experienced a beam dump (second dashed line) which produced a small hole on its wall.

For these reasons, during the analysis the complete dataset has been divided into four periods during which the cell surface condition can be considered to remain unchanged. For each of them, particular studies have been performed in order to limit the the range of application of the sampling corrections and therefore the errors on α_r and P_a. This has allowed to take advantage of the data collected at high T_{cell} in order to extract the value

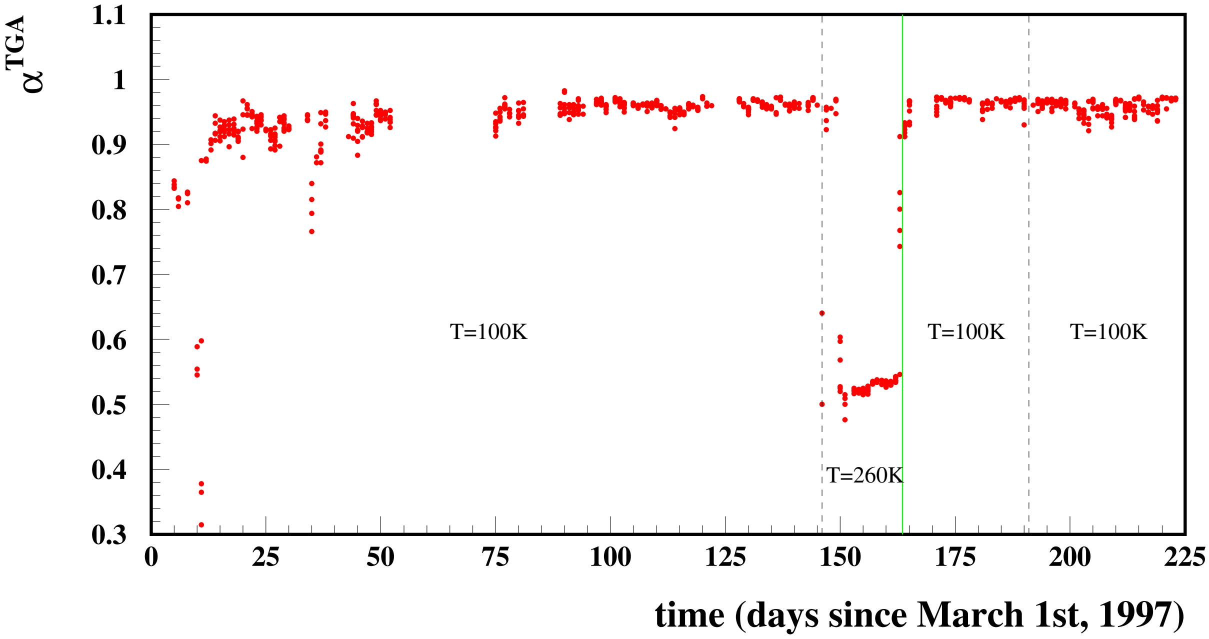

Figure 4.1: The target atomic fraction measured by the TGA over the entire 1997 HERMES polarized data taking period. The dashed lines indicate the occurrences of the two HERA beam losses. The solid line points out the time of the storage cell replacement. The running period at $T_{cell} = 260$ K can be clearly recognized due to the drop of the atomic fraction from $\alpha^{TGA} \simeq 0.95$ to $\alpha^{TGA} \simeq 0.55$. The lower dispersion of the data during the second half of the year is due to the optimization of the ratio of measurement time of mass 1 and mass 2. The data has been rebinned in bins of 2.5 hours each.

of the molecular polarization at that temperature, as explained in section 4.3.3.
The molecular ballistic flowrate ϕ_{bal} and the rest gas calibration constant c_{rg} have been extracted using the measurement techniques presented in section 3.2.1. They are shown in table 4.1 together with the TGA calibration constant κ. As all these values are not affected by any change of the cell surface properties, they can be considered to be valid overall the year.

Calibration constant	Value	Error
κ	0.551	0.026
ϕ_{bal} (KHz·mA^{-1})	0.595	0.297
c_{rg} (KHz·mA^{-1}·mbar^{-1})	$3.06 \cdot 10^6$	$1.53 \cdot 10^6$
p_{tc} (mbar)	$1.49 \cdot 10^{-7}$	$7.45 \cdot 10^{-8}$

Table 4.1:
TGA, ballistic flux and rest gas calibration constants for the hydrogen 1997 data taking period. The last row shows the average pressure in the target chamber. The presence of the unit mA in ballistic and rest gas constants is due to the TGA emission current normalization.

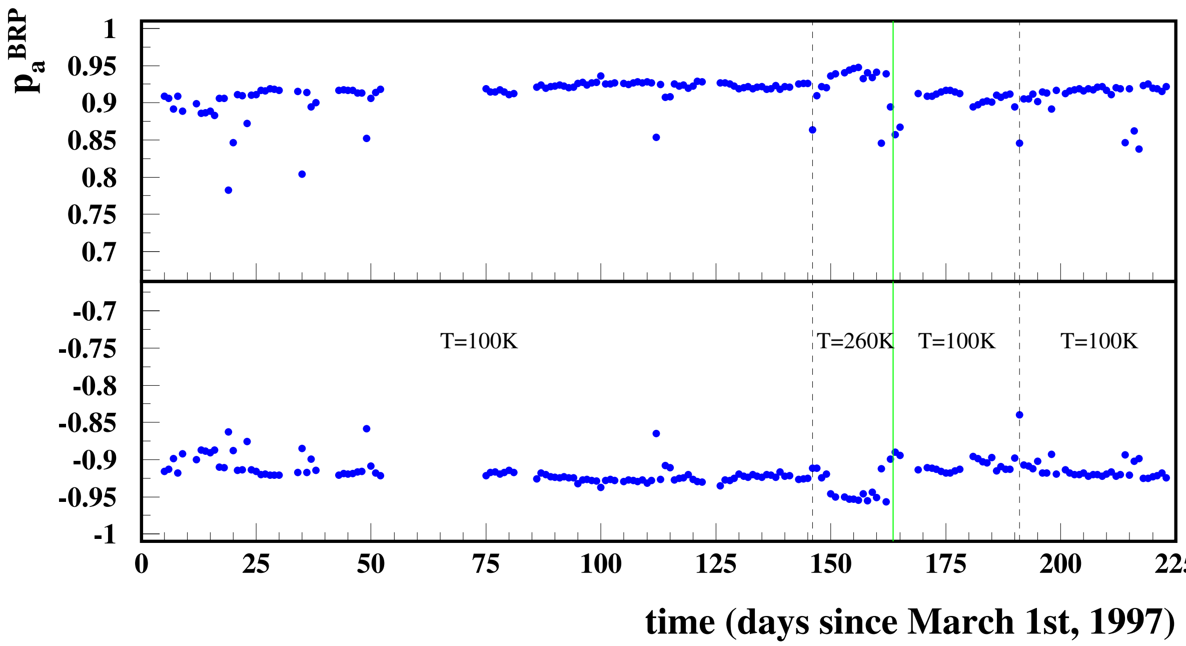

Figure 4.2: The target atomic nuclear polarization measured by the BRP over the entire 1997 HERMES data taking period. The plot is split in two parts to highlight the two ABS running modes *positive* (top) and *negative* injected nuclear polarization (see table 2.1). The higher value of P_a^{BRP} during the period at $T_{cell} = 260$ K is due to the reduced spin relaxation via spin exchange and wall collisions. The average measured polarization is above 90 %. The data has been rebinned in bins of 24 hours each.

4.2 Limitation of the sampling corrections and obtained results

As shown in the previous section, during the 1997 running period, the the cell surface properties have potentially changed three times, so that the whole dataset can be subdivided into four time ranges, for which the cell condition are assumed to remain constant. In section 3.5 it was shown that the range of application of the sampling corrections which are needed to relate the TGA and BRP measurement to the average target values is very wide if one does not have any information concerning the status of the cell surface. On the other hand, if one can prove the validity of one particular scenario, the sampling corrections could be restricted to that case, with a substantial reduction of the systematic error on α_r and P_a. In the following, the analysis of the cell surface and the consequent choice of the sampling corrections will be presented for each period along with the resulting values of P_a, α_r and α_0.

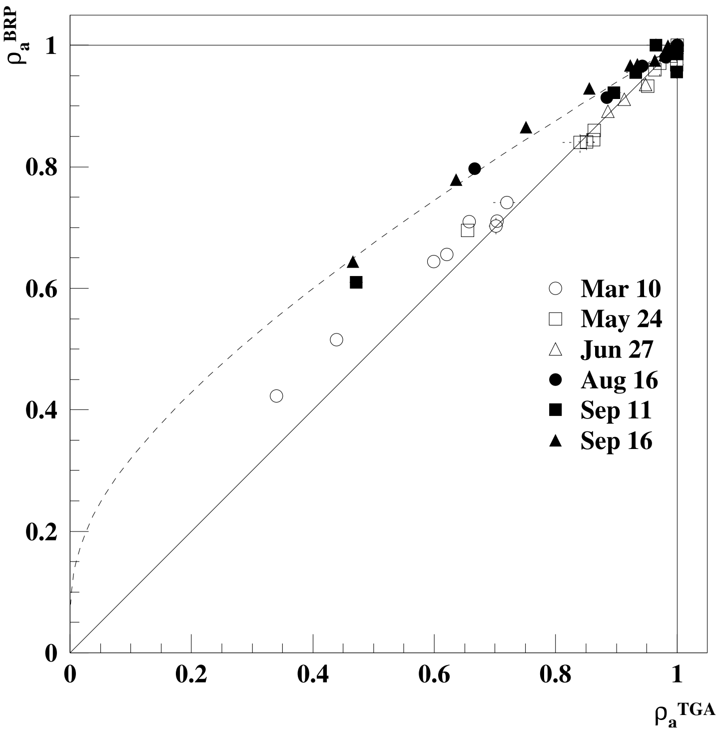

Figure 4.3:
Normalized atomic beam signals of BRP and TGA during measurement of the temperature dependence of the recombination process. Values of ρ_a^{BRP} and ρ_a^{TGA} close to 1 correspond to cell temperatures around the working point $T_{cell} = 100\,\mathrm{K}$. The solid line is the physical limit for $\gamma_r^{ST} \geq 0$, whereas the dashed line depicts the result of the montecarlo simulation for a homogeneous cell ($\gamma_r^{ST} = \gamma_r^{BT}$). Open marks represent results obtained with the first cell before the beam loss, while solid ones are related to the second cell.

4.2.1 First cell: from the startup to the beam dump

For this first period, two studies are available whose results provide a good test of the cell surface condition. The first analysis, concerning the atomic recombination, has been performed by Baumgarten [Bau00] and is represented in figure 4.3. The graph shows the normalized BRP atomic beam signal ρ_a^{BRP} plotted against the same quantity measured by the TGA ρ_a^{TGA} for several measurements of the temperature dependence of the recombination process (cell temperature scans). Due to the different detector acceptances, only the portion of atomic signal seen by the TGA can be lowered by the occurrence of recombination in the sample tube, so that this scenario can be highlighted by this comparison. In fact, if no recombination happens in the sample tube ($\gamma_r^{ST} \simeq 0$, where γ_r^{ST} is the recombination probability per wall collision in the s.t.) $\rho_a^{BRP} = \rho_a^{TGA}$ holds, whereas in case of not negligible recombination ($\gamma_r^{ST} > 0$) one should observe that $\rho_a^{BRP} > \rho_a^{TGA}$. In the plot, open marks represent measurements related to the first storage cell before the occurrence of the beam loss. For $\rho_a^{TGA} > 0.8$, corresponding to cell temperature values around the nominal one, the scenario $\gamma_r^{ST} \simeq 0$ is clearly proven. Hence, instead of using the homogeneous cell scenario given by eq. (3.61), the upper values of α_r can be limited for this fist period by eq. (3.32), with a significant reduction of the its potential range to:

$$\mathbf{IBT} \leq \alpha_r \leq \frac{\alpha_r^{TGA}}{\sqrt{2} - (\sqrt{2} - 1)\alpha_r^{TGA}} \tag{4.1}$$

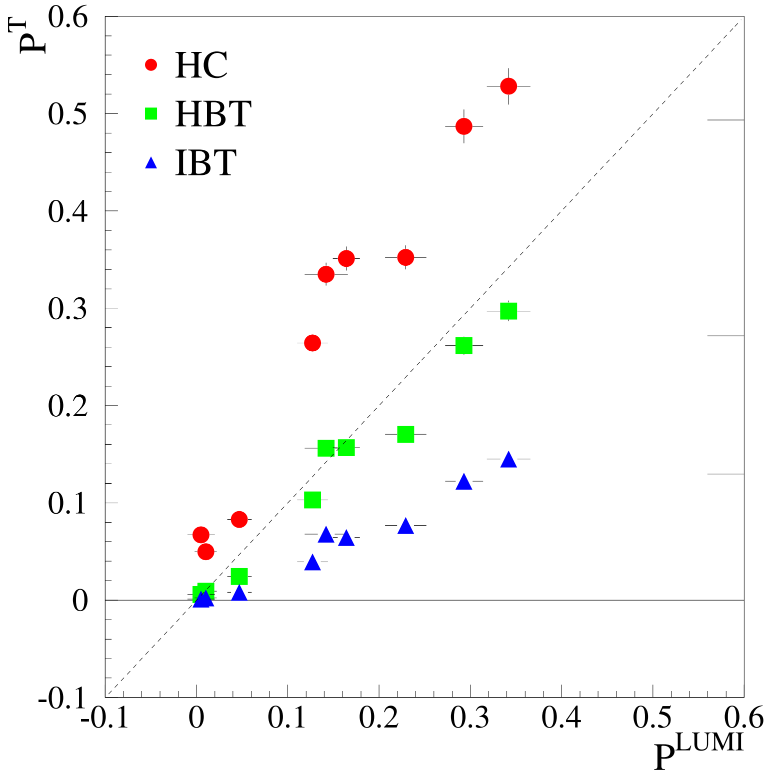

Figure 4.4:
Target electron polarization P^{LUMI} measured by the luminosity monitor during special *Bhabha* runs (x-axis) compared to the correspondent value P^T, calculated applying three different scenarios for the sampling correction c_P to the BRP and TGA measurements (y-axis). The diagonal dotted line represents the condition $P^{LUMI} = P^T$.

where **IBT** is the mathematical lower limit for α_r given by eq. (3.63). The value α_r is calculated as the central point of the interval (4.1) and the systematic uncertainty by the half difference of the two limits.

The sampling correction for the atomic polarization can be limited thanks to the measurement of the target electron polarization P^{LUMI} performed by the luminosity monitor during special runs when the ABS alternatively injected positive and negative P_e [Pot02] (see section 2.8). This can be done by comparing the results from the lumi detector with the target electron polarization calculated from the BRP and the TGA measurements[47]:

$$P^T = \alpha_0\, \alpha_r\, c_P\, P_a^{BRP} \tag{4.2}$$

By applying different sampling corrections c_P[48], one can check which cell surface scenario produces a result close to the condition

$$P^T = P^{LUMI} \tag{4.3}$$

In figure 4.4 values of P^T obtained applying the three different sampling corrections **HC**, **HBT** and **IBT** (compare eqq. (3.64), (3.65) and (3.66) respectively) are plotted against

[47]In eq. (4.2), the β term disappeared as the electron polarization of a molecule is equal to zero.

[48]The sampling correction c_α as been calculated has the central value of the entire range between the homogeneous cell and the inhomogeneous beam tube scenarios, as described in section 3.5

P^{LUMI}. For each model, the discrepancy $\bar{\delta}_{model}$ between the two results can be defined as

$$\bar{\delta}_{model} = \frac{1}{N-1}\sum_{i=1}^{N}\left(\frac{P^{T}_{model}(i) - P^{LUMI}(i)}{P^{lumi}}\right)^2 \tag{4.4}$$

where N is the total number of polarization measurements.
The analysis yields the results

$$\bar{\delta}_{HC} = 166\,\% \qquad \bar{\delta}_{HBT} = 8\,\% \qquad \bar{\delta}_{IBT} = 25\,\% \tag{4.5}$$

from which it is clear that the most reasonable scenario for the wall depolarization sampling correction is the homogeneous beam tube (compare section 3.5). One can therefore restrict around **HBT** the possible range of variation of the depolarization factor π_{wd} in the following way:

$$0.7\,(\mathbf{IBT}) + 0.3\,(\mathbf{HC}) < \pi_{wd} < 0.3\,(\mathbf{IBT}) + 0.3\,(\mathbf{HC}) \tag{4.6}$$

As usual, average value and error can be calculated as the central value and half difference of the whole interval.

4.2.2 First cell: high temperature data

After the beam loss on July the 28^{th}, the cell temperature was raised to 260 K in order to increase the atomic recombination. The aim was to collect a set of data useful for the measurement of the molecular polarization β. Unfortunately, as shown in section 3.5, at low α_r (strong recombination), the application of the entire range of the sampling corrections between the lower limit scenario (**IBT**) and the upper limit one (**HC**) delivers a not satisfactory estimation of the uncertainty. For example, at $\alpha_r^{TGA} = 0.55$ one would get $\alpha_r^{TGA} = 0.47 \pm 0.27$ corresponding to 57 % relative error. Hence, for this running period the identification of the cell surface condition is crucial.
The proper scenario for α_r can be found combining measurements performed by the TGA and by the luminosity monitor. Rewriting eq. (3.46) for the total target normalized density $\tilde{\rho}_t$, which includes molecular background sources from rest gas and ballistic flux, one can state the following relation between the (temperature normalized) density $\langle\, n\,\rangle_{norm}$ measured by the lumi (see section 2.8) and the total average atomic fraction $\alpha = \alpha_0\,\alpha_r$:

$$\langle\, n\,\rangle_{norm} \propto \tilde{\rho}_t = \frac{\sqrt{2}}{1+(\sqrt{2}-1)\alpha} \tag{4.7}$$

For two different cell temperature values, the relation between the correspondent lumi rates is then given by

$$\frac{\langle\, n\,\rangle^{(T_1)}_{norm}}{\langle\, n\,\rangle^{(T_2)}_{norm}} = \frac{(\sqrt{2}-1)\,\alpha^{(T_2)}}{(\sqrt{2}-1)\,\alpha^{(T_1)}} \tag{4.8}$$

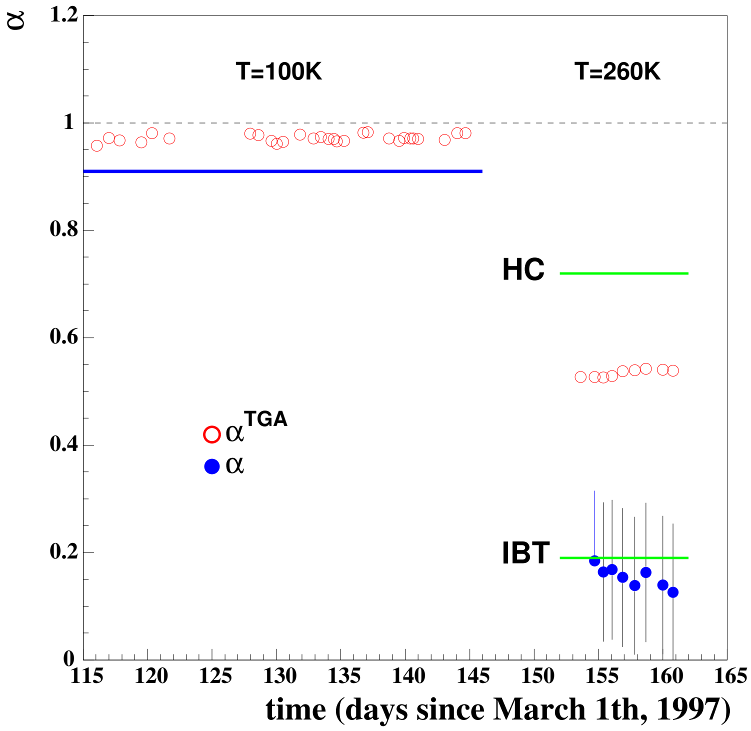

Figure 4.5:
The total atomic fraction α for the running period at $T_{cell} = 260\,\mathrm{K}$ (blue marks) calculated normalizing the correspondent value at $T_{cell} = 100\,\mathrm{K}$ to the density ratio between the two running periods. The results is compared with the average α_r values delivered by the application of the **HC** and **IBT** scenarios to α_r^{TGA}. The solid line in the left part of the plot represents the average value $\alpha^{100K} = 0.914$.

Hence α^{260K} can be extracted by comparing the lumi rates at $T_{cell} = 260\,\mathrm{K}$ with the ones measured at $T_{cell} = 100\,\mathrm{K}$ before the beam loss:

$$\alpha^{260K} = \frac{1}{\sqrt{2}-1}\left(\frac{\langle n\rangle^{100K}_{norm}}{\langle n\rangle^{260K}_{norm}}\left[(\sqrt{2}-1)\,\alpha^{100K}+1\right]-1\right) \tag{4.9}$$

where the average value of α^{100K} can be calculated for example during the first running period as described in the previous section.
Since α_0 is typically very close to one (compare table 4.2), eq. (4.9) provides a good estimation of α_r^{260}:

$$\alpha^{260K} = \alpha_0^{260K}\,\alpha_r^{260K} \simeq \alpha_r^{260K} \tag{4.10}$$

The resulting α^{260K} is shown in figure 4.5 [Mar02] along with the average values of α_r^{260K} delivered by the **IBT** and **HC** scenarios applied to α_r^{TGA}. The comparison points clearly out a substantial agreement between the measurement and the inhomogeneous beam tube model. As the **IBT** supplies a mathematical lower limit rather than a unique sampling correction, the range of variation of α_r has to be taken between **IBT** itself and the model next to it, namely **HBT**:

$$\mathbf{IBT} \le \alpha_r \le \mathbf{HBT} \tag{4.11}$$

As one can judge by looking at figure 3.5, the limitation of the systematic error on α_r resulting from this analysis is substantial.

For the spin relaxation, one has to take into account that, due to the lower density, at $T_{cell} = 260\,\mathrm{K}$ the strength of both spin exchange and wall depolarization is decreased compared to the nominal condition $T_{cell} = 100\,\mathrm{K}$.
The spin exchange effect can be estimated by scaling the reference value $\Delta P_{se}^{100K} = 3.3\,\%$ to the density ratio $\sqrt{\frac{100}{260}}$, resulting in $\Delta P_{se}^{100K} = 2.0\,\%$.
The relaxation due to wall depolarization is expressed by the depolarization factor P_{wd} which can be determined applying the sampling correction to the "measured" value P_{wd}^{BRP}.
The relations (3.64) to (3.66) have been determined assuming $\alpha \simeq 1$. At $T_{cell} = 260\,\mathrm{K}$, the strong recombination forces to redefine the range of variation for P_{wd} in the following way [Bau01]:

$$y \leq P_{wd} \leq \frac{2\,y^2}{2 + (2\,\alpha_r^{TGA}\,\varepsilon\,(1-y))/(2+\varepsilon\,(1-\alpha_r^{TGA}))} \tag{4.12}$$

where $y = P_{wd}^{BRP}$.

4.2.3 Second cell: before the beam dump

On August the 16^{th}, after the data taking period at $T_{cell} = 260\,\mathrm{K}$, the storage cell was exchanged. From this moment on, the condition of the surface can be considered to remain unchanged till the occurrence of the second beam loss on September the 8^{th}.
For this period, a good test of the cell surface useful for the limitation of α_r is given again by the measurements shown in figure 4.3. Indeed, the results concerning the second cell (solid marks) are in agreement with the homogeneous cell (**HC**) scenario represented by the dashed line. One can therefore restrict the α_r range in the following way:

$$a_{low}\,(\mathbf{HC}) \leq \alpha_r \leq a_{up}\,(\mathbf{HC}) \tag{4.13}$$

with the scaling factors $a_{low} = 0.97$ and $a_{up} = 1.03$ taking into account a $3\,\%$ systematic uncertainty.

On the other hand, no hints are available which can be used to limit the application of the wall depolarization sampling correction for this period. One has therefore to apply the entire range:

$$(\mathbf{IBT}) \leq P_{wd} \leq (\mathbf{HC}) \tag{4.14}$$

4.2.4 Second cell: after the beam dump

The second storage cell experienced a HERA beam loss on September the 8^{th} which, apparently, didn't seem to have changed its performance. Both pictures 4.1 and 4.3 would confirm this statement. Nevertheless, when the vacuum chamber was opened at the end of the data taking period, a 9 mm long, 3 mm wide hole was found on the cell wall. This additional opening may have modified the density distribution along the cell, not allowing to rely on the homogeneous cell hypothesis any longer. Therefore, for this period the calculation of both α_r and P_a has to be performed by applying the entire range of the sampling corrections between the (**IBT**) and (**HC**) scenarios.

4.2.5 Results of the four periods

The resulting average values of α_0, α_r and P_a for the four periods in which the 1997 data has been subdivided are shown in table 4.2 along with the measured TGA atomic and molecular flowrates.

During the three periods at $T_{cell} = 100\,\mathrm{K}$ the value of the nominal atomic fraction α_0 is, as expected, basically constant. The corresponding values of α_r change significantly, depending on the choice of the sampling corrections. Of particular interest is the difference between the first period, for which the inhomogeneous beam tube scenario holds, and the third one, characterized by the homogeneous cell model. On the other hand, the atomic polarization results to be not very sensitive to the different applied model. The different behavior between α_r and P_a can be understood if one compares the two graphs of figure 3.5.

During the period at $T_{cell} = 260\,\mathrm{K}$ the target is composed in large extent by recombined molecules ($\alpha_r = 0.26$); according to eq. (3.45), α_0 is slightly shifted toward higher values.

	1^{st} Cell, $T = 100\mathrm{K}$	1^{st} Cell, $T = 260\mathrm{K}$	2^{nd} Cell, $T = 100\mathrm{K}$	2^{nd} Cell*, $T = 100\mathrm{K}$
α^{TGA}	0.946 ± 0.037	0.530 ± 0.013	0.965 ± 0.010	0.957 ± 0.014
α_r^{TGA}	0.957 ± 0.037	0.536 ± 0.013	0.976 ± 0.011	0.969 ± 0.014
P_{z+}^{BRP}	0.918 ± 0.015	0.944 ± 0.030	0.911 ± 0.016	0.916 ± 0.023
P_{z-}^{BRP}	0.920 ± 0.015	0.951 ± 0.032	0.911 ± 0.016	0.918 ± 0.020
α_0	0.959 ± 0.029	0.969 ± 0.030	0.958 ± 0.029	0.960 ± 0.028
α_r	0.932 ± 0.044	0.260 ± 0.040	0.987 ± 0.033	0.960 ± 0.032
P_{z+}	0.908 ± 0.007	0.938 ± 0.016	0.893 ± 0.022	0.903 ± 0.020
P_{z-}	0.912 ± 0.007	0.940 ± 0.014	0.895 ± 0.021	0.906 ± 0.019

Table 4.2: Upper half: measured TGA and BRP values for the different periods of the 1997 data taking. The uncertainties are given by the rms of each dataset. Lower half: resulting average atomic fractions and atomic nuclear polarizations. The uncertainties of these values have been calculated with the method explained in section 3.6. The determination of α_r^{TGA}, α_r and α_0 involve the calibration constants shown in table 4.1.*During last period a hole was present on the storage cell wall.

4.3 The measurement of the nuclear polarization of recombined molecules

The measurement of the relative molecular polarization $\beta = P_m/P_a$ for the hydrogen target can be performed by taking advantage of the high T_{cell} dataset. Indeed, according to the average target polarization formula (3.6)

$$P^T = \alpha_0[\alpha_r + (1-\alpha_r)\beta]P_a \tag{4.15}$$

the sensitivity to measure β increases if the term $(1-\alpha_r)$ can be made large, i.e. for high recombination rate. As shown in table 4.2, this condition is actually fulfilled at $T_{cell} = 260\,\mathrm{K}$, where $(1-\alpha_r)^{260K} = 0.74 \pm 0.04$, while $(1-\alpha_r)^{100K} = 0.07 \pm 0.04$[49].
In this section, after a short introduction about the mechanisms involved in the recombination process inside the HERMES storage cell, the technique used to extract the value of β^{260K} is explained. An argumentation on how to use this result to limit the possible range of β^{100K} is eventually presented.

4.3.1 Atomic recombination in the HERMES storage cell

In a storage cell, atomic recombination can take place either in the gas phase (volume recombination) or on the wall (surface recombination). In the molecular flow regime of the HERMES target, the volume recombination is negligible.
Two mechanisms can be identified as potential responsible of the surface recombination:

- the Langmuir-Hinshelwood (**L-H**) process [Har81a, Har81b], where two adsorbed atoms thermalized with the storage cell wall react with each other;
- the Elay-Rideal (**E-R**) process [Hol94], where an atom impinging onto the surface from the gas phase reacts directly with an adsorbed atom..

Moreover, one has to consider that atoms sticking on the surface may be:

- chemisorbed atoms, characterized by a binding energy in the order of a few eV;
- physisorbed atoms (due to the Van-der-Waals interaction), with a binding energy between 10 and 100 meV.

The surface of a new storage cell is chemically saturated thanks to a Drifilm [Tho87, Cam86, Ste94, Gil93] coating, a hydrophobic silicon based polymer $(CH_3 - Si - O_3)$ of high radiation hardness. During beam operation, especially during periods of imperfect

[49] This value holds for the first storage cell employed in 1997. The temperature dependence of α_r is discussed in sec. 4.3.1

tune, the storage cell is exposed to synchrotron radiation, so that, within several weeks, the Drifilm coating gets damaged. If the cell is sufficiently cold ($T_{cell} < 140\,\mathrm{K}$), a layer of water, coming from the vacuum chamber rest gas and from the dissociator (see section (2.1)), coats the uncovered sites. The progressively growing water coverage is an important feature of the HERMES target, since water is known to inhibit hydrogen (or deuterium) recombination. The reason can be related to the fact that a hydrogen atom in water has a chemical binding energy of 5.16 eV, against an energy of 4.52 eV inside a hydrogen molecule [Lid98]. On the other hand, the bond strength of a hydrogen atom in a methyl group of Drifilm should be around 4.3 eV[50]. Hence, at low temperatures, the (exothermic) reaction of a hydrogen atom with Drifilm

$$H_1 + a - CH_3 \longrightarrow H_2 + a - CH_2 + Q \tag{4.16}$$

is favorite, while the (endothermic) process of recombination on water

$$H_1 + H_2O + Q \longrightarrow H_2 + OH \tag{4.17}$$

is suppressed.

The typical temperature dependence of recombination in the HERMES storage cell is shown in figure 4.6. The plot shows a minimum depolarization (high α_r^{TGA}) for temperatures between 70 and 100 K and constant monotonic decreases for higher and lower T_{cell} values. This behavior can be interpreted in the following way [Bau02d]:

[50] As the bond strength of a hydrogen atom in a methyl group of Drifilm is not exactly known, this value refers to the binding energy of $H - CH_2Si(CH_3)_3$

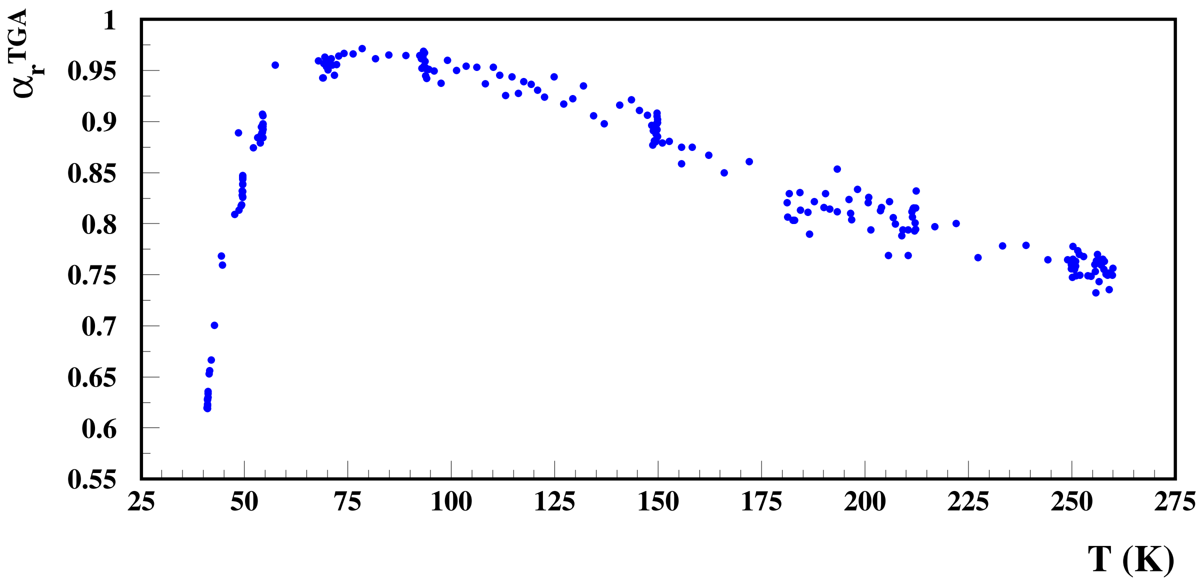

Figure 4.6: The temperature dependence of recombination as measured during a temperature scan of the second storage cell in use in 1997.

- The drop of α_r^{TGA} (increasing recombination) for $T_{cell} > 100\,\mathrm{K}$ can be explained assuming that in this temperature range the **E-R** mechanism dominates. In fact, as the kinetic energy of particles in gas phase is proportional to their temperature, at higher T_{cell} the probability, for a particle impinging onto the surface, to break the chemical bond of a sticking atom gets larger.

- The growing recombination for $T_{cell} < 70\,\mathrm{K}$ can be understood in terms of the **L-H** mechanism. At these temperature values, the sticking time τ_s of physisorbed particles (see eq. (3.51)) is sufficiently long so that atoms can diffuse on the cell surface and recombine. The recombination probability increases with τ_s and hence for falling temperatures.

The temperature range from 70 to 100 K represents the region of least probability for both mechanisms.

4.3.2 The extraction of β^{260K}

The method adopted to extract the molecular polarization benefits from the double spin asymmetry in the deep inelastic scattering of the longitudinally polarized HERA positron beam from the longitudinally polarized proton target, measured by the HERMES spectrometer[51] [Her93, Due95]. The asymmetry can be derived from the difference in the cross sections for antiparallel ($\overset{\rightarrow}{\Leftarrow}$) and parallel ($\overset{\rightarrow}{\Rightarrow}$) aligned positron and proton spins:

$$A_{||}^{meas} = \frac{\sigma^{\overset{\rightarrow}{\Leftarrow}} - \sigma^{\overset{\rightarrow}{\Rightarrow}}}{\sigma^{\overset{\rightarrow}{\Leftarrow}} + \sigma^{\overset{\rightarrow}{\Rightarrow}}} = \frac{1}{P_b P_T} \frac{(N/L)^{\overset{\rightarrow}{\Leftarrow}} - (N/L)^{\overset{\rightarrow}{\Rightarrow}}}{(N/L)^{\overset{\rightarrow}{\Leftarrow}} + (N/L)^{\overset{\rightarrow}{\Rightarrow}}} \tag{4.18}$$

where N denotes the number of events per spin state corrected for the background arising from charge symmetric processes and L is the corresponding luminosity. P_b (P_T) is the beam (target) polarization.
Since the cross section asymmetry is nearly independent from the experimental conditions, $A_{||}$ has to be the same, no matter what the storage cell temperature is. This leads to:

$$\frac{C_{||}^{100K}}{P_T^{100K}} = \frac{C_{||}^{260K}}{P_T^{260K}} \tag{4.19}$$

where $C_{||}$ indicates the quantity:

$$C_{||} = \frac{1}{P_b} \frac{(N/L)^{\overset{\rightarrow}{\Leftarrow}} - (N/L)^{\overset{\rightarrow}{\Rightarrow}}}{(N/L)^{\overset{\rightarrow}{\Leftarrow}} + (N/L)^{\overset{\rightarrow}{\Rightarrow}}} \tag{4.20}$$

[51] An overview of the HERMES spectrometer is given in appendix B.

and P_T^{100K} (P_T^{260K}) is the target polarization at $T_{cell} = 100\,\mathrm{K}$ ($T_{cell} = 260\,\mathrm{K}$) which, by using eq. (4.15), can be expressed by:

$$P_T^{100K} = \alpha_0^{100K}[\alpha_r^{100K} + (1-\alpha_r^{100K})\beta^{100K}]P_a^{100K} \tag{4.21}$$
$$P_T^{260K} = \alpha_0^{260K}[\alpha_r^{260K} + (1-\alpha_r^{260K})\beta^{260K}]P_a^{260K} \tag{4.22}$$

The values for $\alpha_0^{100,200K}$, $\alpha_r^{100,200K}$, $P_a^{100,200K}$ come from the analysis of the two periods, at low and high temperature respectively, when the first cell was in (first and second column of table 4.2).
As the surface conditions at 100 K and 260 K are different, β^{100K} and β^{260K} may be considered to be independent, so that two unknowns are present in equation (4.19).
The discrepancy between the values of the asymmetry measured in the two different experimental conditions can be expressed by the following function $F(\beta)$:

$$F(\beta) = \sum_{bins}\left[\frac{\frac{C_{||}^{260K}}{P_T^{260K}(\beta^{260K})} - \frac{C_{||}^{100K}}{P_T^{100K}(\beta^{100K})}}{\left((\delta_{C||}^{260K})^2 + (\delta_{C||}^{100K})^2\right)^{1/2}}\right]^2 \tag{4.23}$$

where the sum goes over the number of kinematic bins of the asymmetry measurement and $\delta_{C||}$ is the statistical uncertainty of each bin.
β^{260K} has been determined by adjusting its value until the function $F(\beta)$ was minimized. The minimization has been studied as function of the parameter β^{100K} and the result is represented in figure 4.7 [Sto02]. The plot shows that the assumptions taken for β^{100K} have low impact on the result for β^{260K}.
The following value has been extracted for β^{260K} taking the simple average of the values obtained by using $\beta^{100K} = 0$ and $\beta^{100K} = 1$:

$$\beta^{260K} = 0.68 \pm 0.09_{stat} \pm 0.06_{syst} \tag{4.24}$$

The statistical error was calculated by enlarging the minimum of $F(\beta)$ by one unit and was found to be rather independent from the choice of β^{100K}. The uncertainty of the present measurement is dominated by the low statistics of the data taken at 260 K (190'000 DIS candidates) compared to the 100 K data sample (2.5 Million events). The main source of the systematic uncertainty arises from the uncertainty in the sampling corrections for α_r^{100K} at small β^{100K} values and for α_r^{260K} at high β^{100K} values. An additional contribution, independent on the choice of β^{100K}, derives from the poorer knowledge of the sampling corrections of the BRP measurement at high cell temperatures. Other uncertainties common to both the 100 K and the 260 K measurements, like the uncertainty in α_0, do cancel. The stability of the result has been investigated by varying target data quality criteria and by varying the number of kinematic bins considered in eq. (4.23): no systematic effect could be detected beyond the statistical accuracy.

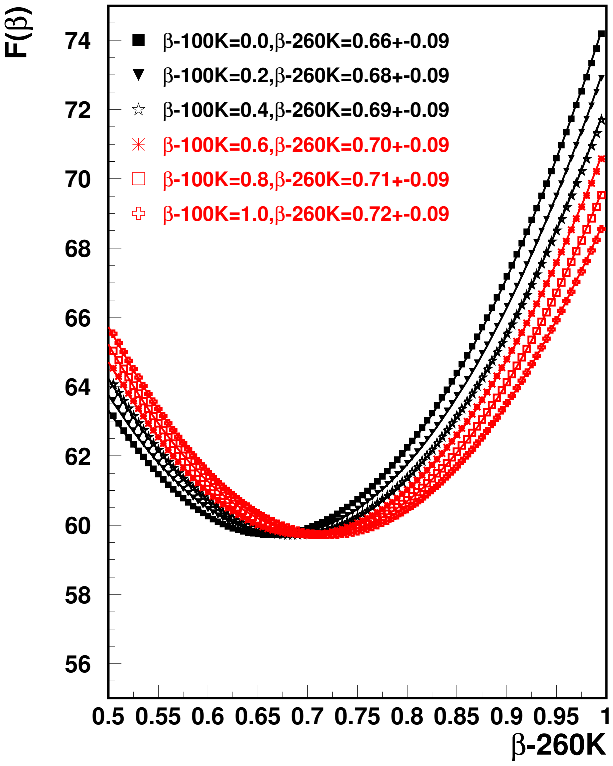

Figure 4.7:
$F(\beta)$ as a function of β^{260K} for fixed values of β^{100K} in the allowed range $0 \leq \beta \leq 1$. The values of β^{260K} for which $F(\beta)$ is minimized vary between 0.66 and 0.72 depending on β^{100K}. The statistical error is basically independent on β^{100K}.

Recalling the considerations of section 4.3.1, one can state that, under the experimental conditions in which the measurement has been performed, the recombination process can be described by the the Eley-Rideal mechanism in which an atom coming from the volume hits a chemically bound atom on the surface with enough kinetic energy to overcome the activation barrier. Assuming that the nucleon spins are not affected by the recombination process, the nuclear polarization of the molecule at its formation (P_m^0) can be evaluated by taking the average value of the polarization of the atom coming from the volume (P_a) and of the one sitting on the surface (P_s):

$$P_m^0 = \frac{P_a + P_s}{2} \tag{4.25}$$

The loss of polarization of the molecule after recombination has been well described in [Wis01]. In free flight, the internal molecular fields B_c from the spin rotation interaction and the direct dipole-dipole interaction, cause the nuclei to rapidly precess around a direction which is skewed to the external field by B_c/B. The orientation of B_c is randomized at each wall collision. Between successive wall collisions, the component of the polarization along the external field decreases by an amount $(B_c/B)^2$ and after n wall bounces:

$$P_m = P_m^0 e^{-n(B_c/B)^2} \tag{4.26}$$

where $B_c = 6.1\,\mathrm{mT}$ for H_2.
For the HERMES cell, $n \simeq 300$ [Bau02a] and $B \simeq 335\,\mathrm{mT}$ so that from the eq. (4.26) one

has:

$$P_m \simeq 0.9 P_m^0 \tag{4.27}$$

From the extracted value of β^{260K} and making use of eq. (4.25) and of the value for P_a^{260K} (see Table 4.2), one can give an estimation of the residual polarization of atoms on the surface:

$$P_s^{260K} = \left(\frac{2\,\beta^{260K}}{0.9} - 1\right) P_a^{260K} = 0.48 \pm 0.22 \tag{4.28}$$

4.3.3 The estimation of β^{100K}

The studies presented in section 4.3.1 prove that the recombination process at $T_{cell} = 100\,\mathrm{K}$ and $T_{cell} = 260\,\mathrm{K}$ is the same. The effect has been described in terms of the **E-R** mechanism, where an atom impinging onto the surface from the gas phase reacts directly with an adsorbed atom. This observation can be exploited in order to allow a restricted range for β^{100K}, as shown by the following argumentations.
Assuming that the nuclear spin state of the impinging atom is not affected by recombination, the theoretical lower limit for β^{100K}:

$$\beta_{low}^{100K} = \frac{P_m^{(100K,low)}}{P_a^{100K}} = \frac{0.9\,P_m^{0\,(100K,low)}}{P_a^{100K}} = \frac{0.9\,(P_a^{100K} + P_s^{100K,low})}{2\,P_a^{100K}} \tag{4.29}$$

can be found supposing that atoms sticking on the cell surface are completely depolarized ($P_s^{100K,low} = 0$). In such a case, for an average atomic polarization $P_a^{100K} = 0.90$ (see table 4.2) one has:

$$\beta_{low}^{100K} = 0.45 \tag{4.30}$$

On the other side, an upper limit for β^{100K} can be fixed by taking advantage of the measurement of β^{260K}. This requires a comparison between the cell surface conditions at the two working temperatures.

- at $T_{cell} = 100\,\mathrm{K}$, an (aged) cell is additionally covered by water.
- at $T_{cell} = 100\,\mathrm{K}$, the recombination probability per site is smaller compared to $T_{cell} = 260\,\mathrm{K}$, because of the decreased kinetic energy of atoms impinging onto the cell wall.

In section 4.3.1, it has been demonstrated that the water “fixes” the Drifilm coating damaged by the beam, without changing the recombination mechanism (recombination is not catalyzed by water). Hence, the presence of water does not have any effect on the polarization of recombined molecules.
On the other hand, at 100 K, the smaller recombination probability implies a larger residence time of chemically adsorbed atoms on the cell surface than at 260 K, so that the

potential nuclear depolarization increases accordingly.
In conclusion, the molecular polarization at $T_{cell} = 100\,\mathrm{K}$ can not be larger than the measured value at $T_{cell} = 260\,\mathrm{K}$:

$$\beta_{up}^{100K} = \beta^{260K} \tag{4.31}$$

Hence, the range of β^{100K} can be limited to

$$0.45 \leq \beta^{100K} \leq 0.83 \tag{4.32}$$

which takes into account the linear propagation of the statistical and systematic errors of β^{260}.
The final value and error of β^{100K} can be calculated as the average between the two limits in 4.33 and the half difference respectively:

$$\beta^{100K} = 0.64 \pm 0.19 \tag{4.33}$$

4.4 The target average polarization in 1997

With the estimation of β^{100K}, the knowledge of all terms needed for the calculation of the target polarization for the 1997 hydrogen running period is complete. The calculation of P^T for the three periods at $T_{cell} = 100\,\mathrm{K}$ has delivered the values shown in table 4.3 along with the average overall the high temperature data taking period. In is interesting to observe that, due to considerably large value (and small error) which has been applied to β, although the amount of recombined molecules change significantly for different periods, the total target polarization (and error) does remain substantially uniform. Due to the completely symmetric running conditions, the results for positive and negative injected nuclear polarization can be combined in a single value. The final average result for the low temperature data taking is

$$P^T = 0.852 \pm 0.033 \tag{4.34}$$

with a total relative error of 3.9 %.

	1^{st} Cell	2^{nd} Cell	2^{nd} Cell (with hole)	Average
P_+^T	0.850 ± 0.033	0.851 ± 0.036	0.854 ± 0.032	0.851 ± 0.033
P_-^T	0.853 ± 0.033	0.853 ± 0.036	0.857 ± 0.033	0.854 ± 0.033
P^T	0.851 ± 0.033	0.852 ± 0.036	0.856 ± 0.033	0.852 ± 0.033

Table 4.3: Target average nuclear polarization for the 1997 hydrogen running period. The first two rows show the results for positive and negative injected polarization. In the last row, the average results are presented.

Chapter 5

Analysis of the Deuterium Running Period in 2000

During the HERMES data taking period from January to September 2000, the polarized target run with deuterium. This period has been characterized by unprecedented running conditions in terms of stability of all target components as well as of the HERA beam tune. As it will be shown along the chapter, the absolutely smooth performance of the atomic beam source and the constant quality of the cell surface allow to treat the whole dataset as uniform from the point of view of the calculation of the target nuclear polarization.

5.1 Overview of the dataset

Over the eight months long deuterium running in 2000, the HERMES target presented very stable conditions. The atomic beam source, equipped with a recently developed microwave dissociator [Koc98], experienced only one major failure which hardly affected the data taking. Neither the scattering chamber, nor the TGA/BRP vacuum system had to be open, leading to constant amounts of residual gas in the storage cell as well as changeless efficiencies of the detectors. The storage cell had no need to be replaced, as its performance in terms of atomic recombination and nuclear depolarization was always excellent. The reason of such a good behavior can be found both in a particularly fortunate Drifilm coating and in the limited damage caused by the very well tuned electron/positron beam. After the single beam loss occurred in the vicinity of the HERMES experiment, the scarcely dropped measured atomic fraction recovered within several hours of polarized running.
The outstanding performance of the HERMES target in this period is well represented in figure 5.1, showing the values of nuclear polarization measured during data taking. In the period between January and June, the target was operated in order to inject positive and negative nuclear polarization (P_z+ and P_z- respectively), allowing a precise measurement

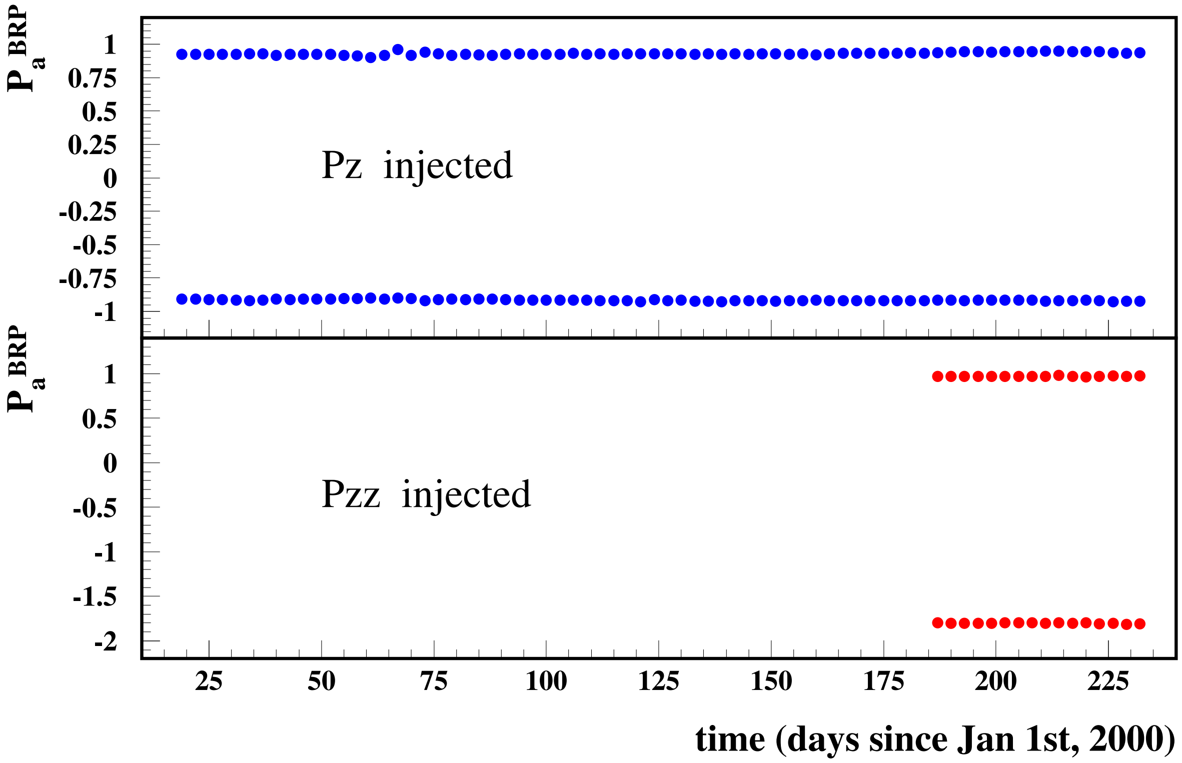

Figure 5.1: The atomic nuclear and tensor polarization measured by the BRP during the 2000 running period. The data has been rebinned in bins of 72 hours each. The positive and negative nuclear polarization (upper plot) was injected overall the data taking period. The bin averaged values are constantly above 0.9. The tensor polarization (lower plot) was employed from July on. Also during this injection mode the target performance was absolutely smooth.

of the deuterium spin structure function g_1^d [Len02]. From July on, a new injection mode combining nuclear and tensor polarization P_z+, P_z-, $P_{zz}+$ and $P_{zz}-$[52], was established in order to perform the first measurement of the tensor-polarized structure function b_1^d [Con02].

The constant behavior of the cell surface in terms of atomic recombination is demonstrated in figure 5.2, where the atomic fraction measured by the target gas analyzer is plotted overall the year.

5.2 The atomic polarization P_a

As discussed in section 3.3.1, the target average atomic polarization is determined by the performance of the ABS, defining the injected polarization P_a^{inj}, and by the spin relaxation which can happen inside the storage cell. A comparison between the hydrogen and deuterium target leads to the following considerations:

[52] The hyperfine states corresponding to each injected polarization are shown in table 5.1

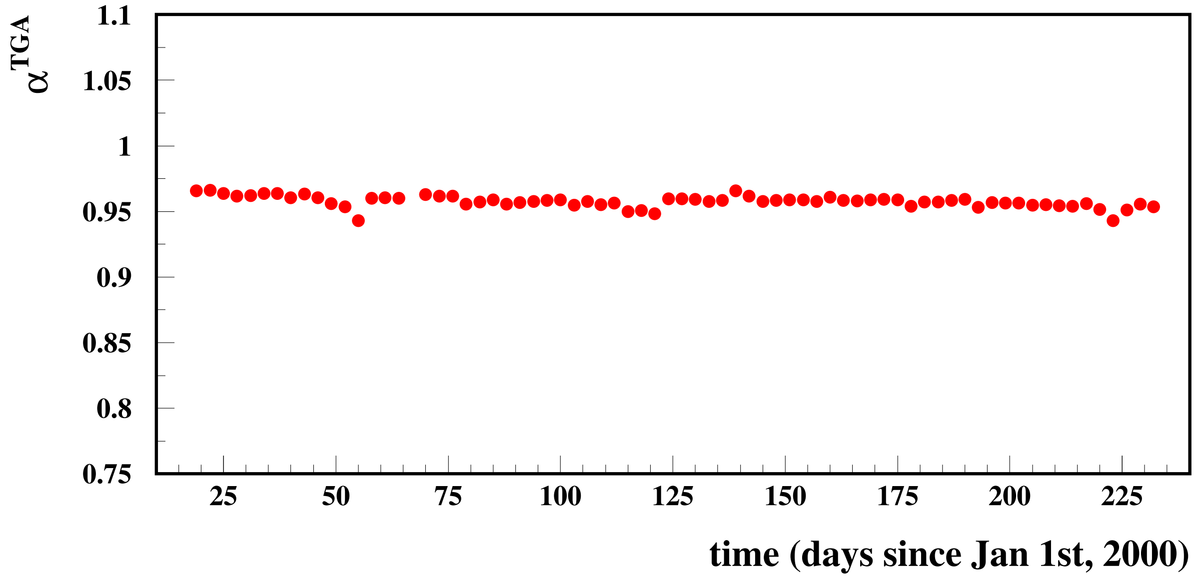

Figure 5.2: The atomic fraction measured by the TGA over the 2000 running period. The plot shows a very stable behavior, with the only exception of the beam loss experienced around the 55th day of data taking. The data has been rebinned in bins of 72 hours each.

- The degree of nuclear polarization injected by the ABS when running with deuterium is substantially lower than for hydrogen (see section 3.3.2). The reason is that, due to the larger set of hyperfine states, the deuterium nuclear polarization can only be achieved by using the transition units located between the two magnetic subsystems, with a consequent decrease of the total injection efficiency (compare section 2.1).

- For equivalent running conditions, in case of deuterium the spin exchange and wall relaxation processes are suppressed by a factor $(B_C^H/B_C^D)^2 \simeq 20$ compared to hydrogen.

The first item suggests that, differently from hydrogen[53], it is likely that the ABS performance in terms of injected positive and negative nuclear polarization results to be asymmetric, due to the several different efficiencies involved.
The second point is of particular interest, because if one could prove that no wall depolarization occurs in the storage cell, or at least that the amount of spin relaxation due to wall collisions is smaller than the statistical uncertainty of the polarimeter, than atomic polarization would match the BRP measurement, without any need of sampling corrections. This condition was actually fulfilled during the deuterium run in 2000, as it will be shown in the following.
The occurrence of wall depolarization can be revealed by exploiting its temperature dependence. Indeed, as explained in section 3.3.1, the probability of nuclear spin relaxation

[53]For hydrogen, the two operation modes P_z+ and P_z- provide the same amount of injected polarization because the efficiency of the two employed transition units is the same.

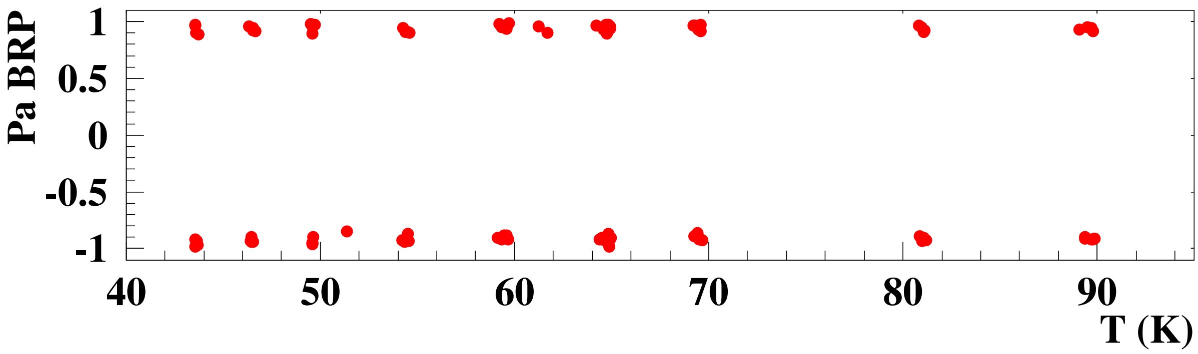

Figure 5.3: Nuclear vector polarization P_z as function of the cell temperature T measured in August 2000. No dependence on the temperature can be observed.

γ_z is proportional to the square of the sticking time $\tau_s = \tau_0\, e^{\left(\frac{E_b}{kT}\right)}$ of the atom on the cell wall, where T represents the temperature of the surface (see eq 3.51). Hence, for a given temperature range ΔT, the occurrence of a non-zero probability $\gamma_z > 0$ can be demonstrated by the measurement of a variation ΔP_z of the nuclear polarization. During the whole running period in 2000, no such a dependence has ever been observed at any reachable temperature value, as represented in figure 5.3, showing the results of a scan performed in August 2000. As a consequence, for the deuterium target the sampling correction for nuclear depolarization equals unity ($c_P = 1$), so that:

$$P_a = P_a^{BRP} \tag{5.1}$$

The complete set of atomic polarization values measured during data taking and averaged over the entire running period are shown in table 5.1.
Moreover, it is worth mentioning that the depolarization due to spin exchange collision

Inj. Mode	Inj. States	P_e	P_z	P_{zz}
P_z+	$\|1\rangle + \|6\rangle$	$+0.0038 \pm 0.0093$	$\mathbf{+0.927 \pm 0.017}$	$+0.871 \pm 0.011$
P_z-	$\|3\rangle + \|4\rangle$	$+0.0040 \pm 0.0100$	$\mathbf{-0.915 \pm 0.010}$	$+0.929 \pm 0.012$
$P_{zz}+$	$\|3\rangle + \|6\rangle$	-0.0028 ± 0.0020	-0.011 ± 0.003	$\mathbf{+0.971 \pm 0.010}$
$P_{zz}-$	$\|2\rangle + \|5\rangle$	$+0.0046 \pm 0.0034$	-0.011 ± 0.005	$\mathbf{-1.803 \pm 0.014}$

Table 5.1: Average values of atomic polarization P_a (distinguished in electron, nuclear vector and tensor polarization, P_e, P_z and P_{zz} respectively) achieved in 2000 during data taking, i.e. for nuclear and tensor injected polarization. The values plotted in figure 5.1 are shown in bold font. The uncertainties are calculated as the average systematic error of the single measurements. The fact that the (relative) systematic error depends on the injected state is a result of the different efficiencies of the BRP transition units (see section 2.7).

for this period has been calculated in section 3.3.1, resulting in a value $\Delta P_a^{se} = 0.3\,\%$ (see table 3.2). As a consequence of the negligible total amount of spin relaxation, the polarization injected by the ABS equals in 2000 the measured BRP value:

$$P_a^{inj} \simeq P_a^{BRP} \tag{5.2}$$

5.3 The atomic fraction α_{tot}

Besides the atomic polarization P_a, three more terms, α_0, α_r and β, enter in the target polarization formula 3.6. These quantities can be collected in the so-called total atomic fraction

$$\alpha_{tot} = \alpha_0\,(\alpha_r + (1-\alpha_r)\,\beta) \tag{5.3}$$

introduced in section 3.6.

For the deuterium target no estimation of the polarization of recombined molecules was possible, so that β has to be allowed to take any physically meaningful value ($\beta = 0.5 \pm 0.5$)[54].

Fortunately, it can be shown that during the deuterium data taking period in 2000 very low, if not any at all, atomic recombination occurred in the storage cell, so that both the sampling correction c_α and the impact of the uncertainty on β result to be negligible. There are two arguments that can be brought up in order to support this statement:

[54] The argument which leads to a lower limit for β^{100K} in case of hydrogen does not apply for the deuterium running because of the different working temperature $T_{cell} = 60\,\mathrm{K}$

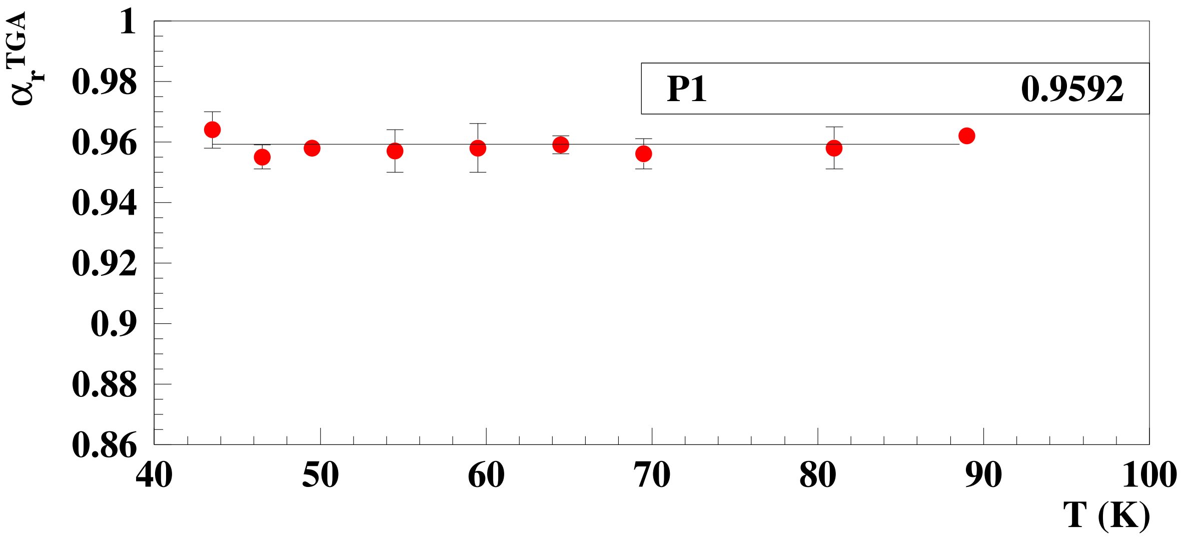

Figure 5.4: Measured atomic fraction as function of the cell temperature for $T_{cell} < 100\,\mathrm{K}$. No dependence on the temperature can be seen. The working point during data taking was set to $T_{cell} = 60\,\mathrm{K}$.

flowrate		Atomic Fraction	
ϕ_a	39.89 ± 3.52	α^{TGA}	0.958 ± 0.012
ϕ_m	1.73 ± 0.65	α_r^{TGA}	0.997 ± 0.014
ϕ_{ball}	0.77 ± 0.14	α_r	0.997 ± 0.015
ϕ_{rg}	0.84 ± 0.15	α_0	0.919 ± 0.022
		α_{tot}	0.918 ± 0.026

Calib. Const. & other Param.	
$\bar{a}$	-0.83 ± 1.27
β	0.5 ± 0.5
κ	0.860 ± 0.025
c_{rg}	$8.62 \cdot 10^6 \pm 1.06 \cdot 10^5$
p_{tc}	$0.97 \cdot 10^{-7} \pm 0.01 \cdot 10^{-7}$

Table 5.2: The left table shows the measured average TGA flowrates (all units are in kHz/mA) and the calculated atomic fractions for the deuterium running period in 2000. The right table lists the sampling correction $\bar{a}$ valid for the storage cell in use in 2000, the molecular polarization β, the TGA (κ) and rest gas (c_{rg} in KHz·mA^{-1}·mbar^{-1}) calibration constants and the average target chamber pressure (p_{tc} in mbar).

- Although the atomic recombination is a strongly temperature dependent process, no variation of the measured atomic fraction α^{TGA} in a very wide rage around the working point $T_{cell} = 60\,\mathrm{K}$ was ever observed during the whole year. This can be seen, among the other, during the cell temperature scan performed in August and represented in figure 5.4. It is interesting to compare this result with the total different one obtained with hydrogen in 1997 and shown in figure 4.6.

- The measurement of the fraction of atoms surviving recombination, α_r^{TGA}, performed thanks to the results coming from the target calibrations (compare section 3.2.1) provides the following average value:
$$\alpha_r^{TGA} = 0.997 \pm 0.014 \tag{5.4}$$
proving the absence of recombined molecules.

The final average value $\alpha_{tot} = 0.918 \pm 0.024$ was calculated for this period. In table 5.2 all the terms involved in the evaluation of α_{tot} are presented.

5.4 Results

The value obtained for α_{tot} and the measured atomic polarizations presented in table 5.1 can now be used to calculate the average target polarization in 2000. The results are:

$$\begin{aligned} P_z^T+ &= +0.851 \pm 0.029 \qquad (3.4\,\%) \\ P_z^T- &= -0.840 \pm 0.026 \qquad (3.0\,\%) \\ P_{zz}^T+ &= +0.891 \pm 0.027 \qquad (3.0\,\%) \\ P_{zz}^T- &= -1.656 \pm 0.049 \qquad (2.9\,\%) \end{aligned} \tag{5.5}$$

The differences between the relative uncertainties (in brackets) originate from the injection mode dependent systematic error of the atomic polarization.

Summary

In this work the calculation of the nuclear polarization of the HERMES hydrogen/deuterium gas target has been discussed and average values for 1997 and 2000 running periods have been presented. These two years represent the times which the largest part of the HERMES data taken with a longitudinally polarized target belongs to. In the HERMES target, the factors that can limit the overall polarization, as well as its measurement uncertainty, are the atomic recombination and spin relaxation potentially occurring inside the storage cell. All the calibration techniques performed in order to estimate how much the gas sample is influenced by these processes have been shown along with the related corrections applied to transfer the results to the average target values.
The two analyzed datasets pointed out dissimilar target performances. Beside the expected changes in the injected polarization and in the spin relaxation probability due to the different hyperfine structures of hydrogen and deuterium, also the properties of the storage cell surface showed distinct responses during the two periods. From this point of view, the 1997 hydrogen run registered a rather involved situation, where the recombination probability was several times affected by the interaction of the storage cell surface with the HERA beam. An accurate analysis of the cell conditions for the periods with different surface characteristics has played an essential role for the limitation of the uncertainty coming from the sampling corrections. The other source of error related to recombination, namely the remnant polarization of recombined molecules, β, has been estimated with considerable precision resulting to be about two third of the nuclear polarization of atoms. Beside its own physical account, this achievement has revealed that, for cell temperatures larger than 100 K, a couple of percent fluctuation on the amount of recombination does not seriously affect the target polarization whose average value was eventually determined with a 4 % relative uncertainty. The comparison with the 7 % relative error that could be obtained whitout any knowledge about the β value reveals a substantial improvement.
During the deuterium data taking period in 2000, the HERMES target experienced very stable running conditions. The cell surface did not show any effective modification through the whole year and no detectable spin relaxation or atomic recombination occurred. Such an unprecedented situation allowed a very smooth evaluation of the average nuclear and

tensor polarizations with a relative uncertainty in the order of 3 %. This value is mostly dominated by the accuracy obtained in the determination of the amount of unpolarized molecules coming from the residual gas or ballistically injected by the atomic beam source. Hence, the strategy adopted for the present and future runs is addresses to an improvement of those calibration measurements that are regularly performed to disentangle the different molecular sources.

Besides the performance achieved during the past runs, part of the thesis has been devoted to the studies made in 2000/2001, during the one year long HERA shutdown, for the purpose of changing the target polarization axis from longitudinal to transverse to the beam momentum. The design of the new target magnet is presented in relation to the field constraints given by the bending and emission of synchrotron radiation by the HERA beam, as well as the occurrence of densely spaced beam induced depolarizing resonances absent in the longitudinal case. The magnet was eventually installed and, since 2002, HERMES is being running with a hydrogen transverse polarized target. Although the poor performance of the HERA machine over the whole last year did not allow a complete analysis of the incidence of the resonant spin relaxation, the effect seems to be limited to a couple of percent at maximum beam current. Since this value could be reduced by an improved target field uniformity, the possibility of embedding two correction coils inside the storage cell support structure is currently under test. However, due to the 10 % less holding field strength, the determination of the target polarization for this running period will suffer a worse accuracy compared to 1997. The goal is to limit this value within a 5 % relative uncertainty.

Appendix A

The HERMES Spectrometer

The HERMES experiment is provided with a forward angle magnetic spectrometer [Ack98] of conventional design and symmetric about a central, horizontal shielding plate located in the magnet. A diagram of the instrument is shown in figure A.1. The polar (θ) and azimuthal (ϕ) scattering angles as well as the initial trajectory for the determination of the particle's momentum are measured by the front tracking system which consists of microstrip gas chambers - so-called vertex chamber (VC) - and drift chamber (DVC, FC1/2). The momentum measurement is completed by two sets of drift chamber behind the magnet (BC1/2 and BC3/4). Three proportional chambers in the magnet (MC1/3) are used to to help match front and back tracks as well as to track low momentum particles that do not reach the rear section of the spectrometer. The magnet, capable of a maximum deflecting power of 1.5 T·m, is of the H-type with field clamps in front as well as behind to reduce the fringe fields.
Particle identification (PID) is provided by a led glass calorimeter, a preshower detector (H2) consisting of two radiation lengths of lead followed by a plastic scintillator hodoscope, a transition radiation detector (TRD), consisting of six identical modules, and a Ring Imaging Čerenkov detector (RICH) allowing to distinguish between pions, kaons and protons. Positron in the momentum range between 0.1 and 27.6 GeV are identified using a probability method based on signals coming from the calorimeter, the preshower and the TRD: the identification efficiency exceeds 98 %.
The calorimeter and the preshower detector are included in trigger along with a second hodoscope (H1).
The acceptance is limited at small angle by an iron plate in the beam plane, which shields the electron/positron and proton[55] beams from the field of the spectrometer magnet. Particles with scattering angles within ± 170 mrad in the horizontal direction and between +(-)40 and +(-)140 mrad in the vertical direction are accepted. Therefore, the range

[55]The HERA storage ring is an electron/positron-proton collider. HERMES makes use of the lepton beam only.

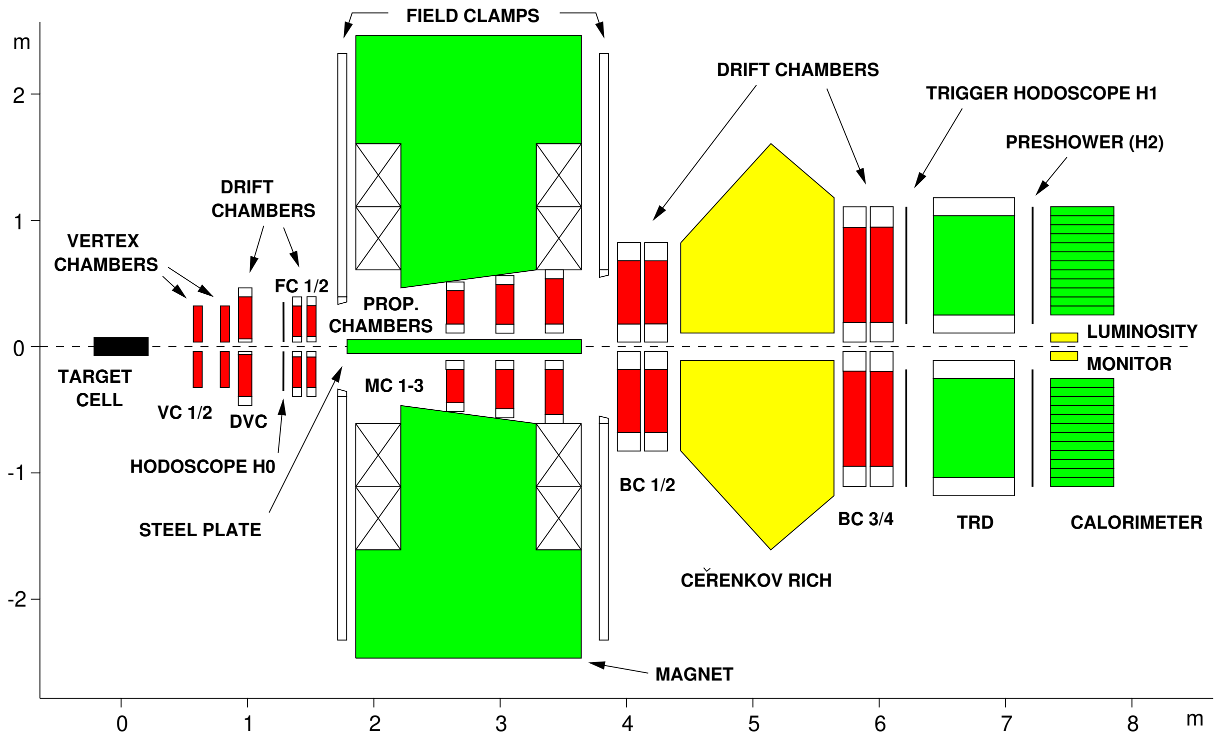

Figure A.1: A schematic side view of the HERMES spectrometer

of polar scattering angles is 40 mrad to 220 mrad. Spin structure functions depend on $x = Q^2/2M\nu$, where Q is the four momentum transfer in the DIS reaction, ν is the energy transfer and M is the mass of the nucleon. With a beam energy of 27.5 GeV, the x range covered by the HERMES experiment is 0.02-1.0.

The luminosity measurement is based on the Bhabha(Moeller) elastic scattering of beam positrons(electrons) and annihilation into photons pairs. A more extensive description of the possible use of luminosity monitor for target relate purposes has been given in section 2.8

The backbone of the data acquisition system is constructed in Fastbus. It consists of 10 front-end crates, the event collector crate and the event receiver crate connected to the online workstation cluster via 2 SCSI interfaces.

Appendix B

Target Hardware Control, Data Acquisition and Online Monitoring

The target data acquisition (DAQ) system is part of the HERMES DAQ system. Tasks of the target DAQ are: monitor the target general parameters, define the ABS injection mode, control the BRP and TGA measurements and read their countrates in order to evaluate the atomic polarization and atomic fraction. These operations are carried out by two different kind of software:

- The *brpclient* program. This software is the heart of the target DAQ. It controls all the ABS and BRP hyperfine transitions power supplies, as well as the BRP and TGA ion-optics and quadrupole mass spectrometers. Hence, the brpclient defines the ABS injection mode, the BRP polarization measurement cycle and the BRP and TGA detected masses. All necessary commands for one measurement are stored in a *front end list* (FEL) for the purpose of minimizing the delay between the sending and the execution of a command. The FEL is then sent to the main HERMES DAQ system which distributes the signals for the different power supplies to several DAC (digital to analog converter) modules. The measurement of the TGA and the BRP as well as the evaluation of the time resolving counter (TRC) is performed by the multi scaler input (MSI) of the DSP (digital signal processor) board. The DSP is connected to the FEL via a Fastbus, causing therefore minimal delay. At the end of the measurement, the results are transferred back to the brpclient in form of a list of countrates each of them is associated either to a chopper window open or closed. From these raw data, the brpclient evaluates the beam signals by background subtraction and calculates the hyperfine populations and atomic fraction of the sample beam. All the data is then stored in ADAMO (ALEPH Data Model) tables and sent to the DAD server (Distributed ADAMO Database). The same data is also stored as *user events* in EPIO records (Experimental Physics Input Output). The brpclient can be controlled either interactively, through a menu based

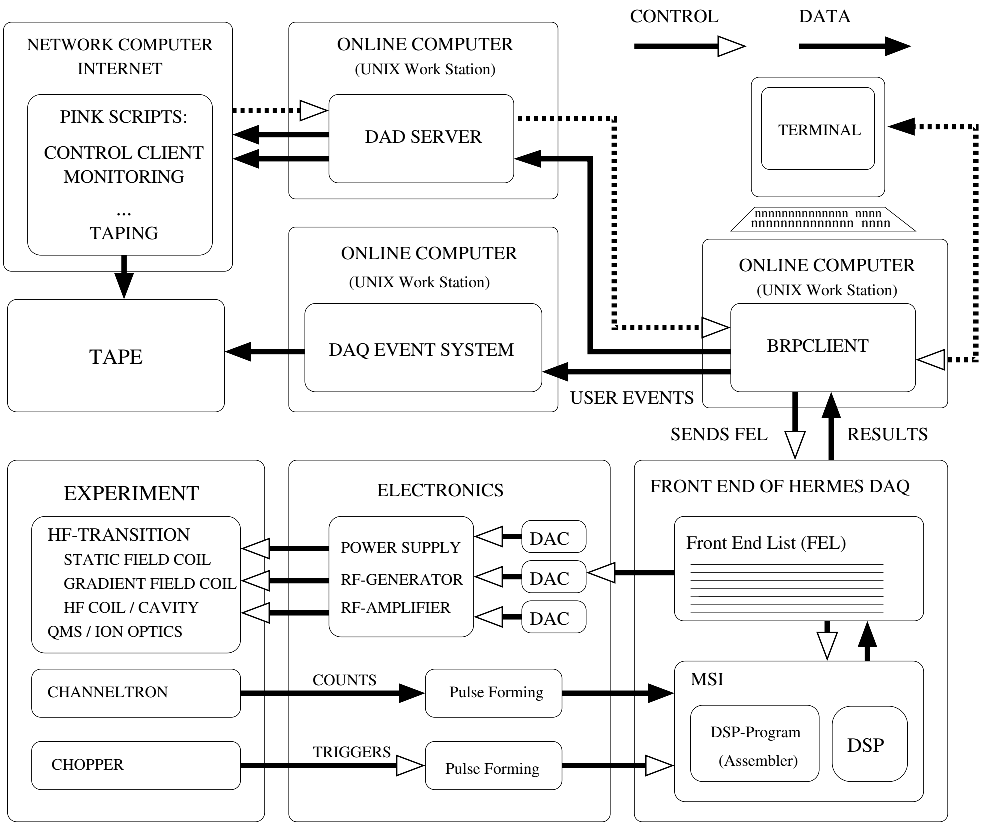

Figure B.1: Schematic of the HERMES target DAQ system.

controlled terminal program, or via the *brpclient control panel*, a PinK[56] script via the DAD server connection.

- The slow control (SC). The programs belonging to the slow control system read ADC (analog to digital converter) modules via CAMAC interface (computer automated measurement and control) in times intervals of typically several seconds up to a minute. The purpose of the slow control is to monitor the behavior of temperatures, vacuum pressures, power supplies voltages and/or currents, etc. that are relevant for the target general functioning. As all the HERMES data, also these values are stored in ADAMO tables and sent to the DAD server, from where they are read by PinK scripts for the online monitoring.

A schematic of the HERMES target DAQ system is shown in figure B.1.

[56]PinK is a DAD extension of Tcl/Tk (Tool Command Language / Toolkit) which allows to write small monitoring and controlling tasks.

List of Figures

List of Tables

Bibliography

[Abr58] A. Abragam, J.M. Winter; *Phys. Rev. Lett. Vol 1*, **10 (1958)**, 374.

[Ack98] K. Ackerstaff *et al.*; *Nucl. Instrum. and Meth. A*, **417 (1998)**, 230.

[Ack99] K. Ackerstaff *et al.*; *Phys. Rev. Lett.*, **82 (1999)**, 1164.

[Ala00] R. Alarcon *et al.*; *Nucl. Phys. A*, **663 (2000)**, 1111.

[All72] A.C. Allison; *Phys. Rev. A*, Vol. 1, **6 (1972)**, 2695.

[And63] P.W. Anderson in *Magnetism Vol. I*; G.T. Rado and H. Suhl (Edts.), Academic Press N.Y. (1963).

[Bar01] S. Barsov *et al.*; *Nucl. Instrum. and Meth. A*, **462 (2001)**, 364.

[Bau00] C. Baumgarten; Ph.D. Thesis, Ludwig-Maximilians Universitaet Muenchen, May 2000.

[Bau01] C. Baumgarten; Private Communication, 2001.

[Bau02a] C. Baumgarten *et al.*; *Eur. Phys. J. D*, **18 (2002)**, 37.

[Bau02b] C. Baumgarten *et al.*; *Nucl. Instrum. and Meth. A*, **482 (2002)**, 606.

[Bau02c] C. Baumgarten *et al.*; *Nucl. Instrum. and Meth. A*, **486 (2002)**, 1.

[Bau02d] C. Baumgarten *et al.*; *Nucl. Instrum. and Meth. A*, **496 (2002)**, 263.

[Bau02e] C. Baumgarten *et al.*; *Nucl. Instrum. and Meth. A*, **496 (2002)**, 277.

[Bau02f] C. Baumgarten *et al.*; A Gas Analyzer for the Internal Polarized Target of the HERMES Experiment, to appear in *Nucl. Instrum. and Meth. A*.

[Ben94] T. Benisch; Diploma Thesis, Friedrich-Alexander-Universitaet Erlangen-Nuernberg, 1994.

[Ben98] T. Benisch; Ph.D. Thesis, Friedrich-Alexander-Universitaet Erlangen-Nuernberg, 1998.

[Bou63a] M.A. Bouchiat; *J. Phys. Radium*, **24 (1963)**, 379.

[Bou63b] M.A. Bouchiat; *J. Phys. Radium*, **24 (1963)**, 611.

[Bou65] M.A. Bouchiat and J. Brossel; *Phys. Rev. 147*, **1 (1965)**, 41.

[Bra95] B. Braun; Ph.D. Thesis, Ludwig-Maximilians Universitaet Muenchen, 1995.

[Bru01] I. Brunn; Diploma Thesis, Friedrich-Alexander-Universitaet Erlangen-Nuernberg, April 2001.

[Buu00] L.D. van Buuren *et al.*; *Nucl. Phys. A*, **663 (2000)**, 1049.

[Cam86] J.C. Camparo; *J. Chem. Phys. 86*, **3 (1987)**, 1533.

[Cer94] CAS; Fifth General Accelerator Physics Course, CERN 94-01, Geneve (1994).

[Coh77] C. Cohen-Tannoudji, B. Diu, F.Laloe; Quantum Mechanics, Wiley-Interscience Publication (1977).

[Con02] M. Contalbrigo; A First Measurement of the Tensor-Polarized Structure Function b_1^d, to appear in the Conference Proceedings of SPIN 2002, 15th International Spin Physics Symposium.

[Des76] M. Desaintfuscion, C. Audion; *Phys. Rev. A*, **13 (1976)**, 2070.

[Dez95] W.A. Dezarn *et al.*; *Nucl. Instr. Meth. A*, **362 (1995)**, 36.

[Dre83] W. Drewes *et al.*; *Phys. Rev. Lett.*, **50 (1983)**, 1759.

[Due90] M. Dueren; A Luminosity Monitor for the HERMES Experiment, DESY-HERMES 5/90.

[Due95] M. Dueren; Habilitation Thesis, Friedrich-Alexander-Universitaet Erlangen-Nuernberg, July 1995.

[Eld47] F.R. Elder *et. al.*; *Phys. Rev.* **71**, (1947) 829.

[Eng02] R. Engels; Ph.D. Thesis, Univ. Koeln (2002).

[Fic71] D. Fick; Einf"uhrung in die Kernphysik mit polarisierten Teilchen, BI-Hochschulskripte Bd. **755a**, Mannheim (1971).

[Gae13] W. Gaede; *Ann. Physik*, **41 (1913)**, 289.

[Ger21] W. Gerlach, O. Stern; *Z. Physik*, **8 (1921)**, 110.

[Gil93] R. Gilman *et al*; *Nucl. Instr. Meth. A*, **327 (1993)**, 277.

[Hae67] W. Haeberli; *Ann. Rev. Nucl. Sci.*, **17 (1967)**, 373.

[Hae80] W. Haeberli; Contribution to the Proceedings of the 5th International Symposium on Polarization Phenomena in Nuclear Physics, no. 69 in AIP Conference Proceedings, (1980), 931.

[Hal80] K. Halbach; *Nucl. Instrum. and Meth.*, **169 (1980)**, 1.

[Har81a] J. Harris and B. Kasemo; *Surf. Sci. (Lett.)* **105 (1981)**, L281.

[Har81b] J. Harris, B. Kasemo and E. Törnquist; *Surf. Sci. (Lett.)* **105 (1981)**, L288.

[Hen02] M. Henoch; Ph.D. Thesis, Friedrich-Alexander-Universitaet Erlangen-Nuernberg, July 2002.

[Her93] The HERMES Collaboration; HERMES Technical Design Report, July 1993.

[Hlm71] U. Holm, H Ebinghaus; *Nucl. Instrum. and Meth.* **95 (1971)**, 39.

[Hol94] S. Holloway; *Surf. Sci.*, **299/300 (1994)**, 656.

[Knu09] M. Knudsen; *Ann. Physik*, **28 (1909)**, 999.

[Koc98] N. Koch; Ph.D. Thesis, Friedrich-Alexander-Universitaet Erlangen-Nuernberg, March 1999.

[Koe88] J.M.V.A. Koelman *et al.*; *Phys. Rev. A*, Vol. 38, **7 (1998)**, 3535.

[Kol98] H. Kolster; Ph.D. Thesis, Ludwig-Maximilians Universitaet Muenchen, February 1998.

[Lem93] S.K. Lemieux *et al.*; *Nucl. Instrum. and Meth. A* **333 (1993)**, 434.

[Len02] P. Lenisa; New Precision Results on the Spin Structure Function g_1^d, to appear in the Conference Proceedings of SPIN 2002, 15th International Spin Physics Symposium.

[Lid98] David R. Lide; Handbook of Chemistry and Physics, CRC Press, 79th Ed. 1998-1999.

[Mar02] H. Marukyan; Private Communication, 2002.

[Mes61] A. Messiah; Quantum Mechanics volume II, North-Holland Publishing Company, Amsterdam, 1961.

[Nas02] A. Nass *et al.*; The HERMES Polarized Atomic Beam Source, to appear in *Nucl. Instrum. and Meth. A*.

[Oh70] S. Oh; *Nucl. Instrum. and Meth.*, **82 (1970)**, 189.

[Phi87] R.J. Philpott; *Nucl. Instrum. and Meth. A*, **259 (1987)**, 317.

[Pot98] S. Potashov; HERMES Internal Report 31, 1998.

[Pot02] S. Potashov; Ph.D. Thesis, Lebedev Physical Institute in Moscow, 2002

[Pur56] E.M. Purcell and G.B. Fields; *Astrophys. J.*, **124 (1956)**, 542.

[Reg99] D. Reggiani; Diploma Thesis, Università degli Studi di Ferrara, December 1999.

[Reg02] D. Reggiani; Beam Induced Depolarizing Resonances in the HERMES Hydrogen/Deuterium Target, to appear in the Conference Proceedings of SPIN 2002, 15th International Spin Physics Symposium.

[Rob92] A.D. Roberts *et al.*; *Nucl. Instrum. and Meth. A*, **322 (1992)**, 6.

[Smo10] M.v. Smoluchowski; *Ann. Physik*, **33 (1910)**, 1559.

[Sok64] A.A. Sokolov and I.M. Ternov; *Sov. Phys.*, Doklady **8 (1964)**, 1203.

[Ste94] M. Stephens, R. Rhodes and C. Wieman; *J. Appl. Phys. 76*, **86 (1994)**, 3479.

[Sto02] U. Stoesslein; Private Communication, 2002.

[Tgp01] The HERMES Target Group; The polarization of HERMES target and its error for the deuterium running in 2000, HERMES Internal Report (2002).

[Tho87] G.E. Thomas *et al.*; *Nucl. Instr. Meth. A*, **257 (1987)**, 32.

[Vdb97] J.F.J. van den Brant *et al.*; *Phys. Rev. Lett.*, **78 (1997)**, 1235.

[Wal93] T. Walker and L.W. Anderson; *Nucl. Instrum. and Meth. A*, **334 (1993)**, 313.

[Wei98] C. Weiskopf; Diploma Thesis, Friedrich-Alexander-Universitaet Erlangen-Nuernberg, 1998.

[Wis01] T. Wise *et al.*; *Phys. Rev. Lett.*, **87 (2001)**, 042701.

[Zap96] K. Zapfe; *Nucl. Instr. Meth. A*, **368 (1996)**, 293.

[Zel86] A.N. Zelenski, *et al.*; *Nucl. Instrum. and Meth. A*, **245 (1986)**, 223.